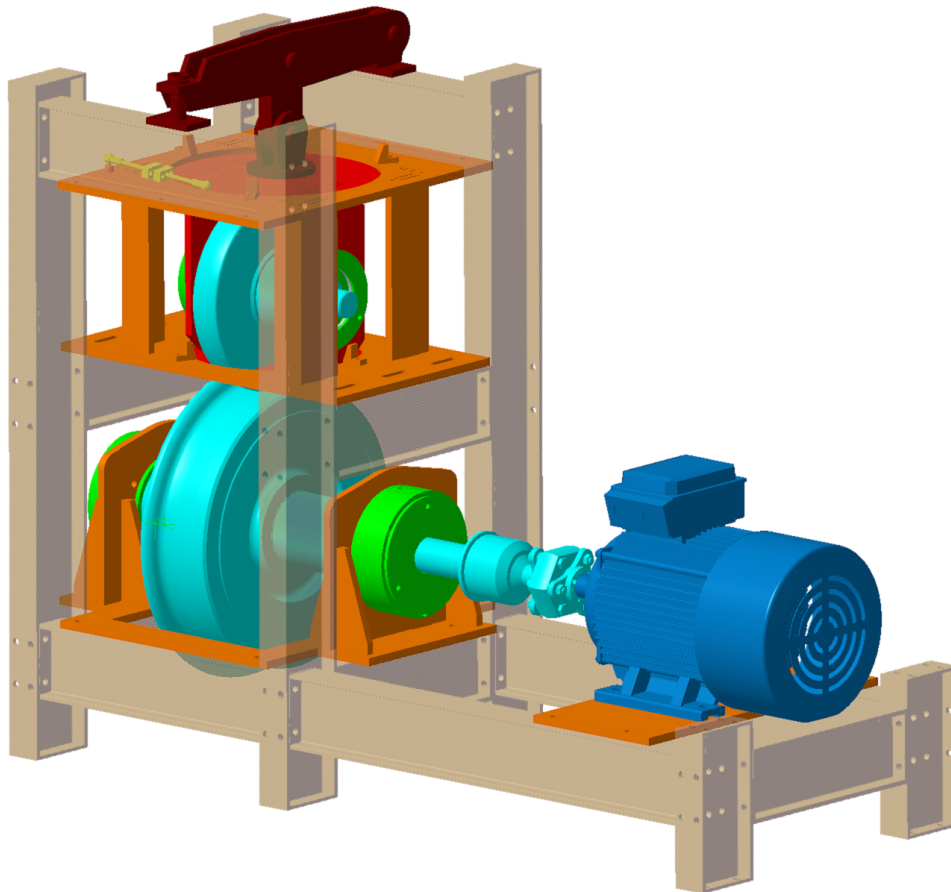




**CHALMERS**  
UNIVERSITY OF TECHNOLOGY

---



# Design of a Test Rig for Railway Curve Squealing Noise

Master's thesis in Sound and Vibration

ARTHUR AGLAT and JANNIK THEYSSEN



MASTER'S THESIS BOMX02-17-86

# Design of a Test Rig for Railway Curve Squealing Noise

ARTHUR AGLAT

and

JANNIK THEYSSEN



**CHALMERS**  
UNIVERSITY OF TECHNOLOGY

Department of Civil and Environmental Engineering  
*Division of Applied Acoustics*  
CHALMERS UNIVERSITY OF TECHNOLOGY  
Gothenburg, Sweden, 2017

**Design of a Test Rig for Railway Curve Squealing Noise**  
ARTHUR AGLAT and JANNIK THEYSSEN

© ARTHUR AGLAT and JANNIK THEYSSEN, 2017.

Supervisor: Astrid Pieringer<sup>1</sup>

Examiner: Wolfgang Kropp<sup>1</sup>

<sup>1</sup> Division of Applied Acoustics, Chalmers University of Technology

Master's Thesis BOMX02-17-86

Department of Civil and Environmental Engineering

Division of Applied Acoustics

Chalmers University of Technology

SE-412 96 Gothenburg

Telephone +46 (0) 31-772 1000

Cover: Assembly of the designed test rig

Gothenburg, Sweden, 2017

# Design of a Test Rig for Railway Curve Squealing Noise

ARTHUR AGLAT and JANNIK THEYSSEN

Division of Applied Acoustics

Department of Civil and Environmental Engineering

Chalmers University of Technology

## Abstract

Curve squealing noise of railroad vehicles has been researched for over four decades. To describe this phenomenon, several models have been developed. An increasing stick-slip motion between the wheel and the rail is assumed to be a key component for the occurrence of squealing. Nevertheless, the circumstances necessary to initiate, uphold and amplify the stick-slip motion in this case are not yet fully described, and existing models need validation. However, due to the non-linear nature of the phenomenon as well as its dependency on a large number of parameters, precise in-situ measurements are difficult to conduct.

This Master's Thesis describes the conception, design and construction of a test rig to create and measure curve squeal noise. A conception of the basic setup is done using knowledge about comparable rigs built. A rig with two interacting wheels, one of them functioning as the rail, is targeted. To ensure the functionality as a test-rig for validating existing simulation-based models, certain settings of the rig need to be changeable. These settings, including for example applied normal force, creepage and rolling speed, are quantified in a parameter study. A wide range of input parameters is used in a repeated time-domain simulation of the interaction, and the number of squealing occurrences is evaluated. A 3D model of the rig necessary to provide the contact with the found set of parameters is developed. All parts involved are described and drawings are generated. The structural safety of critical parts is calculated.

**Keywords:** squeal, curve, railway, test rig, wheel/rail contact, roller, contact modelling, squealing occurrence parameters, mechanical engineering



# Acknowledgements

This work would not have been possible without the support of the Division of Applied Acoustics in Chalmers. Specifically, we would like to thank our supervisor Astrid Pieringer for her helpful advice whenever we needed it. We wish to express our thanks to our examiner Wolfgang Kropp whose approval gave us the confidence to go on. Both of you gave us a lot of room to develop our ideas and design the rig accordingly, which was a rewarding task. And last but certainly not least we would like to thank Börje Wijk, Lars Hansson and Ivan Zenzerovic for their support and advice.

For his advice regarding train wheels and continuous efforts in supporting us, topped by providing the wheel used in the rig, we would like to sincerely thank Erik Kihlberg of the company Lucchini Sweden AB.

Arthur Aglat and Jannik Theyssen

Gothenburg, 2017



# Contents

<b>List of Figures</b>	<b>xi</b>
<b>List of Tables</b>	<b>xiii</b>
<b>1 Introduction</b>	<b>1</b>
1.1 Introduction to the topic . . . . .	1
1.2 Motivation of this Work . . . . .	2
1.3 Placement in actual research . . . . .	3
<b>2 Theory</b>	<b>7</b>
2.1 Squealing Generation Mechanisms . . . . .	7
2.2 Scale-Down Properties of the Contact Patch . . . . .	8
2.3 Description of wheel dynamics . . . . .	9
2.4 Description of the Time Domain Squealing Model . . . . .	11
<b>3 Conceptual Design</b>	<b>13</b>
3.1 Description of the Dynamic Wheel Response . . . . .	13
3.1.1 Finite Element Method . . . . .	13
3.1.2 Measurement . . . . .	17
3.2 Parameter Study . . . . .	18
3.2.1 Parameter description . . . . .	18
3.2.2 Study Setup . . . . .	23
3.2.3 Study Results . . . . .	24
3.2.3.1 Evaluation Method . . . . .	25
3.2.3.2 Pre-study Results . . . . .	26
3.2.3.3 Main-study Results . . . . .	26
3.2.3.4 Side Study Mode Coupling . . . . .	30
<b>4 Construction</b>	<b>32</b>
4.1 Conceptual Construction . . . . .	32
4.1.1 Kinematic Considerations . . . . .	32
4.1.2 Outer Construction . . . . .	32
4.1.3 Force Generation Mechanism . . . . .	33
4.1.4 Longitudinal Creepage . . . . .	33
4.1.5 Vibration Isolation and Damping . . . . .	34
4.1.6 Measurement Concepts . . . . .	34
4.1.7 Motor Coupling . . . . .	35

4.1.8	Active Control Considerations . . . . .	36
4.1.9	Safety Concepts . . . . .	36
4.2	Construction Design . . . . .	37
4.2.1	Considerations regarding contact forces . . . . .	37
4.2.2	Shaft Pre-calculation . . . . .	39
4.3	Selection of purchased parts . . . . .	41
4.3.1	Star Disks . . . . .	41
4.3.2	Bearings . . . . .	42
4.3.3	Disk Springs . . . . .	43
4.3.4	Motor . . . . .	44
4.3.5	I-Profiles . . . . .	47
4.4	Rig Mock-up . . . . .	48
4.5	Stability calculations . . . . .	52
4.5.1	Analytic safety calculation for critical parts . . . . .	52
4.5.1.1	Shafts . . . . .	52
4.5.1.2	Bearings . . . . .	55
4.5.1.3	Bolts . . . . .	58
4.5.1.4	Press fits . . . . .	60
4.5.2	FEM stability calculations . . . . .	63
4.5.2.1	Lantern Sides . . . . .	63
4.5.2.2	Lower side plates . . . . .	64
<b>5</b>	<b>Discussion</b>	<b>66</b>
<b>6</b>	<b>Conclusion and Outlook</b>	<b>68</b>
	<b>Bibliography</b>	<b>69</b>
<b>A</b>	<b>Appendix - Design</b>	<b>I</b>
A.1	Upper Wheel Geometries Eigenmodes . . . . .	I
A.2	Parameter Study Results . . . . .	II
A.3	Lower Wheel Mockup . . . . .	IV
<b>B</b>	<b>Appendix - Construction</b>	<b>V</b>
B.1	Bearing Data Sheets . . . . .	V
B.2	Star Disks Data Sheets . . . . .	V
B.3	List of Parts . . . . .	V

# List of Figures

1.1	Boogie passing through a narrow curve. . . . .	1
2.1	Moving Mass on a Conveyor Belt: A Stick-Slip Example . . . . .	7
2.2	Precompiled Friction Curve Example . . . . .	8
2.3	Contact patch ellipse between the rail and the wheel . . . . .	8
2.4	Mode Shapes on Disks. . . . .	11
2.5	Engineering schematic model for contact forces . . . . .	11
3.1	Eigenfrequencies of the Lower Wheel . . . . .	14
3.2	Axial mode shapes of the wheel up to 10 kHz. . . . .	15
3.3	Circumferential mode shapes of the wheel up to 10 kHz. . . . .	15
3.4	Radial mode shapes of the wheel up to 10 kHz. . . . .	16
3.5	Lower Wheel Radial Mode at 6607 Hz . . . . .	16
3.6	Lower Wheel Axial Mode at 7074 Hz . . . . .	16
3.7	Comparison of Calculated Receptances for the Lower Wheel. . . . .	17
3.8	Measured and simulated inertances for the lower wheel. . . . .	18
3.9	Researched geometries for the upper wheel. Only half the outline of the cross-section is shown. . . . .	20
3.10	Comparison of Calculated Receptances for the Rail Wheels. . . . .	20
3.11	Wheel head geometry cross-section including contact node. . . . .	21
3.12	Rail wheel head cross-sections including contact node. . . . .	21
3.13	The influence of the chosen modal damping coefficients on the recep- tance. . . . .	22
3.14	Legitimation of Calculation Time Optimization. . . . .	25
3.15	Example result of time-domain solution of the contact problem for a squealing case. . . . .	25
3.16	Understanding the Parameter Study Results Plot. . . . .	28
3.17	Result summary for simulations with wheel geometry WG5. . . . .	29
3.18	short . . . . .	31
4.1	Kinematic interdependence of lateral displacement and creepage. . . . .	33
4.2	Lateral forces acting in the contact point. . . . .	38
4.3	Limit circle with forces acting in the different load cases. . . . .	39
4.4	Coordinate system definition for shaft strength calculation. . . . .	40
4.5	Simulated start-up of the lower wheel with two different motors. . . . .	46
4.6	A principal sketch of I profiles. . . . .	47
4.7	Effect of an increased I profile height on the beam deflection. . . . .	48

4.8	Upper shaft assembly. . . . .	49
4.9	Upper shaft cage assembly. . . . .	50
4.10	Rod and spacers angle setting construction. . . . .	50
4.11	Lower shaft assembly. . . . .	51
4.12	Lower shaft cage assembly. . . . .	51
4.13	Core rig assembly. . . . .	52
4.14	Force lever assembly. . . . .	53
4.15	Driving assembly. . . . .	53
4.16	Complete rig. . . . .	54
4.17	Principal Sketch of the Force Lever Bolt. . . . .	59
4.18	Lantern Side Clamped Feet . . . . .	63
4.19	Lantern Side Contacting Surface with Bearing Housing . . . . .	63
4.20	Lantern Side Von Mises Stress under a Force of 18 kN . . . . .	64
4.21	Half Clamped Elements on the Lower Side Plate . . . . .	65
4.22	Lower Side Plate Von Mises Stress under a Force of 19 kN . . . . .	65
A.1	Eigenmodes of Upper Wheel Geometries . . . . .	I
A.2	Result plot for simulations with wheel geometry WG6. . . . .	II
A.3	Result plot for simulations with wheel geometry WG4. . . . .	III
A.4	Back View of the Lower Wheel . . . . .	IV
A.5	Front View of the Lower Wheel . . . . .	IV
B.1	Data Sheet for Bearing Type 6017-2RS1 . . . . .	VI
B.2	Data Sheet for Bearing Type 6020-2RS1 . . . . .	VII
B.3	Data Sheet for Star Disks. . . . .	VIII
B.4	Data Sheet for Star Disks. . . . .	IX

# List of Tables

1.1	Comparison of existing squealing noise test rigs. . . . .	6
3.1	Lateral creepage steps and according angles. . . . .	23
3.2	Overview over used input parameters in both parameter studies. . . . .	23
3.3	Discretization settings in pre- and main-study. . . . .	24
3.5	Number of squealing cases counted for each set of simulations in the main-study. . . . .	26
3.4	Number of squealing cases counted for each set of simulations in the pre-study. . . . .	26
3.6	Result for damping influence in parameter study. . . . .	27
3.7	Result for friction influence in parameter study. . . . .	27
3.8	Parameter study result for squealing cases over evaluated time segment. . . . .	30
3.9	Effect of removing potentially coupled modes on the occurrence of squealing for squealing at about 2020 Hz. . . . .	30
3.10	Effect of removing potentially coupled modes on the occurrence of squealing for squealing at about 8580 Hz. . . . .	31
4.1	Basic design diameters for upper and lower shaft. . . . .	41
4.2	short . . . . .	45
4.3	Upper Shaft Safety Calculation Data. . . . .	56
4.4	Lower Shaft Safety Calculation Data. . . . .	57
4.5	Calculation Data for the Bearing Life Rating . . . . .	58
4.6	Calculation data for the bolt safety calculation. . . . .	60
4.7	Shaft-Hub connection calculation data. . . . .	62
4.8	Maximum Stress Induced in Lantern Side Plate . . . . .	64
4.9	Maximum Stress Induced in Lower Side Plate . . . . .	65
B.1	List of Parts . . . . .	X



# 1

## Introduction

### Introduction to the topic

A rail vehicle passing through a narrow curve can emit an high-pitch, tonal sound [1, 2]. This unpleasant sound known as squeal noise occurs in a frequency range of 250 Hz to 5000 Hz [3, 4] in which the human hearing is very sensitive [4, 5]. Since squealing is linked to narrow curves, it is especially a problem in inner cities, where tramways were built into the preexisting infrastructure. This further amplifies the impact on humans.

The basic mechanism leading to curve squeal is described by Rudd as a crabbing motion of the vehicle [1]. The setup of the wheel suspension of many trains is designed such that the axles of the boogie are always parallel. When running in a curve, it is therefore impossible to bring both axles perpendicular to the curve tangent. This leads to a sideways-sliding of at least one of the axles, which is the basis for the occurrence of squealing. This explanation has been widely adopted [4, 6, 7].

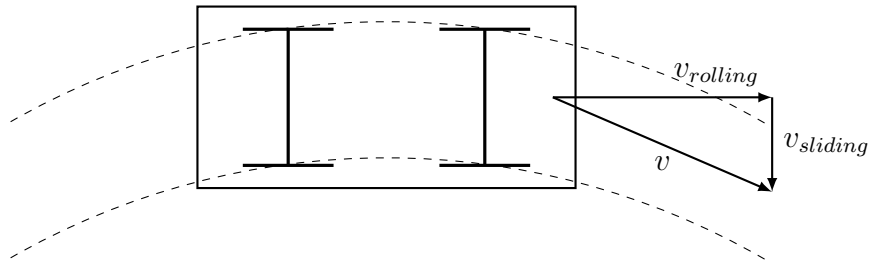


**Figure 1.1:** Boogie passing through a narrow curve (Figure as seen in [1, 3]).

Figure 1.1 visualizes this situation. The sideways-sliding is called lateral creepage  $\eta$  and is quantified as the relative velocity between the wheel and the rail surface in the transverse lateral direction, normalized by the actual forward velocity  $v$  [3]:

$$\eta = \frac{\Delta v_{sliding}}{v} \quad (1.1)$$

One further characteristic of many rail vehicles is that the two wheels on one axle are rigidly connected. During curving the inner wheel follows a shorter track, potentially leading to a longitudinal sliding of one of the wheels, called differential slip [1, 3]. The longitudinal creepage  $\xi$  is described by

$$\xi = \frac{\Delta v_{rolling}}{v}. \quad (1.2)$$

In addition to lateral and longitudinal creepage, Rudd described flange rubbing as a potential situation leading to squealing [1]. Several authors state that the lateral creepage is the main reason for squealing [1–3].

However, there is no direct link between the creepages and the occurrence of squealing but instead an eclectic contact problem [8] that is dependent on a variety of influence factors [9, 10] and determined by the dynamics of the wheel and the rail [6, 7, 9, 11, 12]. Concerning the contact problem, it is generally accepted that the creepage can lead to a stick-slip motion in the contact, that in turn can lead to an excitation of the wheel, specifically certain modes of the wheel [10]. The influence factors, in [9] generalized as a “given set of atmospheric and mechanical characteristics”, include the relative humidity [13], the angle between the rolling direction and the curve tangent also called angle of attack [14], the lateral contact position [6], [15], the wheel damping [1], rail lubrication [2] and the rolling speed [14]. The study of the wheel and rail dynamics suggests that squealing occurs when a the stick-slip frequency matches an eigenfrequency of the wheel [3]. Some authors specify that this eigenfrequency needs to belong to an axial mode shape [6, 10]. [9] points out that eigenfrequencies can vary up to 15 % over the lifetime of a wheel due to the decrease in outer diameter because of wear.

In [16], squealing is described as an "on-off-phenomenon" that can either be eradicated completely or no success is expectable. No benefit is seen in trying to reduce it in level, only in occurrence. Different approaches to reducing the occurrence are discussed. Eliminating the crabbing motion by improving the curving behavior is suggested [2, 3] as well as changing the track layout [2]. The wheel damping is considered an important factor [1–3]. Reducing the friction coefficient between wheel and rail by rail lubrication has been shown to decrease the squealing occurrence [2, 17]. The existence of longitudinal creepage superposed with a lateral creepage has been shown to reduce the lateral creep force and with that, reduce the incidence of squeal [10, 18]. [3] suggests the use of asymmetric rail profiles to reduce squealing occurrences. An active control mechanism to prevent the squeal occurrence was successfully implemented in [13].

## Motivation of this Work

The main goal is to design a test rig that can be used for model validation purposes. Of the many factors that influence squealing in the field, most are not accurately controllable and much less repeatable. This gives measurements in the field an observing character, reducing their applicability when validating mathematical models. Furthermore, extensive measurement series that would be necessary for this purpose come at high expenses, simply due to the required rail vehicle and track.

The goal of this thesis is to design a test rig that specifically features conditions that are expected to lead to squeal noise. The stationary reproduction of squeal noise under constant outer conditions is supposed to facilitate the measurement of significant quantities involved. With that, existing mathematical models can be

validated. As a future step, active vibration control is meant to be implemented to prevent the squealing noise.

## Placement in actual research

Several test rigs have been built for squealing research purposes. A concise summary of existing test rigs that either have been or could be used for squealing noise research is given below. This is to meant to give a reference to what has been done so far and to elaborate on how an additional test rig can contribute to squealing research. An overview over the discussed test rigs is given in Table 1.1.

One test rig that was specifically designed for squeal noise research is the test rig build by the Netherlands Organization for Applied Scientific Research (TNO) in the Institute of Applied Physics (TPD) [19]. As most of the presented test rigs, it is a two wheel test rig in which one of the wheels resembles the actual tram wheel, and the other one acts as the rail. This choice is described as being the most compact and therefore the easiest to control. As pointed out in [20], the finite radius of the rail-wheel in comparison to the “infinite radius” of an actual rail reduces the contact area and thereby increases the contact stresses about 15% for a diameter ratio of 3. This rig is a scale rig with a ratio of 3, yet no quantitative information on the wheel diameters is given. The lateral radius of the rail-wheel is adjusted to compensate for the described increase in contact stresses.

Built based on a lathe, many of the inherent functions are used to produce the desired input parameters, like the wheel speed and the lateral offset. Many other parameters have been designed to be adjustable, like the rail inclination angle and even the ambient temperature and humidity. A feature that is unique to this test rig in this comparison is that the wheels are seemingly relatively easy interchangeable, which enables the adjustment of the transverse contact profile as well as the wheel impedance. The normal force is generated by applying a weight to the end of the lever holding the upper wheel. Measured quantities on this rig are the quasi-static normal and lateral contact forces and the radiated sound pressure level. An efficient way to introduce the damping on the rail-wheel is presented, namely the attaching of layers of thin sheet metal on the sides of the disk. The test rig has successfully produced squeal noise and generated insights into the effect of squealing on the measured friction coefficient [21].

The University of Queensland (UQ) and the CRC for Rail Innovation, Brisbane, Australia together with the RailCorp, New South Wales, Australia built a rail corrugation test rig (RCTR) that is also used for squealing research [10]. In the same manner as in the TNO TPD test rig it is set up as a two wheel test rig. Likewise, the wheels are downscaled and adjusted to recreate the original contact conditions. The normal force and the lower disk speed are input parameters. The normal force is controlled by adding shims under the carrying leaf springs. A feature that is unique to this test rig is that both wheels are driven, which is used to create a braking torque, leading to longitudinal slip. It is equipped with measurement systems that log the disk speeds, the normal force, the acting torque on the drive shafts which can be used to calculate the traction force, the disk temperatures and the disk profile height.

This rig produced squeal noise and was extensively used to validate existing squealing models [14,22]. Of the two wheels, the lower, larger disk is the one that produces the squeal noise, and it is hypothesized that this is due to the lower transverse stiffness and the larger propagational surface area. The squeal is therefore associated with the axial vibration modes of the lower wheel. An increase in sound power level is found with an increase of rotational speed. It is pointed out that during operation the torque and slip needed to be carefully controlled to avoid increases in slip that would affect the contact geometry and produce rapid wear.

The Hongik squeal test rig (HSTR) built by the Hongik University in Seoul and the Korea Railway Research Institute in Uiwang, features a full axle setup [23]. The two connected wheels are driven by two independently driven rail wheels. An additional feature unique to this test rig is the real time control of running speed and angle of attack, which enables the transient simulation of the axle negotiating a curve. The angle can be set in steps of 0.1 deg or 1.75 mrad. The transient simulation is complemented by introducing a rotation difference between the two wheels.

The test rig successfully generated squeal noise when the yaw angle was 0.5 deg or larger. The measurements of the lateral contact force were supplemented by a finite element model, which showed similar results.

A rig designed by the University New South Wales in Sydney (UNSW) is described in [20]. This rig is designed substantially larger than the other test rigs presented with a small wheel of 200 mm diameter running on a rail-wheel of 800 mm diameter. Accordingly, the rig is capable of higher forces with a maximum normal load of 12 kN. The angle of attack can be adjusted. However, the possibilities of adjusting other parameters are rather limited as the lateral position is fixed and no longitudinal creepage is implemented. No information was found about the success of this design. The test rig with the largest normal force of 40 kN in this comparison is presented in [20]. It is designed by the Manchester Metropolitan University (MMU) and used in cooperation with the Institute of Sound and Vibration Research (ISVR) of the University of Southampton. It consists of two rolling disks of 290 mm and 310 mm diameter of the same thickness and shaped with a transverse profile to generate a point contact. The slightly smaller, lower disk is driven. A comparatively large angle of attack of 10 deg can be realized by yawing the upper disk. At the time when the quoted report was published, the test rig was being equipped for squealing research. Hence, no detailed information about results are given.

Comparing these test rigs gives ideas on which features can be inherited from the existing ones and how a newly designed test rig can be beneficial. First of all, most of the model validation has been done with two wheel roller rigs. This can be considered for the basic design of the rig, since building a whole axle test rig is a significantly larger effort. Furthermore, it seems that squealing is observed at rather small yaw angles as described in [10, 23], which leads to prioritizing a sufficiently precise setting of the angle over allowing large yawing angles. Another observation is that most test rigs do not provide a real time control of any input parameters other than the wheel rotation speed. It is assumed that implementing a real time control often comes with the cost of a less precise and repeatable setting of that parameter, especially for translational motions. However, no drawback of this missing feature is observed in the outcomes. It seems suitable to design a test rig such that the input

parameters can be easily changed between operating the rig. Only some of the test rigs provide the option of introducing a longitudinal creepage, and model validation proved to be possible without this feature. However, to back the theory about the influence of longitudinal creepage, a mechanism to introduce longitudinal creepage is necessary. To keep the contact characteristics close to reality, the downscaling of the wheel is to be kept small and an adaption of the transversal profile of the rail wheel is recommended. As [20] points out, even though the contact can be adjusted to closely resemble the contact in the field, it is hard to scale the material properties. Only one of the wheels of the TNO TPD test rig can reproduce flange contact.

**Table 1.1:** Comparison of existing squealing noise test rigs. The type 1x2 describes two-wheel roller test rigs, 2x2 is a

	TNO TPD [19, 20]	UQ [10, 14, 22]	HSTR [23]	UNSW [20]	MMU TDR [20]
	Geometrical Description				
Type	Two wheel	Two wheel	Wheelset	Two wheel	Two wheel
Scale	1/3				1/3
Wheel diameter		170 mm		200 mm	310 mm
Rail-Wheel diameter		426 mm		800 mm	290 mm
	Creepages				
Lateral Creepage	yes	yes	yes	yes	yes
Longitudinal Creepage	no (2003)	yes	yes	no	yes
	Input Parameters				
Maximum Normal Load	2000 N	2000 N		12 000 N	40 000 N
Tangential Load		1000 N			
Maximum Angle of Attack	87.4 mrad	26 mrad	$\pm 52.4$ mrad	adjustable	173.5 mrad
Rail Inclination Angle	yes			no	
Lateral Offset	yes			no	no
Maximum Wheel Speed	2500 rpm	1200 rpm	150 rpm	787 rpm	
Friction Coefficient		0.45 (dry), (lubricated)	0.15 0.33		
Driven Wheel	rail wheel	rail wheel, wheel	rail wheel	rail wheel	rail wheel
Ambient Temperature	yes				
Humidity	yes				
Real Time Control	no		angle of attack, running speed		
Squealing Research	yes	yes	yes	possible	possible

# 2

## Theory

### Squealing Generation Mechanisms

As pointed out in the literature study, squealing can occur when the lateral creepage induces stick-slip in the contact area between wheel and rail. Figure 2.1 presents a simple model describing the stick-slip effect. The model consists of a mass which is placed on a moving conveyor belt and connected to a spring, which is fixed on the other side.

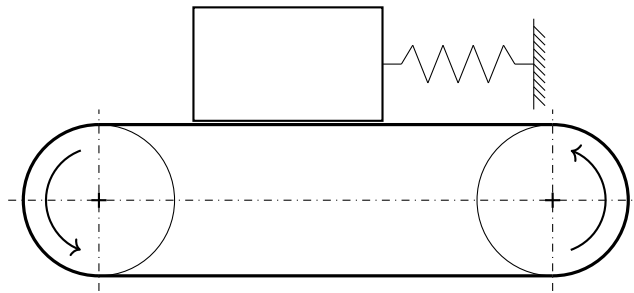


**Figure 2.1:** Moving Mass on a Conveyor Belt: A Stick-Slip Example

The static friction force between the mass and the belt makes the mass move along the conveyor, tensioning the spring. This phase is called stick phase. At some point, the spring force will increase above the static friction force and pull the mass against the conveyor motion. This phase is called slip phase, and a relative velocity, dependent on the dynamic friction force, occurs between the mass and the belt. While the mass is moving against the conveyor, the tension of the spring as well as the relative velocity of the mass is decreased. When the relative velocity reaches zero, the process is repeated. The oscillation is described by the conveyor speed, the mass, the spring stiffness and the normal force and friction coefficient between the mass and the conveyor belt. It is the constant motion of the conveyor belt that introduces the energy maintaining the oscillation. In the contact between the wheel and the rail, this energy is introduced by the sliding velocity as seen in Figure 1.1. As described in the introduction, it is assumed that squealing might occur if the frequency of these oscillations is close to an eigenfrequency of the wheel. The simulation model uses pre-compiled  $\mu$ -slip curves as they are only dependent on material properties and geometrical configurations. They can be presented as in Figure 2.2, where three different phases are defined. When the relative velocity is sufficiently high or low, the friction coefficient is assumed constant or almost constant. This phase is the sliding phase, with a dynamic friction force. When the

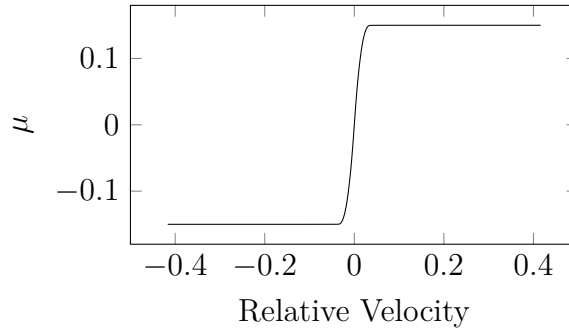


**Figure 2.2:** Precompiled Friction Curve Example

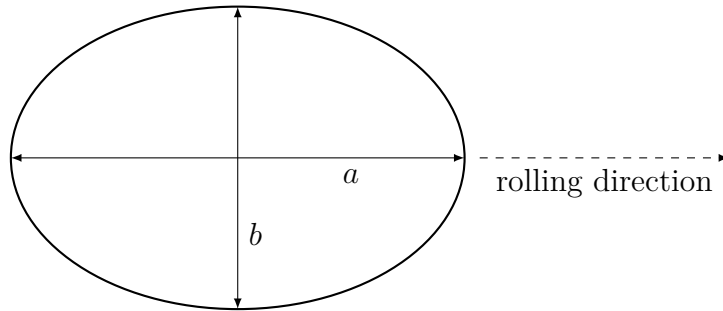


**Figure 2.3:** Contact patch ellipse between the rail and the wheel

relative velocity is close to zero, a static friction force applies in the contact region, and this is represented as the stick phase.

## Scale-Down Properties of the Contact Patch

When designing a rig recreating life like conditions of the contact between a rail and a wheel, one wants to make sure that the stress conditions in the contact area remain the same. Easy to implement and compact conceptual solution requires that the rail is replaced by a disk instead of a flat infinite surface. That is to say that such a modification transforms the infinite radius of the rail by some finite radius of a disk in its rolling direction. As a result, the contact patch between the two disks is elongated in the tangential direction. Those effects induced by this major change can be compensated by adjusting the lateral radius of the rail-wheel so that contact parameters can approach approximately 10% of their original value in the real contact as stated in [19]. This adjustment implies the tuning of the contact patch using the following equations 2.1 to 2.6.

As seen in [24] and following Hertz contact theory for elastic bodies to ensure dynamical similarities with the original case, one can assume that geometrical characteristics need to stand in the contact patch ellipse dimension of the scaled rig, namely the ratio of the semi-axis  $a$  and  $b$  seen in Figure 2.3 in the contact patch needs to stay constant.

To calculate the properties of the real conditions, two cylinders, one finite and one infinite for the wheel and the rail, rolling on each other, are assumed. The curvatures

of interest are then respectively for the wheel and the rail the longitudinal and the transversal curvatures. As a reference exemple, the standard profiles S1002 and UIC60 give radii of  $C_{S1002} = 0.4$  m for the axial radius of the wheel and  $C_{UIC60} = 0.3$  m for the transversal radius of the rail as shown in the contact description in [25]. This ratio  $\frac{b}{a}$  is calculated as follows and shall remain the same. One needs to assume that the longitudinal radius of the wheel is constant over its thread.

$$\frac{b}{a} = \left(\frac{A_1}{B_1}\right)^{\frac{2}{3}} \quad \text{with} \quad A_1 = \frac{1}{2.C_{S1002}} \quad \text{and} \quad B_1 = \frac{1}{2.C_{UIC60}} \quad (2.1)$$

However, when considering two wheels, the semi-axis needs to be calculated independently, and the previous assumption on the longitudinal radius cannot stand anymore. Linear Hertz theory for two elastic bodies is instead used. Let  $R_{1x}$ ,  $R_{1y}$  and  $R_{2y}$  being constant and representing respectively the rolling and transversal radii of the lower train wheel, and the rolling radius of the upper rail wheel. The transversal radius  $\mathbf{R}_{2x}$  of the upper wheel is left open for the tuning of the semi-axles ratio.

$$a = m \left( \frac{3N(1 - \nu^2)}{2E(A_2 + B_2)} \right)^{\frac{1}{3}} \quad (2.2)$$

$$b = n \left( \frac{3N(1 - \nu^2)}{2E(A_2 + B_2)} \right)^{\frac{1}{3}} \quad (2.3)$$

with  $m$  and  $n$  calculated or approximated using formulas and table from [26].

$$m = \sqrt{\frac{\sqrt[1.5]{X_2}}{X_1}} \quad \text{and} \quad n = m.X_1 \quad (2.4)$$

Function of  $X_1$  and  $X_2$  defined as follows:

$$X_1 = \left(\frac{A_2}{B_2}\right)^{0.63} \quad \text{and} \quad X_2 = \left(\frac{1 + \frac{A_2}{B_2}}{2\sqrt{\frac{A_2}{B_2}}}\right)^{0.63} \quad (2.5)$$

Which are themselves function of coefficients  $A_2$  and  $B_2$  defined with the different radii of curvature previously introduced.

$$A_2 = \frac{1}{2} \left( \frac{1}{R_{1y}} + \frac{1}{R_{2y}} \right) \quad \text{and} \quad B_2 = \frac{1}{2} \left( \frac{1}{R_{1x}} + \frac{1}{\mathbf{R}_{2x}} \right) \quad (2.6)$$

## Description of wheel dynamics

The dynamic behavior of the wheel has a key influence on squealing occurrence. A way to calculate this is presented in [27] and applied here. The wheel dynamics are described as Green's functions, which is the displacement response to a point force excitation. Here, the excitation is assumed in the contact point. In the frequency domain, the wheel is described using its receptance defined in the equation

$$\tilde{G}_{ij}(f) = \frac{\xi_j(f)}{F_i(f)}, \quad i, j = 1, 2, 3, \dots \quad (2.7)$$

with  $\xi_j(f)$  being the displacement response for the degree of freedom  $j$  under a harmonic excitation  $F_i(f)$ . The receptance is the displacement normalized by the excitation force. The mobility and inertance are achieved by deriving the receptance once or twice respectively with respect to time.

In the time domain, the wheel is described using its Green's function defined in the equation

$$\tilde{g}_{ij}(t) = \mathcal{F}^{-1}(\tilde{G}_{ij}(f)), \quad i, j = 1, 2, 3, \dots \quad (2.8)$$

applying an inverse Fourier transform to the previously found receptances.

Obtaining the wheel receptance requires the calculation of all wheel mode shapes up to the frequency of interest. For geometries as complex as train or tram wheel, a Finite Element (FE) model can be used to determine those mode shapes. Building a FE model that is appropriate for a modal analysis of a structure as large as a train wheel is computationally expensive when realized using 3D elements. However, when using the axi-symmetry of the wheel, elements named PLANE83 can be used, which in their design contain the information of the whole wheel. The description of such elements can be found in the ANSYS mechanical reference.

The contour of half the cross-section of the wheel is generated using a Computer Aided Design (CAD) software prior to discretizing it with the introduced elements. The boundary conditions of the model imitate the actual fixation of the wheel by assuming a rigid mounting on the shaft. The axle is assumed sufficiently stiff and provides no room for displacement for the wheel at the hub [9,27]. In the FE model, this condition is implemented by blocking the displacement degrees of freedom of the elements connected to the axle. However, not modeling the axle can induce errors in low-order eigenmodes, but is sufficiently accurate on high-order modes that can be of interest when dealing with squealing noise.

Modes order can be explained after detailing the type of modes encountered when dealing with disks in general. Types of modes are categorized by the predominant motions of the wheel in the three directions: axial, radial and circumferential. In each category, two other classifications are made, the amount of nodal diameters  $n$  and the amount of nodal circles  $m$ . The value  $n$  describes the order of a mode. A mode shape with one nodal diameter describes a vibration pattern in which the disk vibrates such that along one diameter, zero velocity is found. Accordingly, a mode has one nodal circle when along exactly one circle, there is no vibration. The oscillation on two sides of a nodal line typically has opposite phase. Figure 2.4 shows disks presenting these two cases. Mode shapes are named according to their nodal diameter  $n$ , their nodal circle  $m$  and their type ('a','r','c' for axial, radial and circumferential), for example  $(n,m,type)$ .

In a system with low damping, modes do not overlap much. This is the case for most train wheels, and the use of mode-specific damping is suitable for describing the damping in such a system. A modal damping  $\zeta$  found in the literature [7,28] for steel train wheels is applied to each type of mode according to their number of

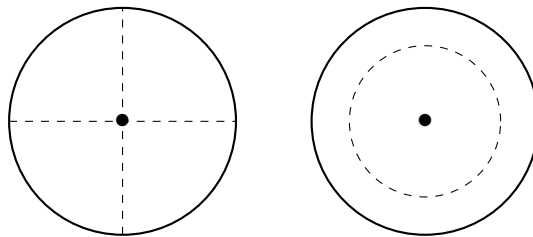


**Figure 2.4:** Visualization of modeshapes typical for round disks. Mode shapes with two nodal diameters (left) and one nodal circle (right).

nodal diameters.

$$\zeta = \begin{cases} 10^{-3} & \text{for } n = 0 \\ 10^{-2} & \text{for } n = 1 \\ 10^{-4} & \text{for } n \geq 2 \end{cases} \quad (2.9)$$

In case an actual wheel response is measured, these initial values can be tuned according to the measurement.

## Description of the Time Domain Squealing Model

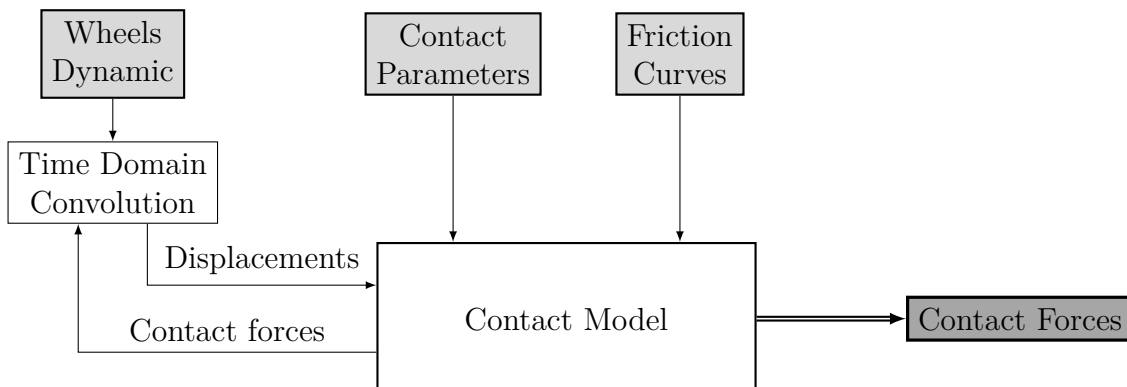


**Figure 2.5:** Engineering contact model for contact forces as presented in [15]. Inputs to the model are represented with light filled blocks, output is darker.

The procedure for calculating the contact forces over time can be outlined as follows, a more detailed description is found in [15, 29]. As a first step, the three inputs need to be generated individually, the first one being the wheel dynamics as described in 2.3 "Description of wheel dynamics". The contact parameters include the geometrical description of the discretized contact patches of both bodies in contact. The contact patch discretization also includes elastic half-space influence coefficients used to compute and adjust the contact pressures so that the vertical force equals the imposed vertical load in stationary conditions. The last input are the pre-compiled friction curves as described above. They are generated for each vertical force of interest, for each contact position, each friction coefficient and for

## 2. Theory

---

each rolling speed. From these inputs, the current contact forces are known, the iterative process of generating the contact forces for both wheels can be initiated using previous time step results, so that after a time convolution with the wheels dynamic the displacements can be sent again into the contact model to create new contact forces from those updated values. The calculation is truncated once the time limit set by the user is reached.

# 3

## Conceptual Design

The motivation for a conceptual design is to use the discussed influence factors from the literature study and quantify the range in which they are supposed to be implemented in the rig. This is done in a parameter study. Influence factors that are based on literature only are the normal force acting in the contact point and the lateral creepage. Less defined inputs to the study are the friction coefficient and the damping of the wheels. The contact geometry is chosen according to Section 2.1 "Squealing Generation Mechanisms". A factor that is completely undetermined is the geometry of both wheels. It is the main goal of the conceptual design to describe both wheel geometries in dependency of the other parameters involved.

As a first step, the wheel geometry of the lower wheel is fixed by using an already existing wheel. This enables a detailed analysis of the wheel dynamics and a comparison to the FE method introduced in Section 2.3 "Description of wheel dynamics".

### Description of the Dynamic Wheel Response

A FE model is built based on the lower wheel geometry and a modal description of the wheel is calculated as described in Section 2.3 "Description of wheel dynamics". The actual wheel response is then measured and compared to the simulation.

### Finite Element Method

In the FE model, 79 modes were found in the frequency range up to 20 kHz for the lower wheel. This frequency range is chosen since at this point, it is unclear at which frequencies squealing can be expected to occur. Modes with up to 14 nodal diameters were found. This includes axial modes with up to three nodal circles, radial modes with up to two nodal circles and circumferential modes with up to three nodal circles. A comprehensive overview for the lower wheel is presented in Figure 3.1.

Mode shapes up to 10 kHz are presented in the Figures 3.2, 3.3 and 3.4. Presented is only half the cross section, and only the displacements in axial and radial direction are shown. Figures 3.5 and 3.6 give examples of the vibration patterns for a radial and an axial mode. Since the wheel is not mirror-symmetric in axial direction, the radial mode shapes contain motion in the axial direction and vice versa. The circumferential mode shapes are difficult to distinguish as no displacements in circumferential direction are plotted. This pattern of modal behavior and distribution over frequency is representative for a steel wheel and more generally any flat disk.

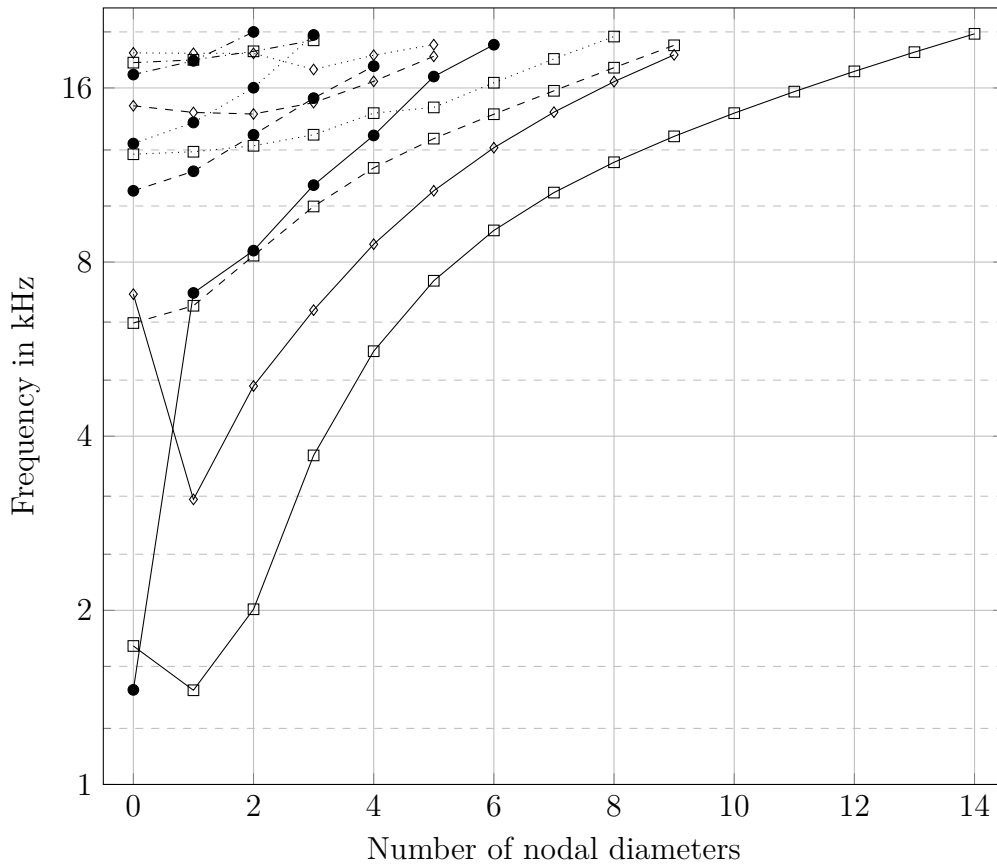


**Figure 3.1:** Eigenfrequencies of the lower wheel up to 20 kHz calculated from a FE model. Axial modes are presented with square marks, radial modes with black circles and circumferential modes with diamonds. Solid, dashed, dotted, and dash-dotted lines represent respectively zero, one, two and three nodal circles for each type of mode.

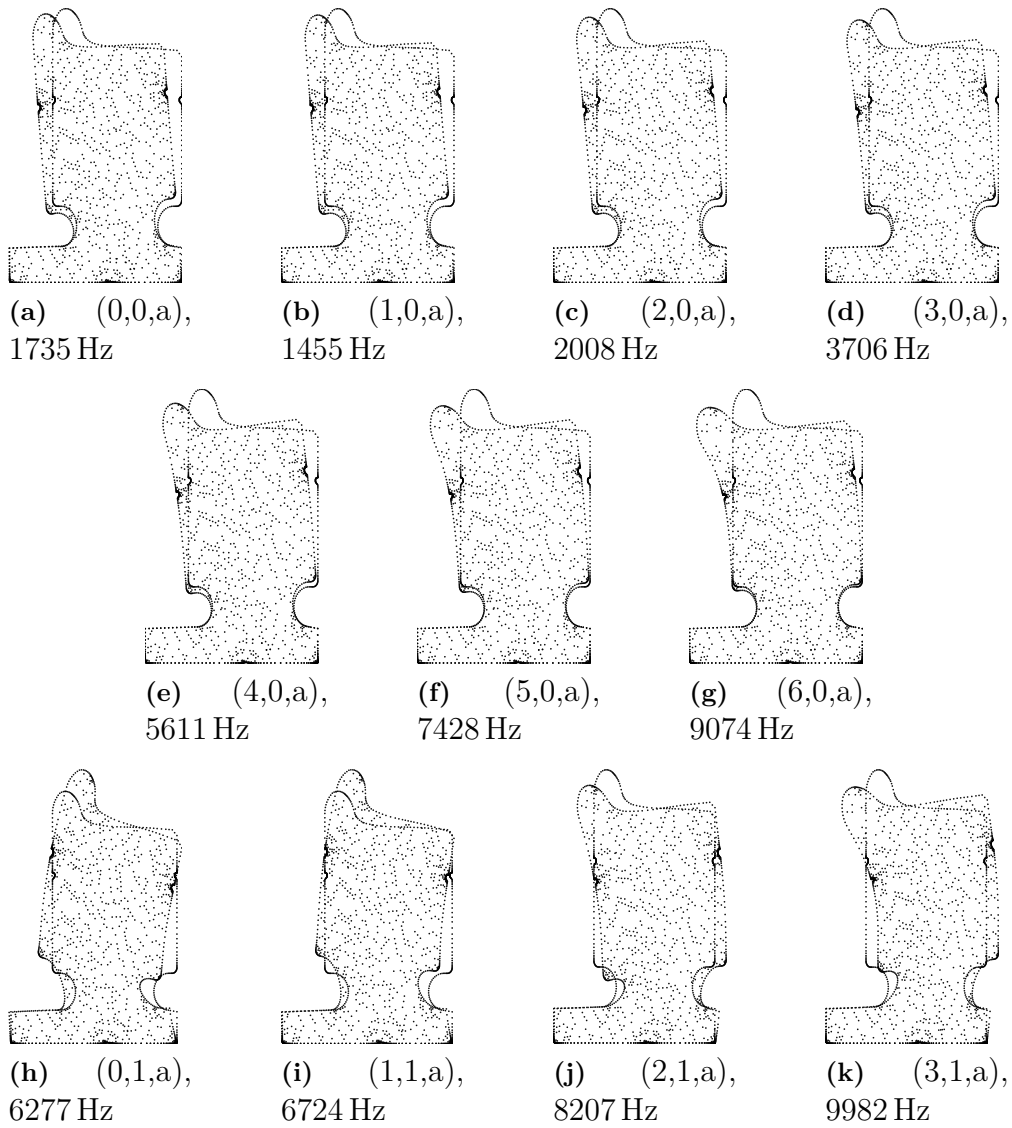


**Figure 3.2:** Axial mode shapes of the wheel up to 10 kHz.

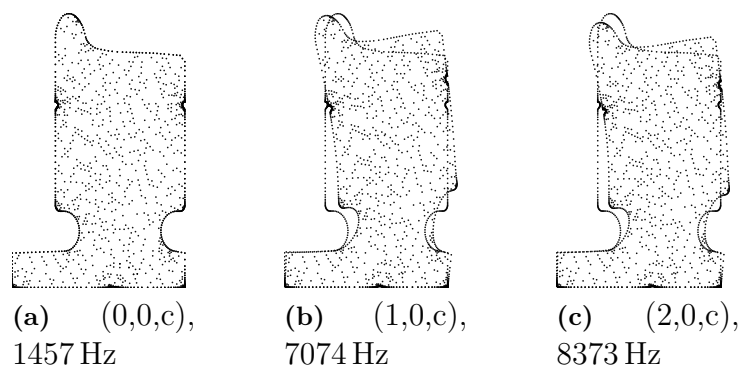


**Figure 3.3:** Circumferential mode shapes of the wheel up to 10 kHz.

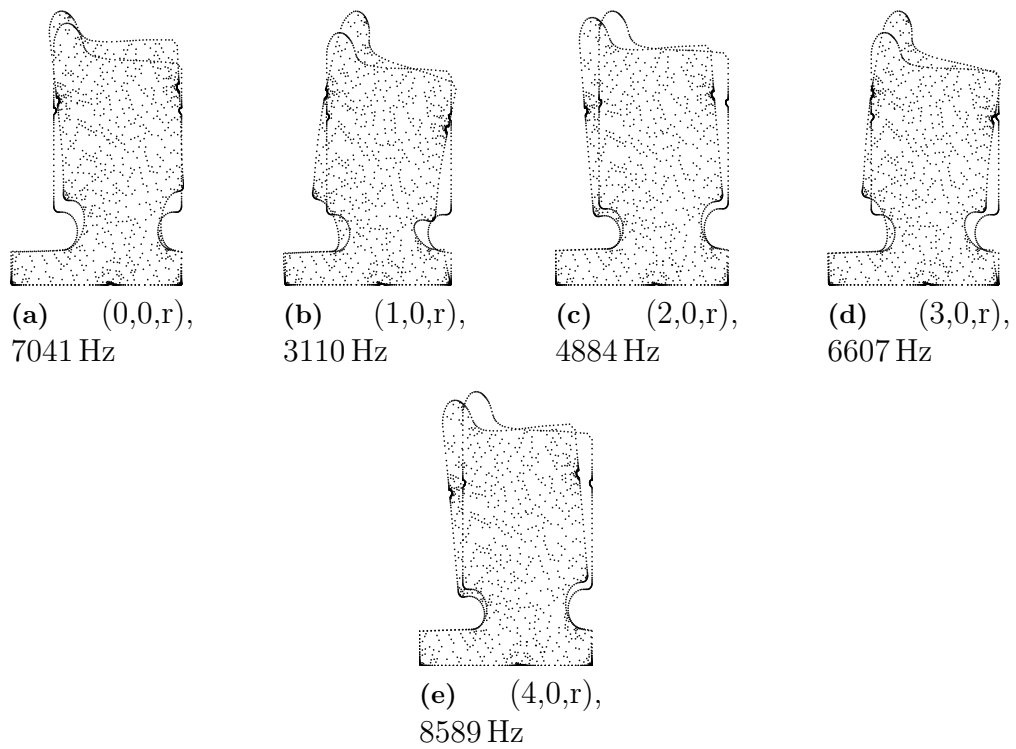


**Figure 3.4:** Radial mode shapes of the wheel up to 10 kHz.

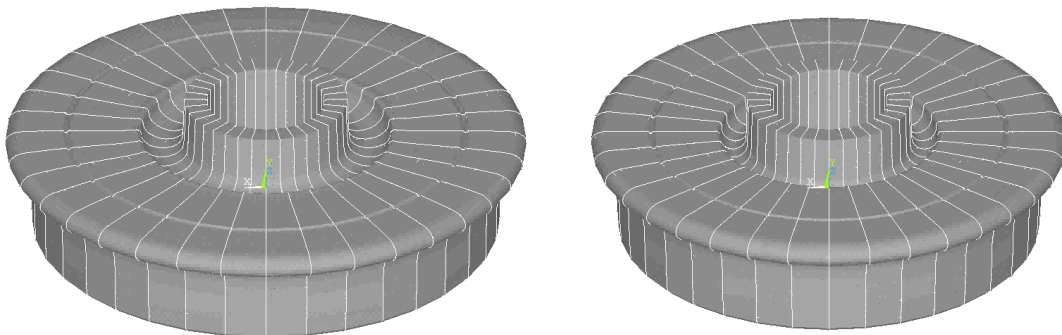


**Figure 3.5:** Lower Wheel Radial Mode at 6607 Hz

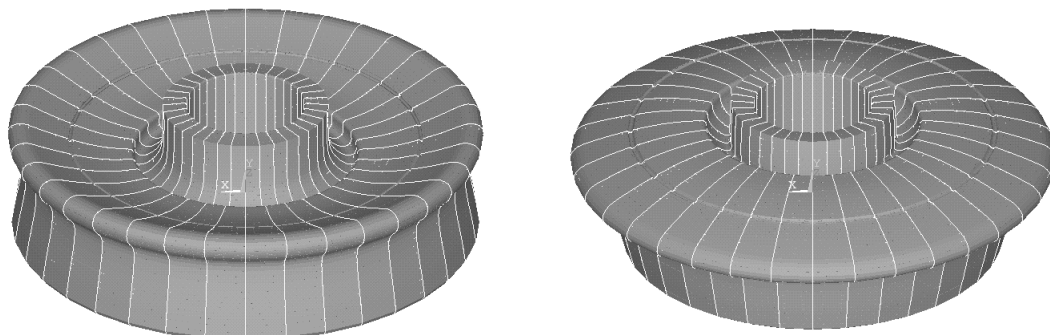


**Figure 3.6:** Lower Wheel Axial Mode at 7074 Hz

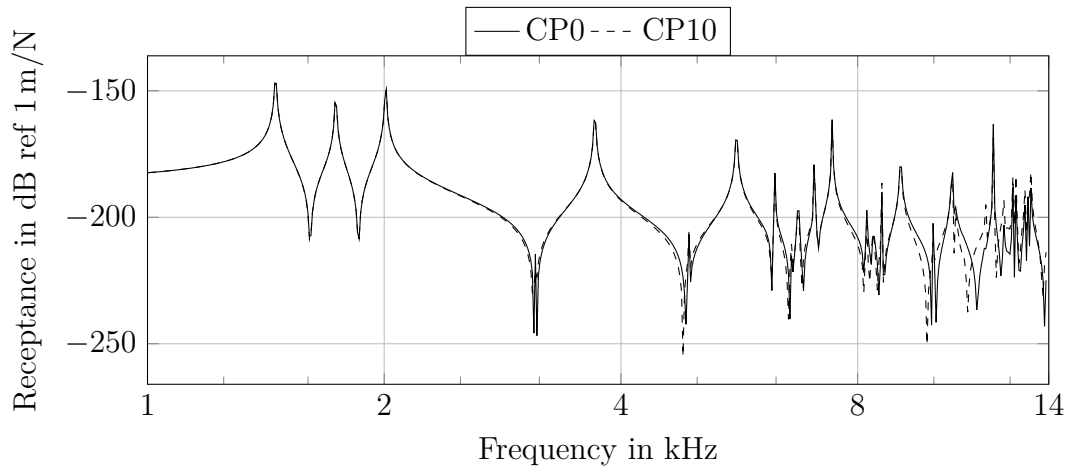


**Figure 3.7:** Comparison of calculated receptances for the lower wheel. The abbreviations CP0 and CP10 describe different contact points, as outlined in Section 3.2.1.

The modal superposition of the presented modes leads to the receptance as shown in Figure 3.7. The receptances of two different contact positions are presented, as it is elaborated on in Section 3.2.1. It is visible that the contact position mainly influences the higher frequencies.

## Measurement

Since an existing wheel is used as the lower wheel, it is available for model validation purposes. For this, the wheel receptance was measured. The measurement took place in May 2017 at the Vibroacoustic Lab at the Technical Acoustic department, Chalmers University of Technology. The wheel is suspended through its center using ropes. Two accelerometers are attached to the wheel, one radially, central on the tread and one axially on the side of the wheel, close to the outer edge. The input mobility is determined by impact hammer measurements. The wheel is hit close to the accelerometers to get the axial and radial input mobility as well as the transfer mobility. Since the steel wheel is a rather resonant system, the response is recorded for 5 s. Each position is hit at least 8 times and the measurements are averaged. The equipment used for this measurement includes

- Three charge accelerometers, type 4393V
- One charge accelerometer, type 4374V
- One B&K charge amplifier, Nexus type 2692, low noise version
- One Hammer B&K type 8203

Acquisition of the data is done using the software TAMARA.

For the validation, a FE model is created according to the description above, using a drawing provided by the manufacturer. Since the wheel at the point of the measurement is not mounted on an axle but freely suspended, the boundary conditions in the FE model are adjusted. After FE modeling and modal superposition as described in Section 2.3 "Description of wheel dynamics", the input inertance is generated and drawn in Figure 3.8 for the axial and radial direction and compared

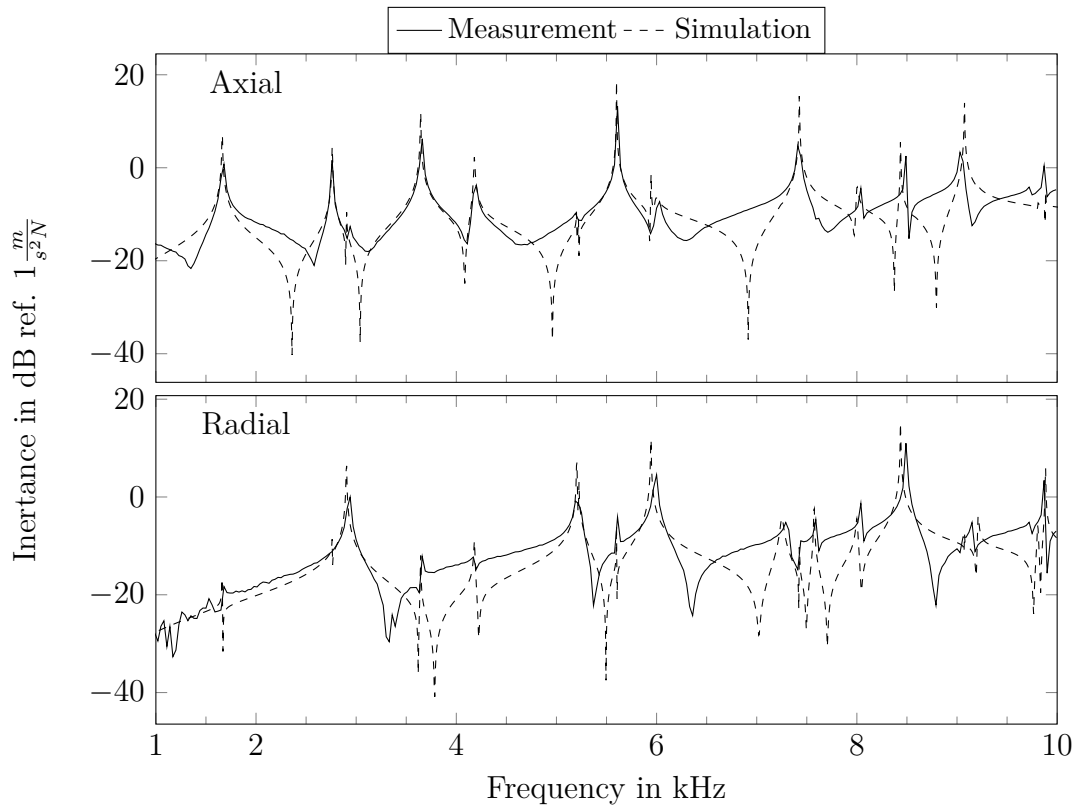


**Figure 3.8:** Comparison of measured and simulated inertances for the lower wheel.

to the measurements.

The modal damping of the FE model is then adjusted manually to match the measurements. It is observed that the actual damping of the modes in many cases is lower than the assumption based on Thompson [3], often by a magnitude 10.

One general comment on those results is that the frequencies, in terms of modal peak positions, fit quite nicely. From those results, it is clear that if one manages to adapt the modal damping to the measurements, a good match between the model and the measurement is achieved. It is therefore assumed to be a valid input to the following simulations.

## Parameter Study

The following section describes the input data, the setup and the results of the parameter study. In the study, the time domain simulation model described in Section 2.4 "Description of the Time Domain Squealing Model" is used to evaluate the contact forces over time for every possible combination of the input parameters.

### Parameter description

As a first step, the parameters varied during the study are introduced. The motivation for their variation as well as the range and step size in which they are varied

are described in the following.

### **Railwheel Geometries (WG)**

The upper wheel, which is not an actual tram wheel but instead functions as the rail, is not described geometrically up to this point. The purpose of this parameter study is to find a geometry, that in combination with the lower wheel is likely to produce squeal noise in many circumstances.

For this, a basic geometry has been developed according to the following guidelines. Firstly, the geometry cross section is roughly designed after an actual rail profile, since then the rail wheel takes up approximately the same space on the other wheel. Secondly, the head curvature is chosen according to Section 2.2 "Scale-Down Properties of the Contact Patch", to create a contact patch that is close to reality. The necessary contact surface with the shaft is a criterion that determines the width and diameter of the central hole, see also Section 4.5.1.4 "Press fits". Flat profile areas simplify the attachment of damping materials and are therefore favored. The outside diameter is chosen to be smaller than that of the wheel to keep the dimension of the rig reasonably compact, but large enough to attach material to it.

From the basic geometry that was generated, variations are generated by reducing the thickness of the disk in 5 mm steps on both sides and in two levels. This approach was chosen because it is assumed a simple way of reducing axial stiffness and thereby shifting the eigenmodes. Figure 3.9 shows the different geometries. Wheel geometry one (WG1) in Figure 3.9a can be seen as the basic geometry. Wheel geometry two (WG2) has the first reduction of thickness on the first level, meaning that at the lower and upper end of the straight profile section, the thicker profile remains. This becomes clear when comparing with wheel geometry (WG4), Figure 3.9d, where the thickness is reduced on the whole length. Wheel geometry 3 (WG3) shows a first level reduction and wheel geometry 6 (WG6) a second level reduction on both sides. Wheel geometry 5 (WG5) has a first level reduction on one and a second level thickness reduction on the other side.

At the point of the design it is unclear, which effect the symmetry of a wheel plays and therefore three symmetric (WG1, WG3 and WG6) and three unsymmetric geometries are used.

For these wheel geometries, the receptances are generated in the same way as for the lower wheel. Hence, a modal description of these wheels is done and the result can be seen in Appendix A.1 "Upper Wheel Geometries Eigenmodes". Receptances for the wheel geometries WG4, WG5 and WG6 are shown in Figure 3.10. Due to the related geometrical shapes they present a similar modal behavior.

### **Contact Positions (CP)**

As the contact position of the wheel on the rail changes during driving and furthermore the contact point impulse response as an input into the calculation changes with the contact position as seen in Figure 3.7, this is an important parameter. In reality, the bogey moves sideways on the rail, on which it is in contact very close to the highest point. To represent this, three contact positions for the wheel and one contact position for each rail wheel have been defined.

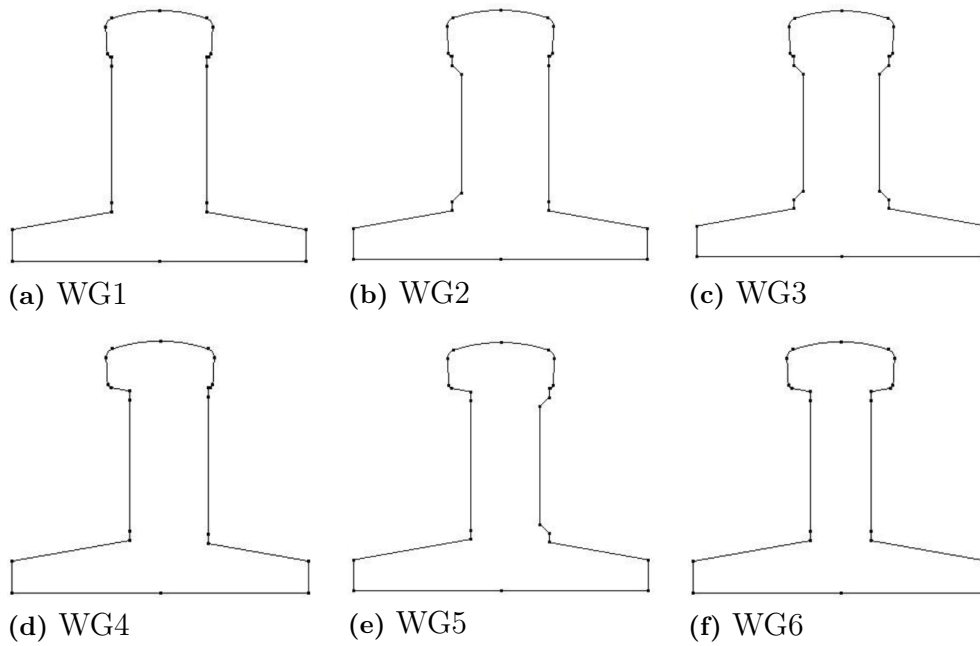


**Figure 3.9:** Researched geometries for the upper wheel. Only half the outline of the cross-section is shown.

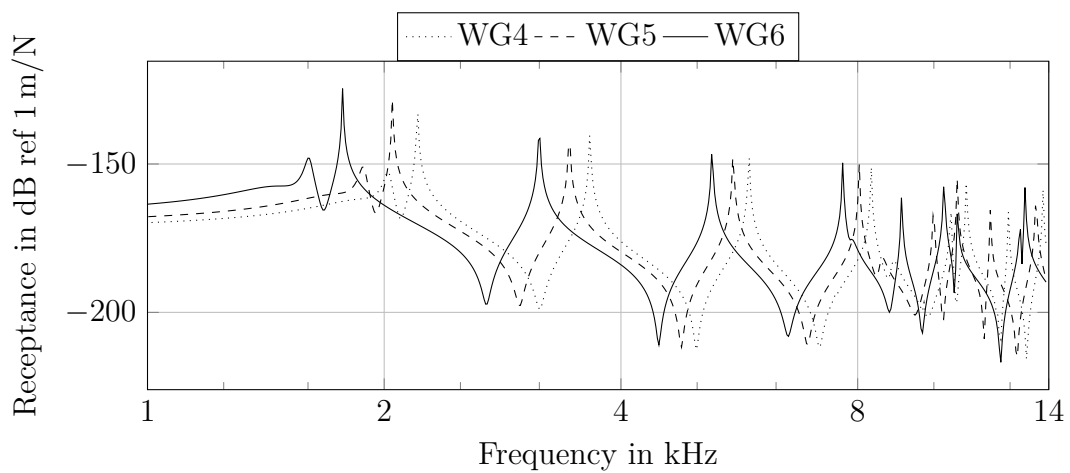


**Figure 3.10:** Comparison of Calculated Receptances for the Rail Wheels.

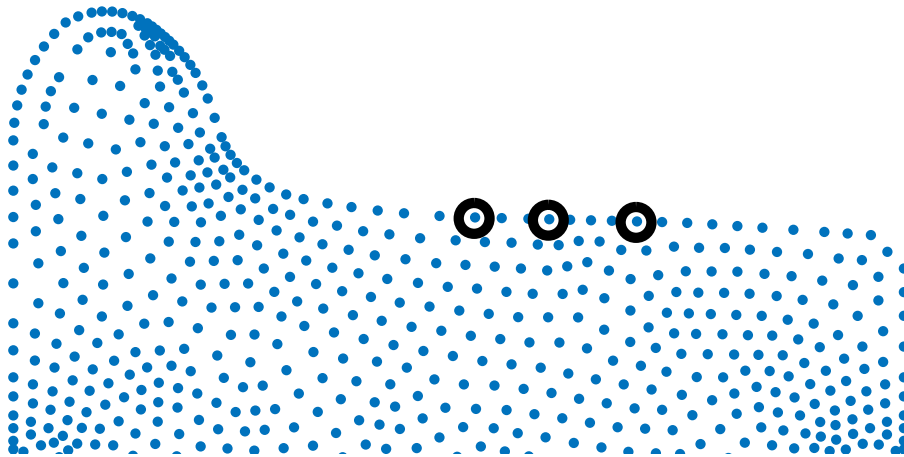


**Figure 3.11:** Nodes from FE model outlining the cross section of the wheel head geometry. The black circles mark the contact positions CP0, CP10 and CP25, from left to right.

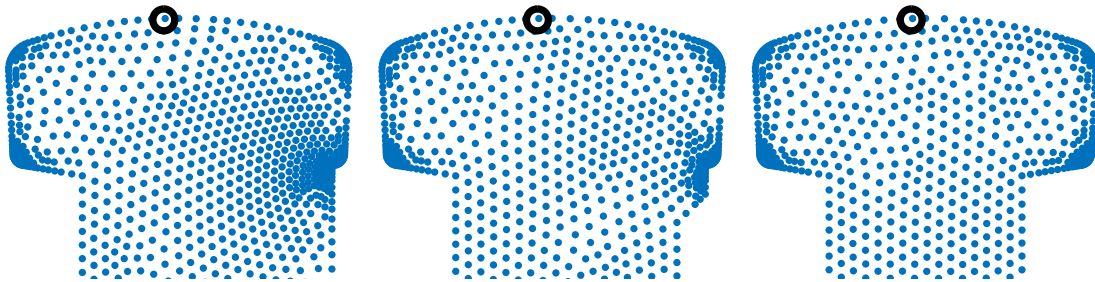


**Figure 3.12:** Nodes from FE model outlining half of the cross section of the rail wheel heads. The black circles mark the contact position. From left to right, the geometries 4, 5, and 6 are shown.

Figure 3.11 shows the considered contact positions on the lower wheel. Each blue dot marks a node in the FEM-calculation described in Section 3.1.1 "Finite Element Method", and the receptances were evaluated at the nodes that are circled. The left contact position corresponds to the constructed zero position and is therefore called CP0. The contact position 10 mm to the right is called CP10 and the one 25 mm to the right from the zero position is called CP25. For the rail wheel or upper wheel, the contact node closest to the central node is chosen for the evaluation. It was found that when choosing the node in the exact center of the head curvature, the receptances differed substantially from close by nodes, a finding with is not included in the report and not entirely explained. However, the contact will due to the sloped head curvature of the lower wheel not be exactly in the center anyway, and so the receptance at the node next to the center is presumed more realistic.

### Friction Coefficient (FC)

The friction coefficient between the two wheels is dependent on some factors that are unknown before the physical test, like the exact surface roughness or the influence of

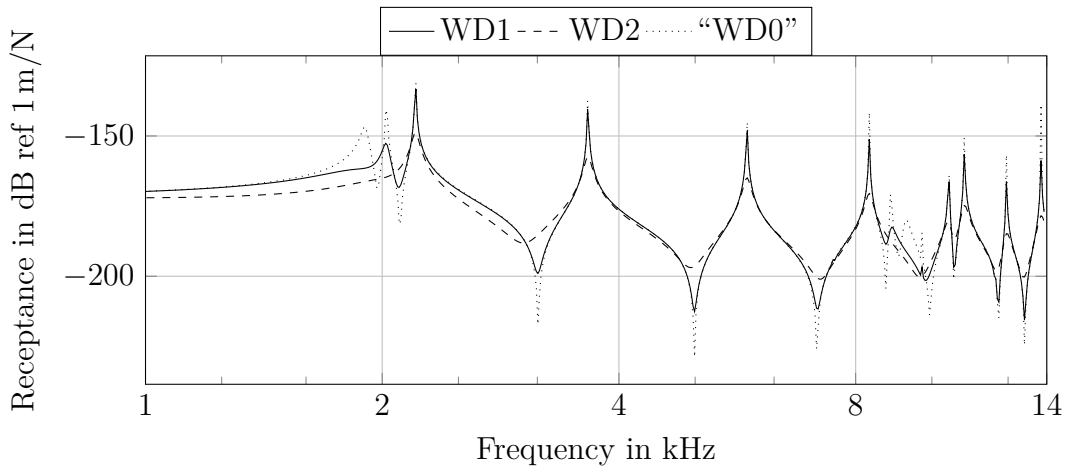


**Figure 3.13:** The influence of the chosen modal damping coefficients on the receptance.

the surface hardening. Furthermore, it is possible to change the friction coefficient during operation using lubricants. For these two reasons, a wide range of friction coefficients is tested, namely 0.15, 0.3, 0.45 and 0.55. This covers the range of the test rig described in [10]. The friction coefficient is in the following often abbreviated as FC.

#### Wheel Damping (WD)

The wheel damping of the upper wheel as introduced in 2.3 "Description of wheel dynamics" is difficult to predict accurately, especially due to the likely use of at this point undefined damping materials. As a consequence, a rather wide range of wheel damping settings cover possible damping scenarios. Adapting the guidelines to modal wheel damping by [28], the basic modal damping is dependent on the number of nodal diameters  $n$ .

To represent the damping layers attached to the wheel, the suggested modal damping coefficients are multiplied with the chosen factors 10 and 100 to generate two different damping settings. The effect can be seen in Figure 3.13, where the different receptances are plotted for the wheel geometry WG4 at 50 km/h. The two used sets of wheel damping coefficients WD1 and WD2 correspond to the factors 10 and 100 respectively. Since the effect of the upper wheel damping on the occurrence of squealing is not entirely certain and it in addition might be changed during operation, the focus of the parameter study will be to pick a wheel geometry that shows the lowest influence on damping.

#### Normal Force (NF)

In the contact point, normal forces up to 35 kN are introduced in the simulations. This corresponds approximately to half the wheel load of a light metro train [30]. Reducing the maximum normal force that way leads to a reduction of the necessary supporting rig geometry and is therefore desired. The normal load is researched in

**Table 3.1:** Lateral creepage steps and according angles.

$\eta$ in %	-2.2	-1.9	-1.4	0.5	0.8	1.1	1.4	1.9	2.2
$\alpha$ in °	-1.25	-1.1	-0.8	0.3	0.45	0.6	0.8	1.1	1.25

**Table 3.2:** Overview over used input parameters in both parameter studies. The changes after the pre-study are indexed with “+” for added parameters and “-” for removed parameters.

NF	LC	FC	RS	WG	WD	CP
15, 20, 25, 35	0.5 <sup>+</sup> , 1.1 <sup>+</sup> , $\pm 1.4^+$ , $\pm 1.9$ , $\pm 2.2^+$	0.8 <sup>+</sup> , 0.15 <sup>+</sup> , 0.3, 0.45 <sup>+</sup> , 0.55	30 <sup>+</sup> , 50	1 <sup>-</sup> , 2 <sup>-</sup> , 3 <sup>-</sup> , 4, 5, 6	1, 2	0, 10, 25 <sup>+</sup>

four steps, 15 kN, 20 kN, 25 kN and 35 kN, later referred to as NF15, NF20, NF25 and NF35.

### Lateral Creepage (LC)

The lateral creepage is introduced as an angle between the two wheels in the horizontal plane. The relation between the angle  $\alpha$  and the lateral creepage  $\eta$  is  $\eta = \tan(\alpha)$ . The lateral creepage is evaluated at nine settings, listed in Table 3.1. The largest creepage of 2.2% is chosen based on [10] and [7].

### Rolling Speed (RS)

Since squealing is mainly problematic in urban areas, the maximum rolling speed is limited to 50 km/h. As a second setting, 30 km/h is investigated. The two settings will be referred to as RS30 and RS50.

### Study Setup

Due to the large amount of parameters and the considerable calculation time for each simulation, the parameter study is split into a pre-study and a main-study. The idea is to assess the squealing behaviour of all wheel geometries with a reduced set of parameters in the pre-study, to reduce the number of researched wheel geometries in the main-study.

Table 3.2 lists which parameters were included in which study. Multiplying the number of parameters of each category gives the number of necessary calculations, being 384 for the pre-study and 5184 for the main-study. Conducting the pre-study lead to the removing of the three wheel geometries WG1, WG2 and WG3 from the study, halving the calculation time.

The time domain solution of the contact problem is done using the simulation model described in Section 2.4 "Description of the Time Domain Squealing Model", adapted to work with two wheels instead of a wheel rolling on a rail. Two further changes in the calculation are made for this parameter study, the first one being the adaption of

**Table 3.3:** Discretization settings in pre- and main-study.

Input	Unit	Pre-study	Main-study	Main-study
$V$	km/h	50	30	50
$dx$	$\mu\text{m}$	250	312.5	500
$dt$	$\mu\text{s}$	18	37.5	36
$f_s$	kHz	55.6	26.7	27.8
$f_{up}$	kHz	21.4	10.3	10.5

the discretization. By specifying a rolling speed  $V$ , there is a fixed relation between the spatial discretization  $dx$  and the time resolution  $dt$ . The sampling frequency  $f_s$  then leads to the upper frequency limit of the analysis  $f_{up}$

The pre-study has been executed with a high upper frequency limit. This is because firstly, the effect of using two wheels instead of one wheel on a rail was not clear and secondly, the substantial decrease in size of the wheels in comparison to standard wheels was assumed to shift the modes and squealing frequencies up. It was found that squealing mainly happened below 10 kHz, and so for the main-study the discretization could be adjusted, optimizing the calculation time. Table 3.3 gives the rolling speed and spatial discretization with their consequences for both the pre- and the main-study.

As a second step in reducing the total calculation time, a truncation criterion is introduced after conducting the pre-study. It is observed that in cases where no squealing occurs, the lateral force converges to one value and does not change for several consecutive time steps. This is not found for squealing cases. Figure 3.14 can be used to verify this. Each simulation from the pre-study is represented by one dot. The horizontal axis classifies the results by their root-mean-square (rms) force level in the last 150 ms of the simulation, a procedure which is explained more deeply in Section 3.2.3.1 "Evaluation Method". The vertical, dashed line separates the squealing-cases on its right from the other cases. The vertical axis gives the maximum number of consecutive identical force values for each simulation. It can be seen that for squealing cases, this number is considerably lower than the introduced truncation criterion of 1000 consecutive identical force values. During simulation, the calculated side force is tested against this criterion every 4000 time steps. Summing the absolute differences of the actual force value from the 1000 previous force values always gives a nonzero result, except in case all values are exactly the same. In the main-study a resulting zero leads to truncation of the simulation and the classification as a non-squealing case.

The total simulation time is 3.5 s in both the pre- and the main-study, based on the procedure described in [7].

## Study Results

A typical result for a squealing case is shown in Figure 3.15. The graph shows the lateral contact force  $F_y$  over time. The smooth build-up of the side force in the first 0.2 s is due to a run-up process in the model that is not further discussed here.

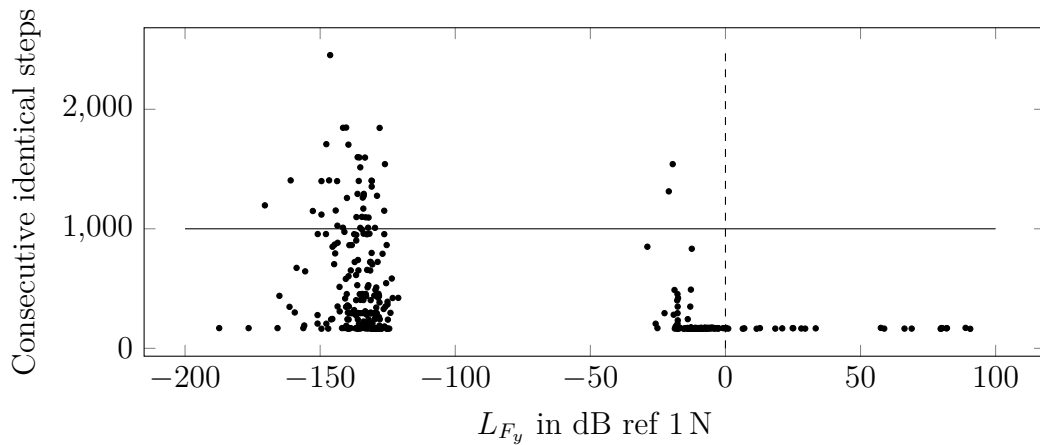


**Figure 3.14:** Legitimation of Calculation Time Optimization by breaking the simulation after 1000 time steps with identical results.

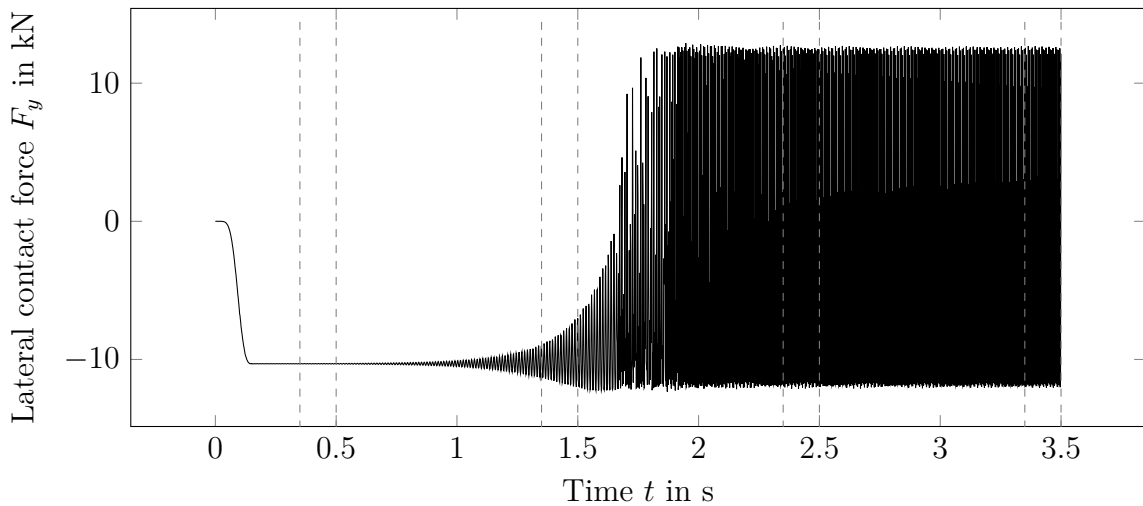


**Figure 3.15:** Example result of time-domain solution of the contact problem for a squealing case.

The build-up is followed by a period of small variations around the static side force, which in turn is followed by a large increase of the force. At about 2 s the force reaches the maximum transmissible side force in both directions and is such limited in its increase.

### Evaluation Method

The squealing is evaluated in four time ranges of each 150 ms in 1 s distance, indicated with dashed vertical lines in Figure 3.15. To characterize the force fluctuation, a time-averaging within these time ranges is carried out using the root mean square method:

$$F_{y,rms} = \sqrt{\frac{1}{T} \int_{t_1}^{t_1+T} (F_y(t) - \overline{F_y})^2 dt} \quad (3.1)$$

**Table 3.5:** Number of squealing cases counted for each set of simulations in the main-study.

WG4	WG5	WG6
404	419	381

The criterion, that classifies a result as a squealing case is that this rms force exceeds 0 dB in the last time range, 3.35 s to 3.5 s, when represented as a level, using the equation

$$L_{F_y} = 20 \log \frac{F_{y,rms}}{1N} \quad (3.2)$$

The squealing criterion is the same as described in [7]. The first three time ranges are evaluated in the main study to further characterize the squealing.

#### Pre-study Results

The 384 simulations in the pre-study led to 26 results that fulfill the squealing criterion. These are distributed among the wheel geometries according to Table 3.4. It becomes clear that wheel geometries WG4, WG5 and WG6 show a substantially higher potential to squeal than the others and are therefore chosen as candidates for the main-study.

**Table 3.4:** Number of squealing cases counted for each set of simulations in the pre-study.

WG1	WG2	WG3	WG4	WG5	WG6
0	1	0	6	8	11

#### Main-study Results

The 5184 calculations in the main study lead to 1204 results that classify as squealing. Table 3.5 shows the distribution of squealing cases among the wheel geometries. Finding a wheel geometry that supports the occurrence of squealing the most, only based on this table, would be insufficient, since the squealing cases are quite evenly distributed between the wheels. For that, a more in-depth analysis of the results is made. Figure 3.17 shows every simulation for the wheel WG5 structured as explained in Figure 3.16. For the wheel geometries WG4 and WG6 these plots are attached in Appendix A.2 "Parameter Study Results". It is apparent that the occurrence of squealing is not easily predictable due to the interdependence of all parameters. As a general trend, it is seen that the likelihood to squeal increases with increasing normal force as well as with an increasing friction coefficient. It is assumed that this is due to the higher energy input at higher force and friction coefficient. However, this trend is not seen for higher rolling speed, which could also be interpreted as a higher energy input. Furthermore, for the lateral creepage a opposite trend is seen, the number of squealing cases decreases with increasing positive lateral creepage. For negative lateral creepages, almost no squealing occurs. Contact point CP25

**Table 3.6:** Proportion of squealing cases for each damping setting as an indication of the influence of the upper wheel damping. For WG4 a comparatively larger dependency on the damping is observed.

WD	WG4	WG5	WG6
1	74%	64%	60%
2	26%	36%	40%

**Table 3.7:** Proportion of squealing cases for each friction coefficient as an indication of its influence. No notable influence with regard to the wheel geometry is found.

FC	WG4	WG5	WG6
0.15	1%	1%	1%
0.30	20%	17%	16%
0.45	36%	37%	37%
0.55	43%	45%	46%

seems to promote squealing more than the other two positions, especially at lower force inputs or lower friction coefficients.

Choosing one of the wheel geometries for use in the rig is done by considering specifically the influence of the wheel damping, the friction coefficient and the timing of the squeal occurrence. As described in Section 3.2.1, a low influence of the wheel damping on the occurrence of squealing is desired. Table 3.6 shows the percentage of squealing cases for each wheel geometry in dependency of the wheel damping. In general, the lower damping setting WD1 leads to more squealing, but WG6 shows the least dependency here, followed by WG5.

The same strategy applies when considering the friction coefficient. As mentioned in Section 3.2.1, the actual friction coefficient is hard to foresee and therefore the wheel geometry with the least influence on that is wanted. Table 3.7 presents the percentage of squealing cases for each wheel geometry. No significant differences are found here.

Examining the resulting contact force over time showed that while some simulations qualifying as squealing cases develop the amplitude early in the process, others pass the criterion only in the last evaluated time range. It is assumed, that in reality, where the contact forces are exposed to external irregularities, a simulated, quick build-up is more likely to actually lead to squealing. Table 3.8 presents the proportion of squealing cases in dependency of the time for each wheel geometry. The wheels WG4 and WG6 show an earlier response than WG5.

Based on these evaluations, wheel geometry WG5 is chosen as the wheel geometry, because of its highest total number of squealing occurrences, the comparatively small dependency on wheel damping and the friction coefficient. One more reason is its non-symmetry which enlarges the possibilities of its application as a testing wheel.

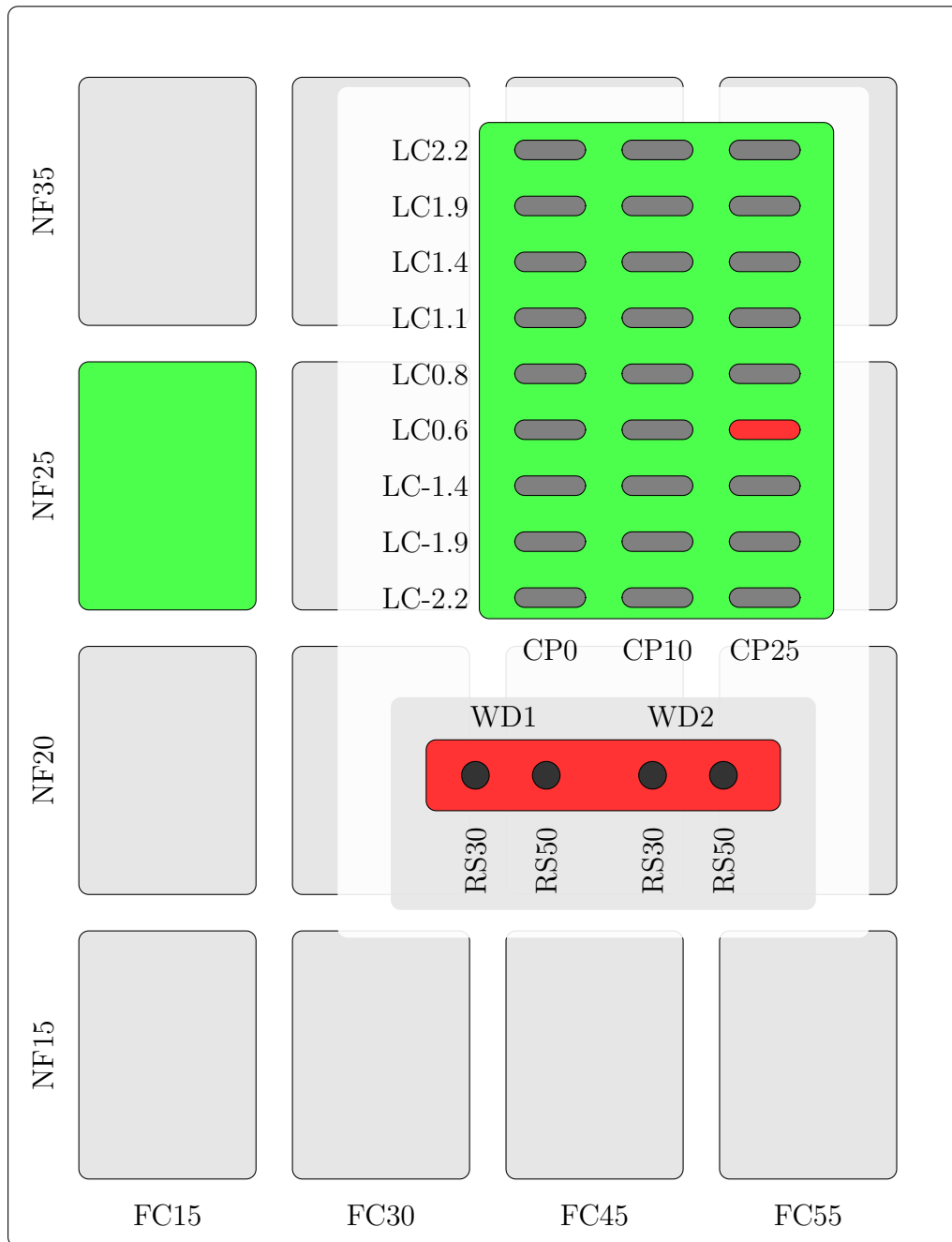


**Figure 3.16:** The arrangement of the results of the parameter study follows the schematic outlined above. Each result is represented by a single dot. The dots are organized in different level groups. The first level, depicted in light gray, clusters results with the same friction coefficient and normal force. Within these, results are categorized by their contact position and arranged vertically by their lateral creepage, shown as dark gray bars. In these bars on the third level, the individual results, represented by the circles, are organized by the wheel damping and rolling speed as shown.

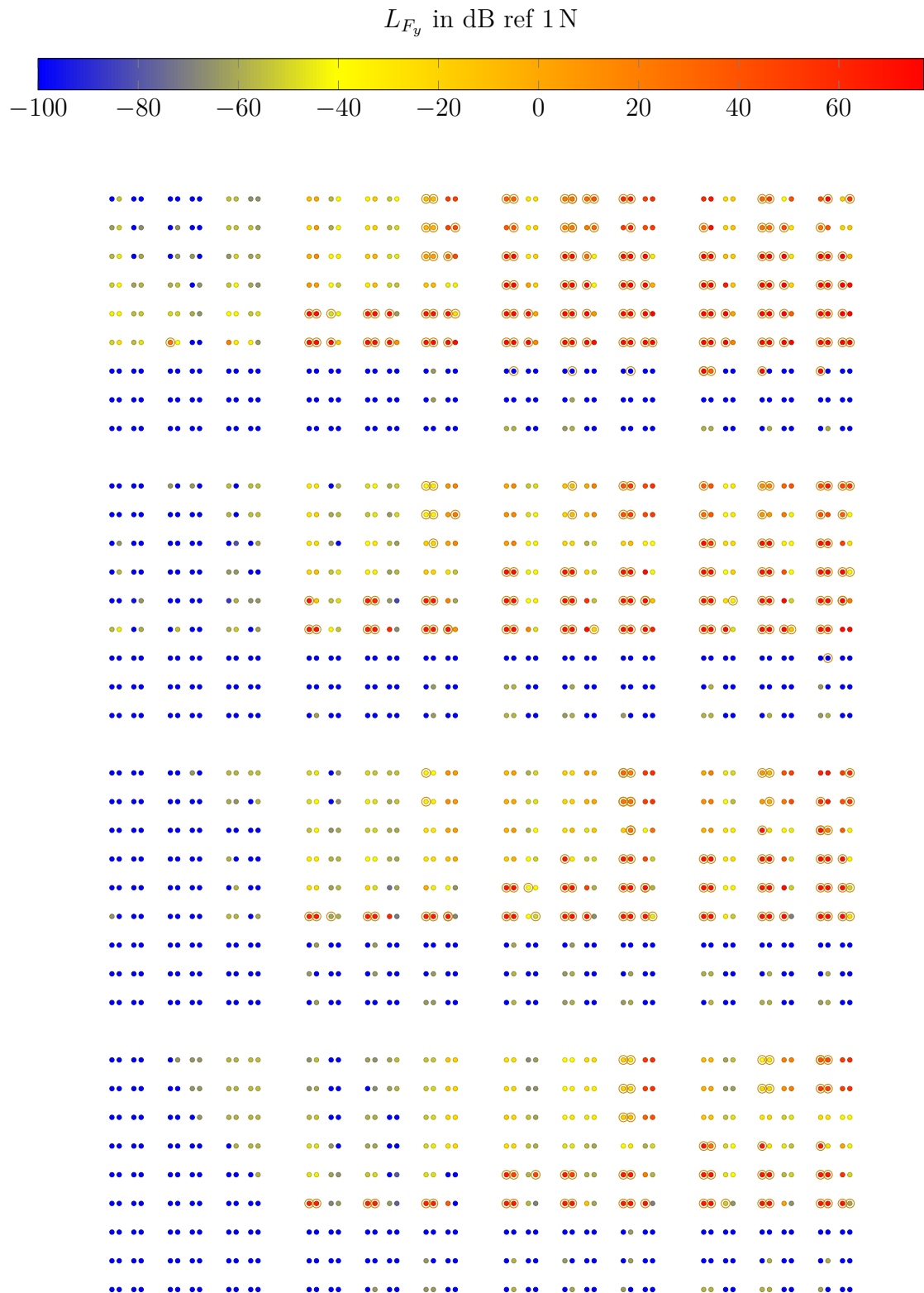


**Figure 3.17:** Result summary for simulations with wheel geometry WG5. Each dot represents one simulation, and the color of each dot indicates the time-averaged force level  $L_{F_y}$  in the last 150 ms of the simulation. Encircled results fulfill the squealing criterion.

**Table 3.8:** Proportion of squealing cases in dependency of considered evaluation time segment. It can be noticed that a high percentage of squealing occurs already in the early time segments.

Time	WG4	WG5	WG6
>0.35 s	82%	75%	85%
>1.35 s	93%	86%	95%
>2.35 s	97%	93%	96%
>3.35 s	100%	100%	100%

**Table 3.9:** Effect of removing potentially coupled modes on the occurrence of squealing for squealing at about 2020 Hz.

$F_{Y,rms}$ in dB		Upper Wheel Mode	
		present	removed
Lower Wheel Mode	present	13.80	-22.98
	removed	-59.86	-62.05

#### Side Study Mode Coupling

It is observed that the frequency content of the lateral force in squealing cases mainly has one dominant frequency. Generally, there are two main frequencies at which squealing occurs: at around 2020 Hz and 8580 Hz. A reason for this could lie in the coupling between modes. It was found that the lower wheel has an axial mode at 2008 Hz and a radial mode at 8585 Hz. The upper wheel likewise has eigenfrequencies close to the dominant squealing frequencies, with axial modes at 2048 Hz and 8576 Hz. One result has been chosen for each squealing frequency. Figure 3.18 shows the side force over time in Figures 3.18a and 3.18c and the frequency content in the time range 3.35 s to 3.5 s in Figures 3.18b and 3.18d. In the frequency plots, the modes in question are indicated by dashed (axial modes) and dotted (radial modes) lines.

To see the influence of these modes on the occurrence of squealing, for each squealing case additional calculations are executed. In each additional calculation, one or both modes are removed from the receptances. The result is shown in the Tables 3.9 and 3.10. It can be seen that for both squealing cases, if one or both of the potentially coupled modes are removed, the squealing does not occur. As a consequence, it can be concluded that the interaction of the two modes does not have an influence. It can however not be concluded that the coupling of these two modes is the only reason for the squealing occurrence.

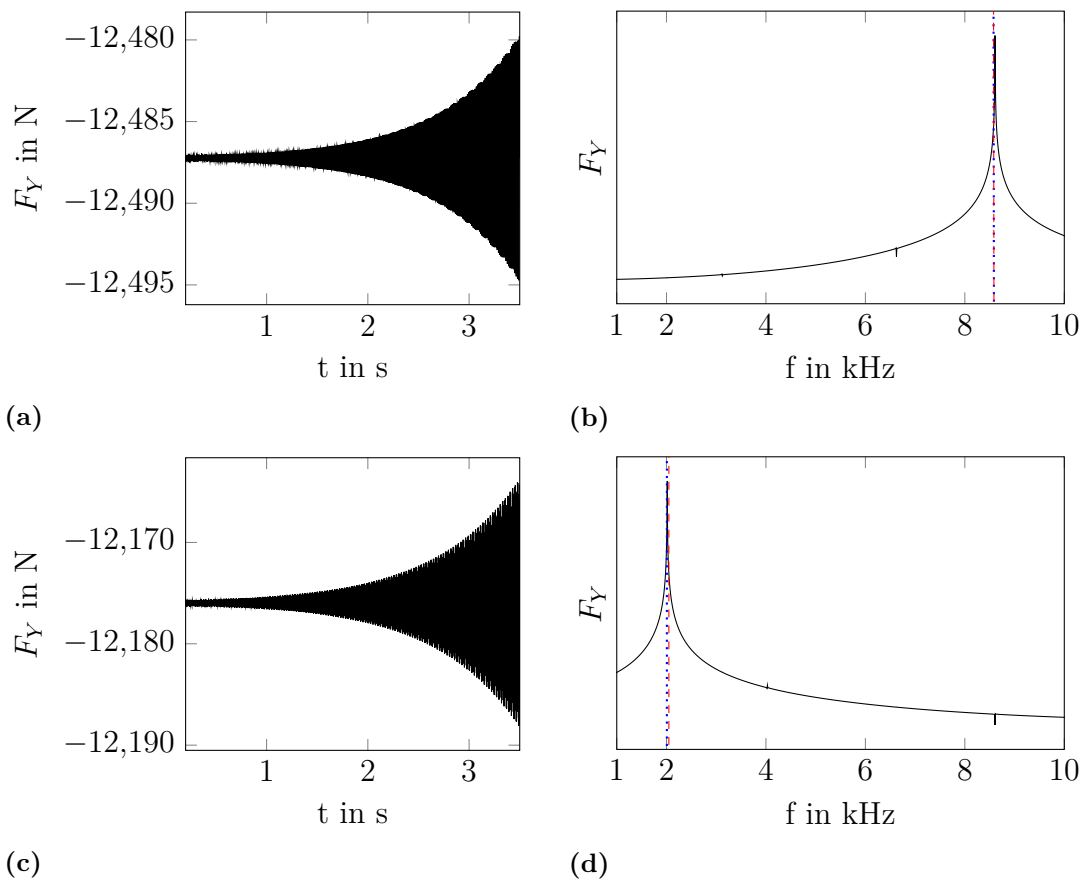


**Figure 3.18:** Influence of single modes on the occurrence of squealing. Figures (a) and (c) show the time domain response of the squealing cases. Rather low amplitude squealing cases were chosen since then the frequency response, seen in Figures (b) and (d) is mostly free from distortions by the limit cycle.

**Table 3.10:** Effect of removing potentially coupled modes on the occurrence of squealing for squealing at about 8580 Hz.

$F_{Y,rms}$ in dB		Upper Wheel Mode	
		present	removed
Lower Wheel Mode	present	18.03	-51.07
	removed	-54.84	-58.69

# 4

## Construction

In the construction chapter, the principal ideas for the setup of the rig are developed, the requirements towards loads are acquired, and the mock-up is described. For critical parts, analytical or finite element based safety calculations are carried out.

### Conceptual Construction

The first step in the construction is developing concepts which are the basis for further steps. This includes both concrete ideas that are to be implemented as well as considerations regarding topics that might be of interest in future expansions of the rig, and such need to be regarded in the construction.

### Kinematic Considerations

The way how the lateral displacement, the setting of the angle for the lateral creepage and the vertical motion necessary for the normal force are implemented in the rig can result in an interdependence between these motions. This occurs if both motions are to be realized at one of the wheels. Then, one has to decide which motion is set first, meaning it defines the change relative to the original state of the wheel. The other motion defines the change relative to the already altered state. This becomes clear in Figure 4.1. The original position is drawn solid, the first motion is presented in dashed lines and the other motion leads to the final setting of the wheel. The left graphic shows the case if the angle is set first, and the lateral displacement is conducted in the now rotated reference system. The right graphic shows the case in which the lateral displacement is set first and the lateral creepage is adjusted in this shifted reference system. In the left graphic, one can not change the angle of the wheel in its final position without also affecting the longitudinal position. In the right graphic, one can not change the lateral position normal to the final position. For this reason, it is decided to divide the motions between the two shafts. As it is more feasible to rotate the wheel that is not driven by the motor, the angle for the lateral creepage is set at the upper wheel while the lower wheel is shifted laterally.

### Outer Construction

The general construction idea is to use a combination of sheet metal plates and I-profile beams for the outer rig. The use of sheet metal has the advantage of being able to use laser-cutting as a fast and accurate manufacturing tool. Furthermore,



**Figure 4.1:** The kinematic interdependence when both the lateral displacement as well as the lateral creepage are achieved by one shaft. The rectangles represent wheel positions, where the solid rectangle is the original position, the dashed rectangle gives the position after the first motion and the dotted rectangle represents the final position.

when designing hooks and notches in an appropriate way, the assembly can be simplified and the relative positioning of parts can be improved. This is especially important for minimizing the angular error between the bearings of one shaft. The I-profiles provide a standardized and stiff way to connect the plates.

## Force Generation Mechanism

The normal force can be generated in several ways that each perform differently with regard to convenience and complexity of implementation. A hydraulic system is discussed, which could provide a very convenient use and the potential to change the normal force during operation. Its downside is the complexity of implementation. A pneumatic system that could provide both the required accuracy in setting the force as well as a high enough force could not be found. An electromagnetic force generation shows the same benefits as a hydraulic system, but again with the downside of complex implementation as well as potentially high energy costs. All methods above provide an emergency shutdown, in which the normal force is reduced in a short amount of time.

Another possibility is the use of a stack of springs which are tensioned by a screw, which is comparatively inconvenient in its use but gives the possibility of adapting the suspension stiffness and provides a straightforward implementation. The latter method is chosen for the test rig.

## Longitudinal Creepage

As referenced in Section 1.3 "Placement in actual research", the superposition of lateral and longitudinal creepage has an impact on the severity or occurrence of squealing. To introduce longitudinal creepage in this setup a braking of the non-driven wheel is necessary. The braking torque should not introduce large vibrations itself while being adjustable and accurate. Ways to achieve this are using a direct chain connection between the two shafts as described in [20], a second motor as described in [10] or possibly even more elaborate solutions. Friction-based braking solutions like disk breaks might introduce vibrations and interfere with the researched vibration due to squealing.

This design of the test rig does not include a designated longitudinal braking mechanism. However, a connection to a brake is prepared by extending the upper shaft,

leaving space for a coupling.

### **Vibration Isolation and Damping**

The driving unit and the squeal vibrations will transmit to the supporting structure. This can lead to unwanted radiated noise to the surroundings. Since this is a working research facility and to ensure higher quality measurements, this radiation should be controlled. This can be achieved by placing vibration isolation on the structure. A decoupling of the vibrating parts from the frame is considered not expedient since that would introduce unwanted clearances and make the vibrating system more difficult to describe in models.

A location where damping material could be applied is inside the I-profile beams shown in Figure 4.7. If placed over the whole frame, a surface as large as  $2.88\text{ m}^2$  of damping layers can be achieved, considering only the inner part of all possible profiles. Damping material can also be applied on parts that are not fixed in space, that are free to rotate or translate, but still radiate unwanted sound from induced vibrations. Those elements closer to surfaces of the wheels, could receive damping material up to  $1.05\text{ m}^2$  if available space is found without disturbing the ongoing studies.

To decouple the rig from the building by preventing vibrations to be transmitted through the rig feet to the ground, isolator springs can be used. Assuming only vertical motion and vibration of the rig, a single degree of freedom model could be used to design the isolator. Due to the considerable mass, even with rather stiff isolation material, a quite low resonance frequency could be achieved. This could result in a substantial decoupling for frequencies in the order of the squealing occurrence.

For the damping of the upper wheel, different concepts exist. A simple method is attaching a material with a high loss factor to the sides. It can be adjusted by changing its material properties. The damping can be tuned to specific frequencies by using sandwich layers. One further way that is described as functioning is delineated in [19]. Here, several layers of thin sheet metal plates are attached to one wheel, dissipating the vibrational energy.

### **Measurement Concepts**

Several quantities are to be measured in the rig, not only for collecting data for the ongoing studies but also for monitoring the state of the rig.

Some of these quantities are directly available, for instance the motor speed and torque. The direct acquisition of these data is recommended if possible. If direct output cannot be produced, strain gages can be placed around the driving shaft to estimate the torque, and an optical incremental encoder can be used to measure rotational speed. The counterpart for the optical sensor can be designed such that the angle of the shaft is known at all times. For such a device, the axle of the upper wheel is designed longer in the case such an encoder was to be attached.

The force input into the system as well as the forces acting in the rig are of interest for both monitoring and squealing research. A passive element indicating the input

force is the position of the screw head compressing the springs. An active element like a force sensor can be placed between the press stamp and the cage holding the upper wheel axle. An option to measure forces in almost any position of the rig is the use of strain gages. This is the intended method for measuring the lateral force in the contact point, by placing strain gages on the shaft.

Static measurements to control the position of the two wheels are proposed here. Those quantities do not need to be real-time monitored as they are fixed during the rig operation. Two main parameters are to be considered here, the angular position representing the angle of attack between both wheels, and the lateral position of the contact patch on the lower wheel tread. Regarding the angular position of the upper cage, a visual system similar to the rotational disks on a micrometer is an option. This system is only used to set the value of the lateral creepage using the following formulas. An accuracy of approximately  $0.05^\circ$  can be obtained with two rings are placed on the edges of the circular shape top disk (see Figure B.21) with for example respectively 81 and 90 marks. The lateral position of the contact patch is to be measured using a caliper. The process can be simplified by providing small holes in the bearing housing lids, which provide a fixed reference surface.

Quantities of interest for squealing research are the vibrations in the contact the and emitted noise. Measuring vibrations requires accelerometers on the wheel. However, the signal cables are an issue because of the wheel rotation. There are two solutions, either using a wireless device to transmit the signals or to use a slip ring that transfers signals from a ring rotating with the shaft to a static brush which is slipping on the ring. The first option needs extra space on the sides of the wheel so the device can be attached. The second one requires changes on the shafts. With accelerometers glued to one side of the wheel, all signal cables need to be guided to the end of the shaft through a central hole. The slip ring is placed at the tip of the axle, flush mounted inside the hole where the rotating cables come out. Slip rings can have multiple channels if required and could also be used to transfer an input signal to for example power a shaker or a piezo-stack. Since on one side, the shaft is connected to the motor, this path is only planned for the other side of the wheel. If it is of interest to measure or input signals on the other side, a cable can be transferred through a hole in the wheel. The hole should be small enough to not influence the global response of the wheel in the frequency range of interest.

## Motor Coupling

The way the motor is coupled to the rig has consequences for the general setup as well as the vibrational interaction between the motor and the rig. Since in the rig, squealing as a self excited vibration is to be researched, any external vibrations can possibly harm the build up of these vibrations. For this reason, it is not recommended to use any torque-converter like a gearbox or a belt drive, since these are likely to introduce ripples in the torque or in the case of a belt drive a whole new vibrational system.

However, electric motors by default introduce torque ripple as well, which is linked to their internal setup and the features of the magnetic field between the rotor and the stator. Coupling the motor to the wheel while decoupling as much vibrations

from both sides as possible can be achieved using elastic couplings. These couplings are made from two stiff elements, connected to the two shafts on both sides, which are then linked by a rubber element acting as an isolator. In addition angular and parallel misalignments can be taken care of by the rubber element.

One further demand on the motor coupling is the possibility to axially displace the shaft due to the considerations in Section 4.1.1 "Kinematic Considerations". It is not recommended to move the motor with the shaft every time, since the readjustment to reach coaxiality between the motor and the shaft is both important and tedious. The axial displacement is furthermore designed such that it can not be changed during operation, allowing a stiffer and less complex connection. An option that is used in this design is the use of star disks, which transmit torque by using radial forces between a shaft and a hub. The selection of star disks for this application case is extended in Section 4.3.1 "Star Disks".

### **Active Control Considerations**

One application of the test rig is to research active control measures. To avoid squealing occurrences in the audible range, one discussed idea is the use of dithering. Dithering is originally a technique borrowed from the audio engineering. It relies on the fact that distorted sounds or signals can be improved by adding random noise so that the quantization effect inducing the distortion are overall less disturbing to the user. With the rig it could be investigated if the dithering noise can cancel the build-up of the squealing vibrations [31]. For that, a force needs to be introduced such that it can act with a high frequency on the contact point. Three solutions are laid out here.

A shaker, mounted to the side of the wheel could introduce lateral vibrations in the wheel. Such a shaker requires space between the side of the wheel and the bearings and support. Vertical vibration could be introduced inside the wheel by making radial cuts and inserting piezo-elements acting as shakers. A larger piezo-element could also be placed close to the force lever, for example between the lever stamp and the upper cage. The design of the lever is therefore chosen to be as simple and modular as possible, making it easy to replace and update parts.

### **Safety Concepts**

Due to heavy masses, loads and high rotations speeds, the safety of the operator and the equipment is to be considered at all times. And while some safety solutions can only be detailed during or after building the rig, some conceptual decisions can simplify that.

Firstly, the rig is to be constructed such that all rotating parts can be enclosed at least by a steel fence, if possible even by sheet metal. This is meant to stop anything from getting caught in the rotation. Furthermore, the operator can not thoughtlessly reach any rotating parts. It is intended to make the settings of the force, the angle and the lateral displacement available from outside the fence to limit the amount of times the fence needs to be removed to the minimum.

If equipment is to be changed inside the rig, the steel fence needs to be removed

temporarily, which brings the operator in potential danger. A lockable, electrical main switch could provide a higher safety. The idea is to secure the steel fence with a padlock, with only trained personnel having access to the key. When removing the padlock from the fence, it is placed in the main switch to the test rig, locking it to the switched off position. Another concept is having two padlocks, one securing the main switch and one securing the steel fence. The different keys correspond to different level operators, with the main switch key being the ‘user-level’ and the steel fence key being the ‘administrator-level’. An even higher level of safety can be reached if two locks secure the fence, and two trained staff members have the different keys. Operations in the rig are then only carried out with both people present and in mutual supervision.

The motor acts as the emergency brake. If there was an electrical blackout, all that can be done is letting the wheels coast down. The time to brake down the rig in dependency of the motor power is estimated in Section 4.3.4 "Motor". An emergency button needs to be implemented when the motor control is more detailed.

Securing the rig in space by either using external fixations or ground mounting the feet can avoid vibrations or the wheel inertia from critically moving the rig. Measurement and power cables are to be secured so that they can not get caught around a rotating part or moving element.

Another central concept is that the rig is to be run only by piloting it from another room. This would make sure that the operator can not be reached by any parts that, despite the efforts mentioned above, reach moving parts and are flung through the air.

## Construction Design

The construction design is the preparation for the dimensioning of the geometry. This includes the introduction of different load cases and corresponding applied loads. Key dimensions are the diameters of both shafts, which are the basis for the bearing selection process and the dimensioning of the wheel hubs.

### Considerations regarding contact forces

The dimensioning of the geometry can be based on the contact forces. These are estimated based on the normal force and the friction coefficient. In Section 3.2.1 "Parameter description" the maximal normal contact force is set to  $F_N = 35\text{kN}$ . The static friction coefficient used here is  $\mu = 0.65$ . With the relation between normal force and lateral force  $F_L$  the maximum lateral force is found to be  $F_L^* = \mu F_N = 22750\text{N}$ . In all following calculations, an uncertainty with respect to the setting of the normal force by 10% is considered. Considering this, the maximum normal and the lateral force are  $F_N = 38500\text{N}$  and  $F_L = 25025\text{N}$ .

Figure 4.2 shows a top view on the contact point and the forces acting on it in their respective coordinate systems. The  $x$  and  $x'$  axes represent the axial directions of the wheels. The angular misalignment is described by the angle  $\alpha$ . Assuming the lower wheel is driven, it acts on the contact point normal to its axial direction. This is depicted by the force  $F_L$  in the graphic. In the upper wheel, this force leads

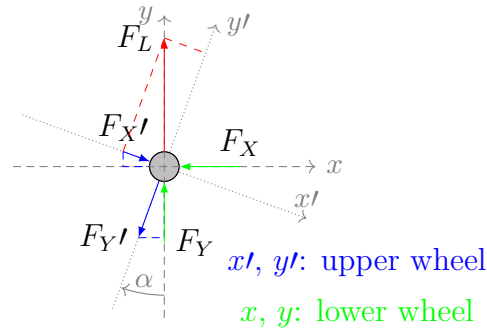


**Figure 4.2:** Lateral forces acting in the contact point represented by the central circle. The coordinate system fixed to the upper wheel  $x'$ ,  $y'$  is rotated towards the lower wheel coordinate system  $x$ ,  $y$  by  $\alpha$ . The length of the arrows is chosen arbitrarily.

to the reaction forces  $F'_X$  and  $F'_Y$ . The force  $F'_X$  represents the proportion with which the upper wheel is pushed sideways, and it needs to be supported by the bearings axially. The component of the contact force that is oriented in  $y'$  direction contributes to the acceleration and deceleration of the upper wheel. As long as there is no external braking torque on the upper wheel, a stationary rotation of both wheels will lead to the vanishing of the force  $F'_Y$ . The side force  $F'_X$  is countered by the forces  $F_X$  and  $F_Y$  on the lower wheel. The static equilibrium equations lead to the following relations for the forces.

$$F'_X = F_L \sin \alpha \quad (4.1)$$

$$F'_Y = 0 \text{ or } F_L \cos \alpha \quad (4.2)$$

$$F_X = F'_X \cos \alpha - F'_Y \sin \alpha \quad (4.3)$$

$$F_Y = F'_Y \cos \alpha + F'_X \sin \alpha \quad (4.4)$$

For the determination of the forces the dynamic behavior during squealing is observed by taking information gained from the parameter study. There, in extreme cases side forces of up to 10 times higher than the static side force are observed. The side force  $F'_X$  is therefore multiplied with this factor to take the squealing into account. For the longitudinal force variation a factor of 5 is assumed, although, since the simulations did not include any longitudinal slip calculation, this can not be based on the parameter study. However, as long as there is no controlled braking of the upper wheel, longitudinal forces are either comparatively small or very large, and therefore the exact figure for this factor is considered not essential. It should be noted that the simulation assumes a perfectly stiff mounting of the wheels at zero play, while in reality a lower stiffness of the suspension leads to lower forces for the same lateral displacement.

Equation 4.2 contains two possible forces, since different load cases need to be considered. The differentiation of the load cases is necessary since not all parts are designed to endure all possible loads, as will be described below. A total of three load cases are treated. The first load case (LC1) is the stationary rolling of both wheels.  $F'_Y$  vanishes as soon as stationarity is reached. The second and third load case describe misuse situations, in which the  $F_Y$  and  $F'_Y$  are substantially larger,

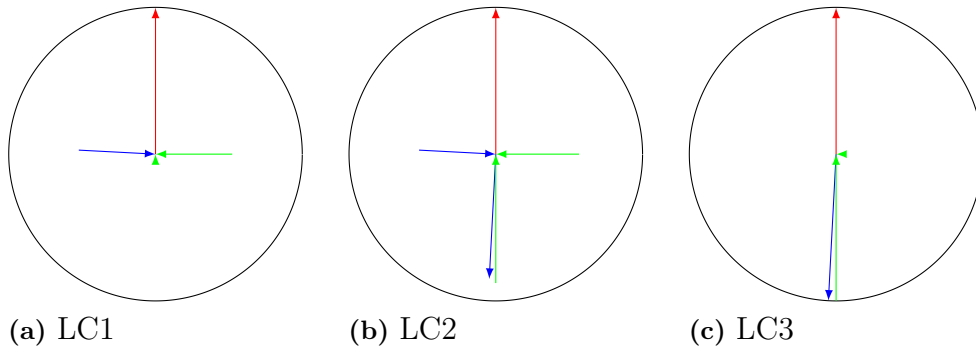


**Figure 4.3:** Limit circle with forces acting in the different load cases. The color and alignment of the forces is the same as in Figure 4.2.

which could correspond to one of the wheels being blocked. In this case, if the side force factor 10 is applied, the total lateral force exceeds  $F_L$ . Since this is physically not possible, but the actual behavior is unclear, two extreme cases are considered. Load case two (LC2) assumes that for the blocked wheel, squealing still occurs. The maximum side force is therefore the same as in LC1. The unused side force potential is then fully taken up by the longitudinal force. In the third load case (LC3) it is assumed that by blocking one wheel the complete force will act in longitudinal direction.

The angle  $\alpha$  is assumed to be maximum  $1.25^\circ$  in either direction. This corresponds to the objective lateral creepage 2.2% since  $\tan(1.25 * \pi/180) = 0.022$ . However, as a precaution measure, in the misuse cases LC2 and LC3 an angle of  $3^\circ$  is used for the calculation. Figure 4.3 shows the dimension of the force relative to the limit circle with radius  $F_N$ .

## Shaft Pre-calculation

To get a first estimation of the necessary shaft diameters, the following pre-calculation is done. Figure 4.4 shows the principal setup of wheel, attached to the shaft which is suspended between two bearings at the positions  $A$  and  $B$ . Both bearings are assumed to be able to take radial loads, while only bearing  $B$  takes the axial loads. The force input into the wheel is represented by the axial force  $F_a$ , the radial force  $F_r$  and the tangential force  $F_t$ . The distance between the force input and the bearings are described by  $a$  and  $b$ , and the diameter of the wheel is  $d$ . The first step is to determine the reaction forces at the bearing positions. Using the moment equilibrium at the bearing position  $B$ , the reaction forces at position  $A$  can be found as follows:

$$F_{A,X} = \frac{F_t b}{a + b} \quad (4.5)$$

$$F_{A,Y} = \frac{2F_r b - F_a d}{2(a + b)} \quad (4.6)$$

The total radial force on the bearing is calculated by vectorial addition

$$F_{A,tot} = \sqrt{F_{A,X}^2 + F_{A,Y}^2} \quad (4.7)$$

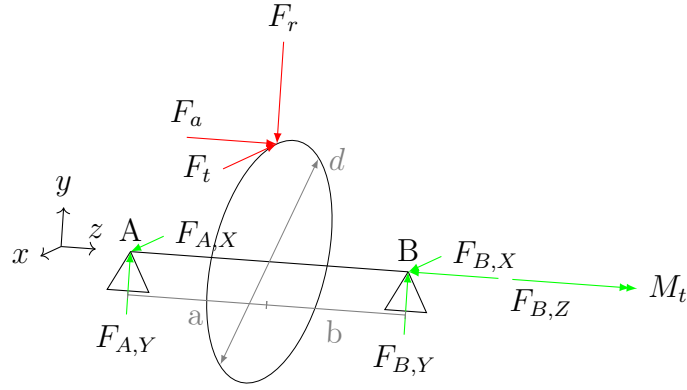


**Figure 4.4:** Coordinate system definition for shaft strength calculation.

The moment equilibrium around the bearing position  $A$  and the force equilibrium in  $z$  direction leads to the reaction forces at the bearing position  $B$ .

$$F_{B,X} = \frac{F_t a}{a + b} \quad (4.8)$$

$$F_{B,Y} = \frac{2F_r b + F_a d}{2(a + b)} \quad (4.9)$$

$$F_{B,Z} = F_a \quad (4.10)$$

And the total radial force is described by

$$F_{B,tot} = \sqrt{F_{B,X}^2 + F_{B,Y}^2} \quad (4.11)$$

The next step is to determine the highest acting bending moment. Due to the non-steady bending moment distribution along the shaft diameter because of the axial force input, the two sides of the shaft are considered separately, and then the side with the maximum moment is chosen for further consideration.

$$M_{B,X,left} = F_{B,Y} a \quad (4.12)$$

$$M_{B,Y,left} = -F_{A,X} a \quad (4.13)$$

$$M_{B,X,right} = F_{B,Y} b \quad (4.14)$$

$$M_{B,Y,right} = -F_{A,X} b \quad (4.15)$$

A resulting moment is calculated by vectorial addition.

$$M_{max,res} = \sqrt{M_{B,X,max}^2 + M_{B,Y,max}^2} \quad (4.16)$$

The necessary shaft diameter can now be estimated using the formula

$$d \leq \sqrt[3]{\frac{32M_b}{\pi\sigma_{b,allowed}}} \quad (4.17)$$

where  $\sigma_{b,allowed}$  is the allowed maximum stress, which is depending on the material, the load scenario and the geometry, and  $M_b$  is the maximum moment. Since bending

**Table 4.1:** Basic design diameters for upper and lower shaft depending on the load case.

Case	Unit	Use - LC1	Misuse - LC2	Misuse - LC3
Upper Shaft	mm	73	83	80
Lower Shaft	mm	95	103	101

moments as well as torsional moments are active, the von Mises yield criterion can be applied. The von Mises stress is calculated according to

$$\sigma_v = \sqrt{\sigma_{res}^2 + 3(\alpha_0 \tau_{res})^2} \quad (4.18)$$

where  $\alpha_0$  is a single number that can be taken from a table, allowing the rating of shear stresses as normal stresses. For the moments this leads to the composed moment  $M_v$ .

$$M_v = \sqrt{M_{b,max,res}^2 + \frac{3}{4}(\alpha_0 M_t)^2} \quad (4.19)$$

The factor  $\alpha_0$  is found to be 0.7 for alternating bending and normal steel types. The minimum diameter therefore needs to be

$$d \geq \sqrt[3]{\frac{32}{\pi \sigma_{allowed}} \sqrt{M_{b,max,res}^2 + \frac{3}{4}(\alpha_0 M_t)^2}} \quad (4.20)$$

with  $M_t$  being the torsional moment due to the tangential force  $F_t$ . The allowed maximum stress is found using the formula

$$\sigma_{allowed} = \frac{R_e}{SC_u \alpha_k} \quad (4.21)$$

with  $R_e$  being the elastic deformation limit of the material, the safety factor  $S$ ,  $C_u$  a usage factor that compensates for non-uniform motion, and  $\alpha_k$  taking notches into account. A safety factor of  $S = 4$ ,  $C_u = 1$  and  $\alpha_k = 1$  are used.

Using the input forces introduced in Section 4.2.1 "Considerations regarding contact forces" and the geometries described below, the required diameters for each shaft can be calculated, depending on the load case.

## Selection of purchased parts

### Star Disks

The connection between the motor and the lower shaft needs to provide a high enough transmissible torque while at the same time being able to change the axial position of the lower shaft. As outlined earlier, this is suggested to be done using Star Disks. Star disks are conical parts that are clamped between a hub and a shaft and which are axially pretensioned under operation. They operate by creating a radial force between the hub and the shaft. The emerging surface pressure allows a

torque transfer between the shaft and the hub. By stacking several Star Disks, the total transmissible torque can be increased. With this setup, the axial displacement of the lower shaft can be carried out as long as there is no pretension on the Star Disks. A data sheet provided by the manufacturer [32] is provided in the Appendix B.2 "Star Disks Data Sheets".

As described in the data sheet, the maximum transmissible torque  $M$  is dependent on the number of used disks  $n$ :

$$M_n = nM \quad (4.22)$$

The preload  $E$  is likewise proportional to the number of disks used

$$E_n = nE \quad (4.23)$$

Star Disks of the type "A090065IV" with an inner diameter of 65 mm and an outer diameter of 90 mm provide 131 Nm of transmissible torque when preloaded with 6700 N. With an assembly of 5 disks, a total transmissible moment of  $M_n = 655\text{Nm}$  can be transmitted when preloading the stack with 33.5 kN. For the purpose of this rig it is assumed that approximately 600 Nm is an appropriate driving torque, since as will be shown later in Section 4.3.4 "Motor", the main torque demand stems from the acceleration and deceleration of the rig and not from the sustaining of the speed during operation.

## Bearings

As introduced in Section 4.2.2 "Shaft Pre-calculation", each shaft is held in position by two bearings. The outcome of that section is an estimation for the shaft diameter at the bearing position, which is used one criterion in the bearing selection. Since bearings come in standardized sizes, the inner diameter for the upper bearings is chosen to be 85 mm and for the lower bearings it is 100 mm.

The requirements for the bearings are considered for choosing the bearing type. Under operation, the bearings will be exposed to high forces in radial direction due to the normal load, and relatively lower axial forces due to the relatively small angle that is introduced (see Equation 4.1). The maximum rolling speed should exceed 500 rpm for the lower bearings and 700 rpm for the upper bearings in order to realize the 50 km/h running speed.

To effectively measure and work with the squealing phenomenon, it is desirable to achieve a stiff mount of the shafts to minimize its influence. Furthermore, the harmonic vibration that is introduced into rotating systems by every bearing should be reduced as much as possible. Hence, bearings with a low clearance and the potential of an axial pretension are preferred. For the construction and running of the rig, low costs in acquisition and a low maintenance are desired.

Deep groove single-row roller bearings are chosen due to their ability to carry both axial and radial loads in a fairly compact setup. By constructing the outer rig as described in Section 4.1.2 "Outer Construction", the potential angular misalignment between the bearings is reduced and with that, the need for appropriate bearings such as spherical roller bearings. Angular roller bearings would be able to carry even higher axial pretension forces. However, since the stationary axial forces are so low, the deep groove roller bearings accomplish this task sufficiently. Finally, deep

groove roller bearings are the most common bearings and therefore beneficial in cost and support, and they are available as sealed versions which simplify the lubrication. Identical bearings are used on both sides so that the vibrations introduced by them at least have the same frequencies, simplifying the analysis of measured signals. The bearings with the serial numbers 6017-2RS1 and 6020-2RS1 are chosen for the upper and lower shaft respectively. The data sheets are given in Appendix B.1 "Bearing Data Sheets".

## Disk Springs

Disk springs are used to create an axial pretension  $F_{preload}$  in the bearings. This provides a stiff suspension by minimizing the bearing clearance. Deep groove roller bearings with an inner diameter of 80 mm have a inner clearance of  $12 \mu\text{m}$  to  $36 \mu\text{m}$ . With a contact patch of approximately 1.2 mm diameter this could be notable and important because the influence of the bearing clearance not easily predictable.

The disk springs are set to  $F_{preload} = 5000\text{N}$  by adjusting the number and thickness of shims that determine the axial spacing between the spring and the bearing housing lid. It is intended to use these springs on both shafts. By pretensioning only one side of the shaft, the axial position can be set relative to one housing by inserting shims. The spring can then act against this fixed side.

These springs are described in DIN 2093 and characterized by the deflection  $s$ , up to which the spring behaves approximately linear, and the force necessary to reach this deflection  $F_s$ . Using the relation for the spring stiffness  $k = F_s/s$ , the necessary deflection  $s_i$  to achieve the force  $F_{preload}$  is found by  $s_i = s \cdot F_{preload}/F_s$ .

For the upper shaft, one spring with the outside diameter of 125 mm is used. With  $s = 2.63\text{mm}$  and  $F_s = 29,900\text{N}$  the necessary deflection  $s_i$  is found to be 0.44 mm. The spring used is named DIN 2093 - B 125. On the lower shaft the spring DIN 2093 - B 160 is used, with an outside diameter of 160 mm,  $s = 3.38\text{mm}$ ,  $F_s = 41000\text{N}$  and  $s_i = 0.41\text{mm}$ .

To change the spring stiffness, several springs can be combined. This is used in the generation of the  $F_N = 35000\text{N}$  normal force. Here, it is desirable to design the spring stiffness low enough so the normal force can be set accurately. At the same time, the spring stiffness needs to be as high as possible to reduce the influence of the suspension on the contact. To design the spring stiffness, it is assumed that the normal force is introduced by a M16 screw. The choice of screw leads to the choice of disk spring, DIN 2093 - A 40 with an inner diameter of 20.5 mm. It is assumed that when adjusting the normal force, a quarter rotation of the screw is a differentiable setting. Furthermore, 36 different settings are desirable, to realize a step size of 1 kN, leading to in total 9 rotations. The pitch of metric screws describes the axial distance from one crest to the next, therefore in this case giving the compression of the springs per each rotation. A fine thread with a pitch of 0.5 mm is picked because it provides more rotations per change in length. A total deflection of 9 rotations  $\cdot$  0.5mm/rotation = 4.5mm at maximum force is hence desired.

With a lever ratio of 2, which originates in the way the force lever is set up (see Section 4.4 "Rig Mock-up"), the maximum force at the springs is  $F_{N,2} = F_N/2 = 17500\text{N}$ . The total spring stiffness  $k_{tot}$  needs to be around 3888 N/mm. Using two

springs in parallel doubles their total stiffness, using them in series halves their total stiffness. The spring DIN 2093 - A 40 provides a maximum deflection  $s = 0.68\text{mm}$  at  $F_s = 6500\text{N}$ . With three of these springs in parallel the maximum force of  $F_{s,3} = 3 \cdot F_s = 20400\text{N} > F_{N,2}$  can be achieved. With 7 packages of 3 springs in parallel, a maximum deflection of  $s_{max} = 7 \cdot 0.68\text{mm} = 4.76\text{mm} \geq 4.5\text{mm}$  is realized, with a spring stiffness of  $k_{tot} = 4097\text{N/mm}$ .

## Motor

One motor is used to drive the rig. To realize a transmission that is as direct as possible, minimizing unnecessary rotational vibration sources, no gearbox or other torque converters are used. For practicality reasons, the motor is acting on the lower wheel.

The power requirements for the motor are derived from the necessary torque and rotational speed. Two cases are included in the power estimation. Firstly, the motor needs to produce enough torque to maintain the squeal motion. This torque is described by  $T_{min,squeal} = F_X r_{lw}$  with the longitudinal force  $F_X$  from Equation 4.3 and the radius of the lower wheel  $r_{lw}$ . With  $F_X = 119\text{N}$  and  $r_{lw} = 261\text{mm}$  the torque necessary to maintain potential squealing is  $T_{min,squeal} = 31\text{Nm}$ .

Secondly, the power reserve needs to be large enough to accelerate and decelerate both wheels in a reasonably short time, since the motor also acts as the break. To estimate a relation between motor power and breaking time, the energy contained in the rotation of the two wheels at the driving speed of  $V_{kmh} = 50\text{km/h}$  is calculated. The energy  $E$  in a rotating body is calculated according to

$$E = \frac{1}{2} J \omega^2 \quad (4.24)$$

with the moment of inertia  $J$  and the angular velocity  $\omega$ . The angular velocity is found by

$$\omega = 2\pi n = 2\pi \frac{V_{kmh}}{3.6} \frac{1}{2\pi r} = \frac{V_{ms}}{r} \quad (4.25)$$

with the number of revolutions  $n$ , the speed in m/s  $V_{ms}$ . The moment of inertia can be estimated by

$$J = \int_M r^2 dm \quad (4.26)$$

weighting each mass element  $dm$  with its squared distance from the rotation axis  $r^2$ , integrating over a mass  $M$ . For rotation symmetric bodies this simplifies to

$$J = \frac{1}{2} R^2 m \quad (4.27)$$

with the outer radius  $R$ . The mass  $m$  of a homogeneous full cylinder is described by  $m = \rho V = \rho \pi R^2 l$  with the density  $\rho$  and the length  $l$ . The total moment of inertia for the shaft-wheel combination is the sum of the individual moment of inertias for each part,

$$J = J_s + J_w = \frac{1}{2} (R_s^2 m_w + R_w^2 m_s) = \frac{\pi \rho}{2} (R_s^4 l_s + R_w^4 l_w) \quad (4.28)$$

**Table 4.2:** Rotational speed, moments of inertia and energy stored at maximum speed for the upper and the lower wheel-shaft combination. The calculation is assuming steel with a density of  $\rho = 7850\text{kg/m}^3$ .

Input	Unit	Upper Wheel/Shaft	Lower Wheel/Shaft
$\omega$	rad/s	73	53
$R_w$	m	0.19	0.26
$l_w$	m	0.08	0.15
$R_s$	m	0.1	0.13
$l_s$	m	0.17	0.6
$J$	kgm <sup>2</sup>	1.5	10.5
$E$	kJ	4	14.7

Since the wheel itself is not a full cylinder but instead the hole is filled with shaft material, in the calculations the shaft is shortened by the length which is already included in the wheel. As seen in Table 4.2, the total kinetic energy stored in the rig at 50 km/h is estimated to be 18.7 kJ. From this, the braking time  $t$  can be estimated by inserting the available average mechanical power during braking and acceleration by  $t = E_{tot}/P_{mech}$ .

However, the mechanical power of an electrical motor is represented by  $P_{mech} = T\omega$  and since the above-noted approach assumes that the maximum power is constantly available, this leads to disproportionately high torques at low speeds. To quantify this influence, a time-stepping simulation of a startup has been done, assuming the parameters noted above. Two motors are considered, with rated powers of 7.5 kW and 15 kW. For both, an efficiency of 0.85 is assumed. The time-stepping simulation allows the limitation of the maximum torque to  $T_{max} = 500\text{Nm}$ . Once the desired rotation speed is reached, the power input is stopped. For each time step, the momentary available torque  $T_*$  is calculated and used in the formula

$$T = J \frac{\partial \omega}{\partial t} \Rightarrow \frac{\partial \omega}{\partial t} = \frac{T_*}{J} \quad (4.29)$$

and after discretization and integration one obtains

$$d\omega = \frac{T_*}{J} dt \quad (4.30)$$

Concluding the motor requirements regarding the power, it can be stated that the desired accelerating/braking time is the critical factor. Motors that are able to accelerate the rig in a reasonable amount of time, for example 5 seconds, can also maintain the squealing. Since no emergency brake is planned, the motor acts as the only brake and therefore the braking time can be the deciding factor.

Further requirements include a low vibration introduction into the system. This can be achieved with special filter circuits in the control electronics, which are not further described here. Another way is the decoupling of the motor using a component as described in Section 4.1.7 "Motor Coupling".

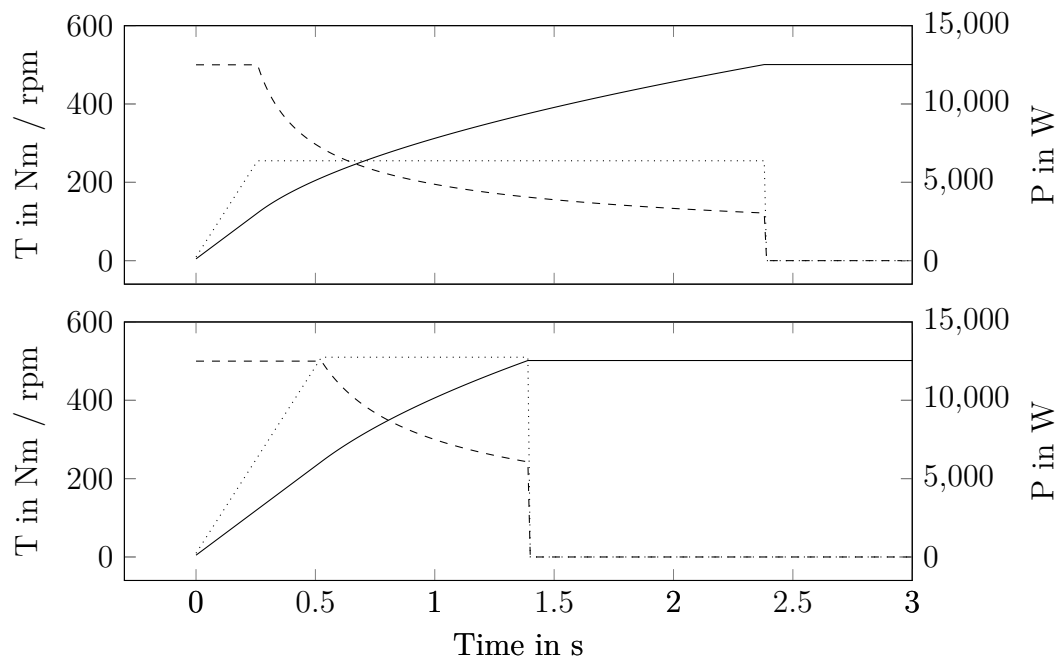


**Figure 4.5:** Simulation of the startup for different motors. The rotation speed (—) in dependency of the momentary torque (- - -). The used power (.....) is plotted as the result of these two. In the top, the graph for a motor with the rated power of 7.5 kW and in the bottom, the startup of a motor with the rated power of 15 kW is shown. The desired rotation speed is reached after 2.38 s and 1.39 s respectively.

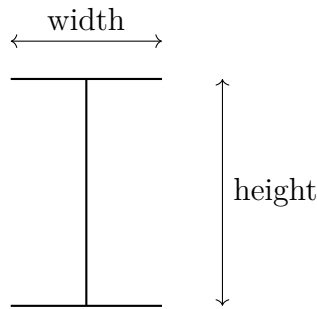


**Figure 4.6:** A principal sketch of I profiles.

## I-Profiles

The selection of the I profile for the setup of the outer frame of the rig is done based on beam bending theory in combination with the norm DIN EN 10024: 1995. The norm describes the standard sizes and geometries of I profiles. For these geometries the second moments of inertia  $I$  can be found. The maximum, static deflection of a beam loaded with a point force is described by the equation

$$f_{point} = \frac{F_n a^2 b^2}{3EI} \quad (4.31)$$

with  $f_{point}$  the deflection at the input point,  $a$  and  $b$  the distances from this point to the fixed ends of the beam, the Young's modulus  $E$  and the total length  $l = a + b$ . From the calculations in Section 4.2 "Construction Design" the maximum normal force on one bearing is found and used as the input for the point force  $F_n$  in these calculations. However, since the force is acting on the bearing housing, and the bearing housing itself is not acting on the beam directly but on a 20 mm thick sheet metal plate, the point force assumption is not sufficient as a model. The equation

$$f_{distributed} = \frac{5F_n l^3}{384EI} \quad (4.32)$$

gives the maximum deflection of a beam fixed on the sides for an evenly distributed load. This, on its own, is likewise not a suitable model, but the real behavior will be in between these two extreme cases.

Profiles are characterized by their height as seen in Figure 4.6, and heights between 80 mm and 180 mm are discussed. Assuming a normal load  $F_n$  of approximately 21 kN and a beam length  $l$  of 600 mm, the deflections shown in Figure 4.7 are calculated. The figure shows that while for the more compact I profiles a change has a large effect, the thicker profiles all show relatively low deflections in reaction to this force. Substantially reducing the deflections above the profile height of 140 mm becomes a very material intensive and can hardly be justified when considering the clearances and stiffnesses in the rest of the rig. Using profiles with a height of 140 mm is therefore recommended.

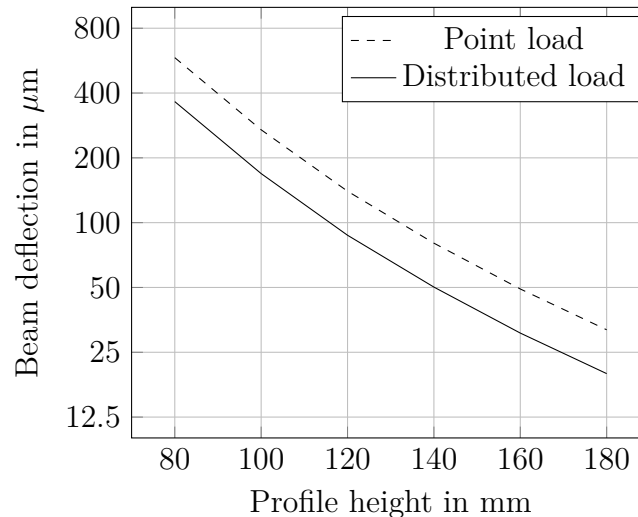


**Figure 4.7:** Effect of an increased I profile height on the beam deflection, shown for the assumption of a distributed load and a point load.

## Rig Mock-up

In the following, the rig mock-up is presented in sub-assemblies. First, a cross section of the upper shaft assembly is shown in Figure 4.8. The wheel is pressed on the shaft as seen in the center of the picture. On the left and right end of the shaft the bearing seats are visible. Side forces that are introduced into the bearings are countered by the distance rings that are pressed against the outside of the outer bearing ring. The axial force is introduced on one side by a disk spring, and on the other side the correct axial spacing is adjusted with an appropriate number of spacer rings. The outer parts are the bearing housings, that take all forces on the bearings and provide room for the disk springs and spacers. The shaft has a central hole on the left side that is connected to a radial bore hole. This is meant for the connection of measurement equipment in combination with a slip ring. On the other side, the shaft is extended to provide an option of attaching measurement equipment or even a second motor.

The next Figure 4.9 shows how the rotating and the lifting motion of the upper wheel are integrated. The upper wheel assembly, shown on the left, is mounted in an assembly called the ‘lantern’. The lantern side walls provide a socket for the bearing housings of the upper shaft assembly. The rotation around the vertical axis is introduced by mounting the side plates into two disks, that can be rotated in two plates with according round holes. This way the necessary lifting motion is provided. The contact force can be introduced by pressing on the top disk.

The two plates guiding the lantern are named top plate and bottom plate and they are part of the upper cage. The spacing of these plates is done by the upper cage side plates. A rod that is connected to both the upper top plate on the cage and the upper disk on the lantern with ball joints is used to set the angle. By inserting spacers of different thicknesses the length can be adjusted and repeatably set to the same lengths. This rod construction can be seen in Figure 4.10. The upper and

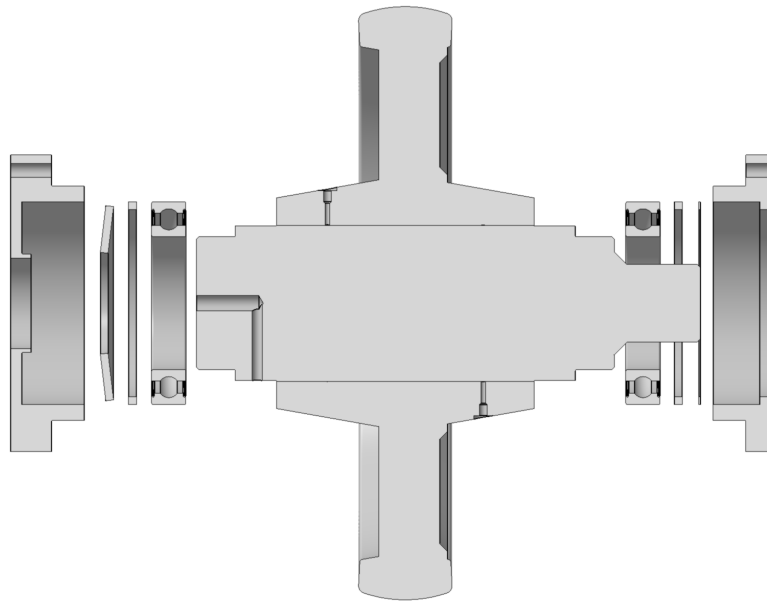


**Figure 4.8:** Upper shaft assembly.

lower plate are fixed to the frame.

The lower wheel is mounted in the lower shaft assembly shown in Figure 4.11. This shaft needs to provide the possibility of axially displacing the wheel by approximately 40 mm. This is implemented by using sleeves that hold the bearing and can move axially in the bearing housing. The sleeves are displayed on the shaft between the wheel and the bearings. The bearing is pressed on the shaft and on the outside held by the sleeves, axially secured with locking rings. The sleeves therefore move axially with the shaft but can rotate around it. They are radially held by the bearing housing and secured against rotating in it by a feather key. The axial displacement can be accurately set by spacer rings on both sides. On one side, a disk spring is inserted to provide the axial pre-loading. Bearing housing lids close the bearing housings and counter the axial force. To simplify the axial displacement, lubricant can be pumped between the bearing housings and the sleeves, with guiding cutouts around the sleeve. On the right, the connection to the motor can be seen.

The lower shaft assembly is mounted in the lower shaft cage assembly as shown in Figure 4.12. A simple assembly of two side plates on a base plate provides a hold for the lower bearing housings. To stabilize the side plates, support walls are used welded to it and connected to the bottom plate as well. The bottom plate is fixed in the rig frame.

The rig frame is built up of I-profiles, since these provide flexibility for future use, the necessary stability and come as standard parts. The upper and lower cage assembly are inserted into the rig frame as shown in Figure 4.13.

The force is introduced by the force lever displayed in Figure 4.14. The horizontal plates on the left and right are connected to the frame. The force is generated using disk springs as displayed on the left side. When inserting and tightening a screw in the round counter-piece that is connected to the frame, the springs are compressed and act on the lever. The hinges, realized with 35 mm bolts, generate the necessary

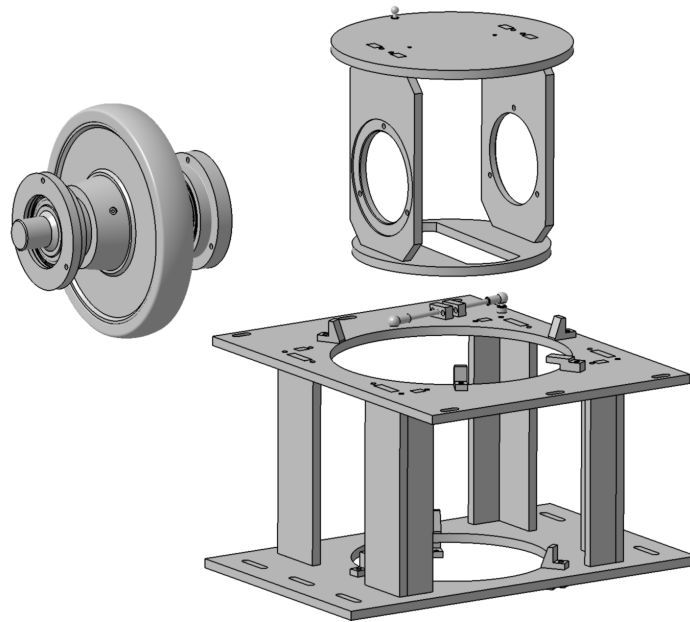


**Figure 4.9:** Upper shaft cage assembly.

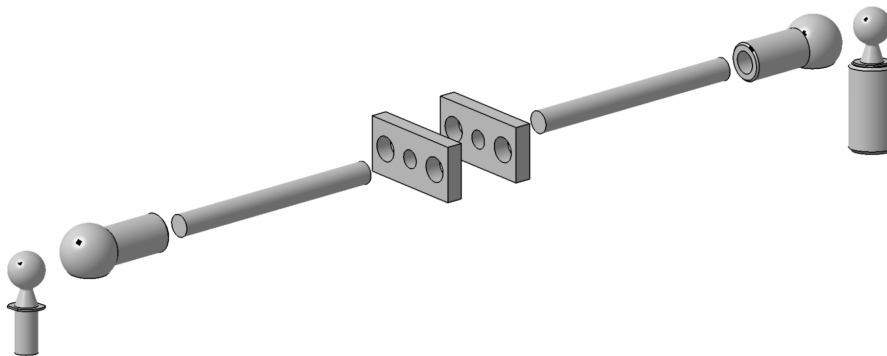


**Figure 4.10:** Rod and spacers angle setting construction.

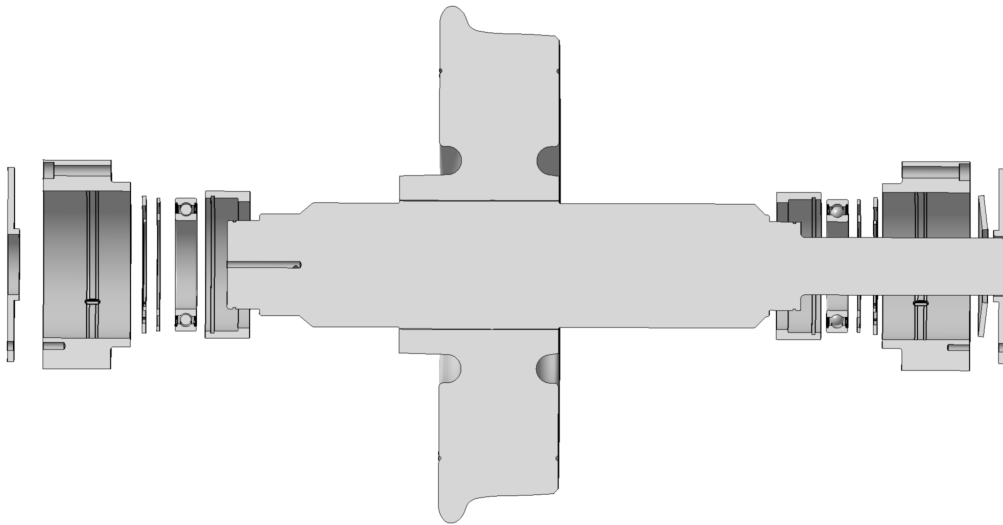


**Figure 4.11:** Lower shaft assembly.

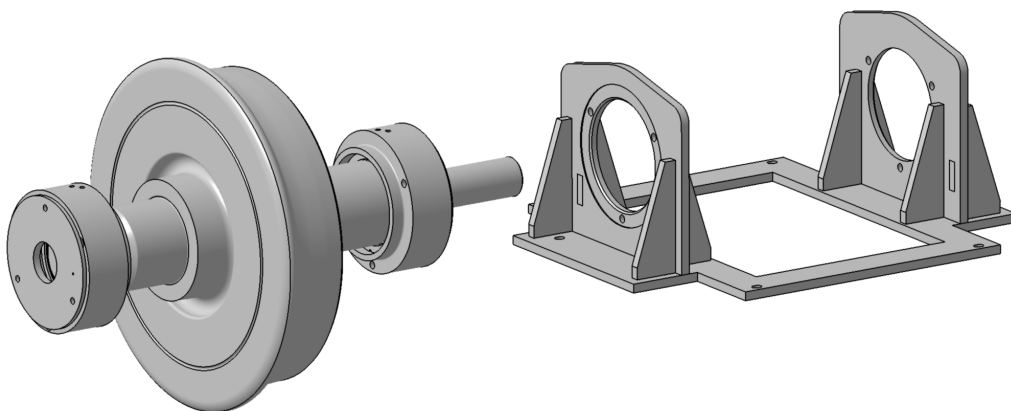


**Figure 4.12:** Lower shaft cage assembly.

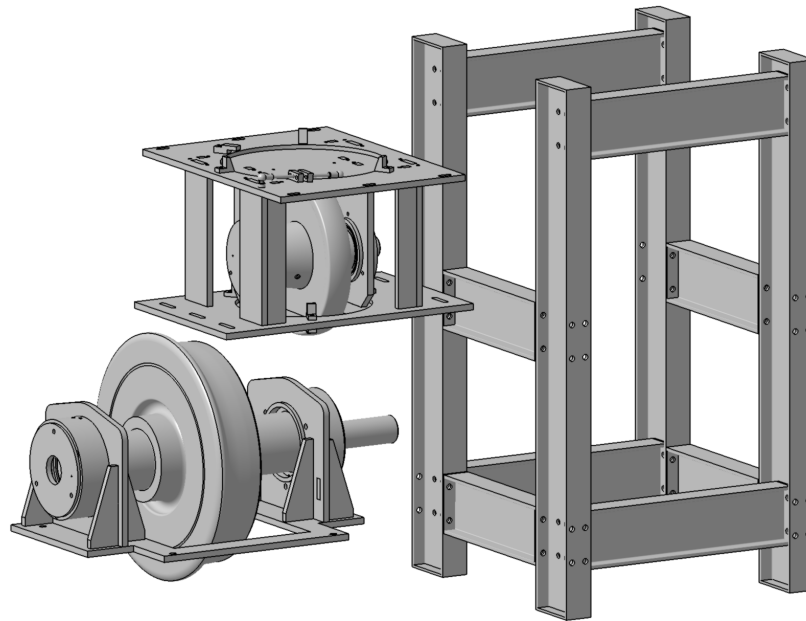


**Figure 4.13:** Core rig assembly.

vertical motion at the central part which is called the stamp. The stamp hinge is located exactly in the middle of the force lever, leading to a lever ratio of 1:2. With this, only half the force needs to be generated at the disk springs.

The driving assembly shown in Figure 4.15 is the connection between the motor and the shaft. Here, the axial displacement of the lower shaft is compensated, since the motor is not meant to follow this displacement every time. Star disks are used to realize this.

The complete setup can be seen in Figure 4.16.

## Stability calculations

### Analytic safety calculation for critical parts

#### Shafts

The shaft safety calculation strictly follows [33, Section 6.9.5], a detailed calculation is therefore not given here. However, all inputs to the calculation are given in Tables 4.3 and 4.4. The graphs in the top rows of the tables represent the bending moment distribution  $M_x$  and  $M_y$  across the length  $l$  of the shaft.  $M_x$  describes the moment emerging from the bearing reaction forces in x-direction, as shown in Figure 4.2.  $M_y$  is analogously the moment due to the forces  $F_{A,y}$  and  $F_{B,y}$ .  $M_t$  describes the torsional moment.

For each load case, the stability is evaluated at two positions  $P_{crit}$ , at the contact position in the middle of the shaft and at the bearing position of the bearing with the higher load. These positions are indicated with dashed lines in the graphs. The shaft diameter  $d$  at the calculation position is the basis for the geometrical input data like cross section and section modulus.

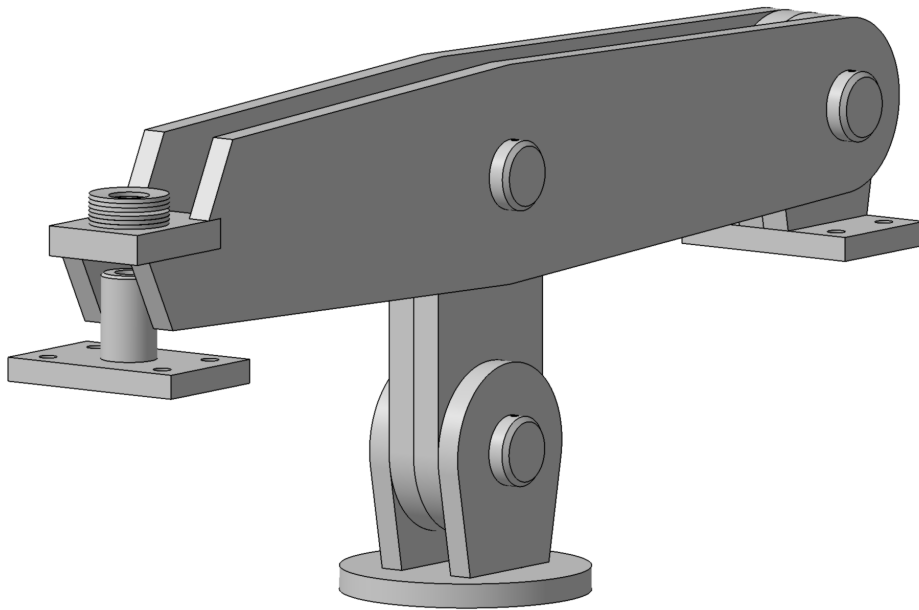


**Figure 4.14:** Force lever assembly.

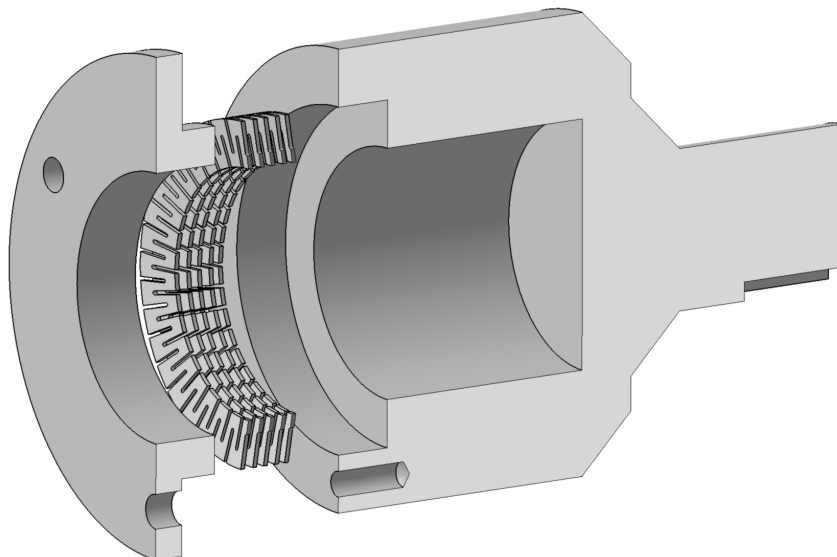


**Figure 4.15:** Driving assembly.

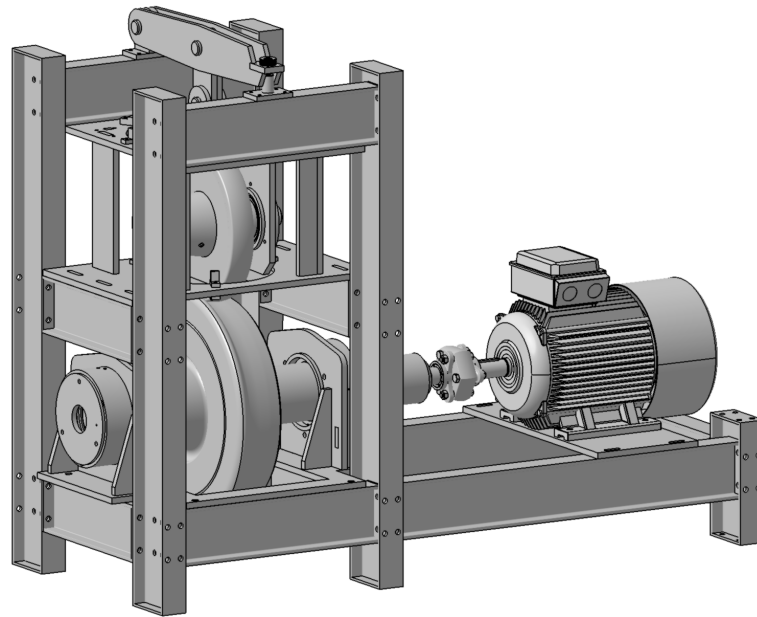


**Figure 4.16:** Complete rig.

In the static strength calculation the goal is to avoid plastic strains during overloads. This is taken care of by using the overload factor  $K_0$ . The yield strength of the shaft material under bending  $\sigma_y$  and torsion  $\tau_y$  is chosen for the material C45. For the static strength, a safety factor  $S_s$  larger than 1.3 to 2.0, depending on the importance of the structure and the certainty about the acting forces. The minimum safety factors of 1.9 on the upper shaft as well as 3.2 on the lower shaft, which are reached in the second load case, fulfill this criterion.

The fatigue calculation considers the material and geometrical characteristics of the shaft more in depth. Since due to the rotation stress concentrations appear cyclic around the shaft, surface finishing and heat treatment become more important for the calculation. This is taken care of with the calculation coefficients  $K_*$ .

$K_{d\sigma}$  and  $K_{d\tau}$  are influence factors of the shaft diameter, chosen for carbon steel from [33, Table 6.47].  $K_{F\sigma}$  and  $K_{F\tau}$  are factors considering the finishing treatment, here assuming the finishing grinding with a roughness of  $R_z$  0.8 - 1.6  $\mu\text{m}$ , found in [33, Table 6.48].  $K_v$  corrects for surface hardening, which is not done here, and so it has the value 1.  $K_\sigma$  and  $K_\tau$  from [33, Table 6.50] are factors taking the geometry surrounding the critical position into account, since step junctions and small chamfers can lead to high stress concentrations. It is assumed that only the step that localizes the bearings axially has a radius small enough to be considered here, and all other diameter changes are designed with large radii.

The endurance limits of the smooth, ideal geometry  $\sigma_{-1}$  and  $\tau_{-1}$  are given in [33, Table 6.45] and are chosen for the material C45. Not all materials react in the same way to stress cycle imbalance, and therefore the factor  $\Psi_\tau$  from the same table compensates for that.

With these specifications the safety factor  $S_f$  is calculated. The value for the fatigue strength safety factor should be larger than 1.5 to 2.5. Similar to the static calculation, for both shafts the second load case is critical at the input position. The

safety values of 2.1 and 1.7 for the upper and lower shaft respectively are within the acceptable range. However, it has to be noted that the load case 2 represents an unusual situation, in which the rig will not be used for extended amounts of time. The fatigue safety factor for this case is thus not very significant. The fatigue safety factors for the use case are acceptable.

Without going into detail in the calculation here, the effect of introducing a braking torque of  $T_{br} = 600\text{Nm}$  on the upper shaft into the LC1 calculation can be shown. This torque is chosen for feasibility reasons, since motors that could introduce  $T_{br}$  are likely rather large in size, especially when used without a gearbox. In this case, the static safety factor for the input position is about 2.0 for the upper and 2.5 for the lower shaft. The fatigue strength safety factor for the input position is 2.3 for the upper and 1.9 for the lower shaft and thus in an acceptable range.

## Bearings

The bearing life rating calculation is a tool to estimate the number of rotations, in which the bearing, with a probability of 90 %, does not fail. The calculation is described in [34], which links to the standard ISO 281:2007, and is executed using the equation

$$L_{10} = \left(\frac{C}{P}\right)^p \quad (4.33)$$

with the basic bearing life rating  $L_{10}$ , the basic dynamic load rating  $C$  which is given by the manufacturer, and the equivalent dynamic bearing load  $P$ . The exponent  $p$  is depending on the type of bearing, for ball bearings it is 3.

The dynamic bearing load  $P$  is a combined measure of the acting axial and radial forces and is calculated using [35]. The axial force  $F_a$  as well as the radial force  $F_r$  are weighted with the factors  $X$  and  $Y$  and added according to

$$P = XF_r + YF_a. \quad (4.34)$$

In [36] a table is given in which the coefficients  $X$  and  $Y$  are found, according to a factor  $f_0F_a/C_0$ . The calculation factor  $f_0$  is found in the data sheet of the bearing. In the case of slow or no rotation, the contact stress between single balls and the raceway can not exceed the yield strength of the materials. This is considered using the basic static load rating  $C_0$ , which is compared to the equivalent static bearing load  $P_0$ ,

$$P_0 = X_0F_r + Y_0F_a \quad (4.35)$$

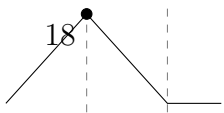
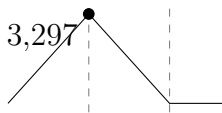
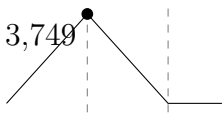
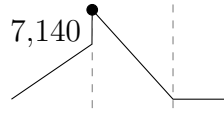
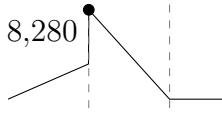
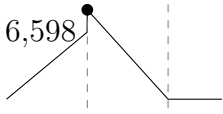
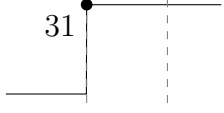
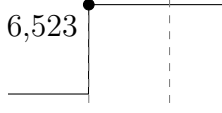
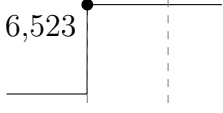
as described in [37]. The coefficients  $X_0$  and  $Y_0$  for deep groove ball bearings are 0.6 and 0.5 respectively. However, if the radial force  $F_r$  exceeds the calculated  $P_0$ ,  $F_r$  is used as the equivalent static bearing load. The static load safety factor can be determined using  $S_{b,s} = P_0/C_0$ .

The calculation input data and results can be found in Table 4.5. For both shafts and each load case, the bearing life and static bearing load are calculated. It should be noted that the bearing life estimation for the load cases LC2 and LC3 is not very meaningful since those load cases do not represent permanent operating conditions. To illustrate the life expectancy result, it is also given in traveled distance, and due to the different sized diameters of the wheels the same distance of 57 000 km is

**Table 4.3:** Calculation inputs and results from the shaft safety calculations for the upper shaft. The plots show the moments along the shaft, with the maximum value given.

Input	Unit	LC1		LC2		LC3	
$M_x$	Nm						
$M_y$	Nm						
$M_t$	Nm						
Geometry							
$l$	mm	240	240	240	240	240	240
$P_{crit}$	mm	120	240	120	240	120	240
$d$	mm	100	85	100	85	100	85
Static strength calculation							
$K_0$	—	3	3	3	3	3	3
$\sigma_y$	MPa	640	640	640	640	640	640
$\tau_y$	MPa	290	290	290	290	290	290
$S_s$	—	3.5	>10	1.9	2.8	2.2	2.8
Fatigue strength calculation							
$K_{d\sigma}$	—	0.71	0.71	0.71	0.71	0.71	0.71
$K_{d\tau}$	—	0.59	0.59	0.59	0.59	0.59	0.59
$K_{F\sigma}$	—	0.9	0.9	0.9	0.9	0.9	0.9
$K_{F\tau}$	—	0.95	0.95	0.95	0.95	0.95	0.95
$K_v$	—	1	1	1	1	1	1
$K_\sigma$	—	1.9	1.9	1.9	1.9	1.9	1.9
$K_\tau$	—	1.55	1.55	1.55	1.55	1.55	1.55
$\sigma_{-1}$	MPa	250	250	250	250	250	250
$\tau_{-1}$	MPa	150	150	150	150	150	150
$\Psi_\tau$	—	0.005	0.005	0.005	0.005	0.005	0.005
$S_f$	—	>10	>10	2.1	4.6	2.5	4.6

**Table 4.4:** Calculation inputs and results from the shaft safety calculations for the lower shaft. The plots show the moments along the shaft, with the maximum value given.

Input	Unit	LC1		LC2		LC3	
$M_x$	Nm						
$M_y$	Nm						
$M_t$	Nm						
Geometry							
$l$	mm	750	750	750	750	750	750
$P_{crit}$	mm	300	600	300	600	300	600
$d$	mm	145	100	145	100	145	100
Static strength calculation							
$K_0$	—	3	3	3	3	3	3
$\sigma_y$	MPa	280	280	280	280	280	280
$\tau_y$	MPa	150	150	150	150	150	150
$S_s$	—	3.4	>10	3.2	6.3	3.7	6.3
Fatigue strength calculation							
$K_{d\sigma}$	—	0.71	0.71	0.71	0.71	0.71	0.71
$K_{d\tau}$	—	0.59	0.59	0.59	0.59	0.59	0.59
$K_{F\sigma}$	—	0.9	0.9	0.9	0.9	0.9	0.9
$K_{F\tau}$	—	0.95	0.95	0.95	0.95	0.95	0.95
$K_v$	—	1	1	1	1	1	1
$K_\sigma$	—	1.9	1.9	1.9	1.9	1.9	1.9
$K_\tau$	—	1.55	1.55	1.55	1.55	1.55	1.55
$\sigma_{-1}$	MPa	250	250	250	250	250	250
$\tau_{-1}$	MPa	150	150	150	150	150	150
$\Psi_\tau$	—	0.005	0.005	0.005	0.005	0.005	0.005
$S_f$	—	2.3	>10	1.7	>10	2.0	>10

**Table 4.5:** Calculation Data for the Bearing Life Rating

Input	Unit	Upper Shaft			Lower Shaft		
Bearing Data							
Bearing Name		6017-2RS1			6020-2RS1		
$C$	kN	52			63.7		
$C_0$	kN	43			54		
$f_0$	–	15.8			15.9		
Forces							
Load Case		LC1	LC2	LC3	LC1	LC2	LC3
$F_r$	kN	11	12	20	15	15	21
$F_a$	kN	10	18	5.0	10	19	6.3
Bearing Life estimation							
$X$	–	0.56	0.56	0.56	0.56	0.56	0.56
$Y$	–	1.08	1.03	1.43	1.08	1.03	1.35
$P$	kN	17	25	18	20	28	20
$L_{10}$	$10 \times 10^6$ rot	48	15.9	42.7	35	11.3	32
Distance	1000 km	57	19	51	57	18	52
Static Bearing load							
$P_0$	kN	12	16	22	15	19	21
$S_{b,s}$	–	3.6	2.7	2.2	3.7	2.9	2.6

reached. However, it is expected that the actual distance traveled before bearing failure is considerably larger, since LC1 assumes full forces, including the extreme side forces due to squealing, permanently acting on the bearing. And while this state can be reached for some periods of time, the anticipated use includes driving the rig with lower normal forces and lateral creepages. One further aspect that can increase the bearing life substantially is to consider the direction of the axial force which is linked to the direction of the introduced angle, and to adapt the direction of the axial pretension opposite to that. Hence, the considered maximum axial load from LC1 is reduced by the pretension of 5 kN while maintaining the benefits of the pretension. The minimum static bearing load safety factor of 2.2 is reached in LC3 for the upper shaft.

## Bolts

The normal force is applied with the lever displayed in Figure 4.14. The stability of the bolt connecting the parts of the hinge can be evaluated by considering the shear forces and moments acting on it. A simplified setup is sketched in Figure 4.17.

The shear force  $F_{shear}$  is largest at the position “b”, where  $F/2$  is acting as shearing on the bolt cross section, and is zero at the central position “a”. However, here the bending moment on the bolt is largest. Assuming the thickness  $t$  for the material, the bending moment at the position “b” is  $M_{bend,b} = Ft/4$  and  $M_{bend,a} = 3Ft/8$ .

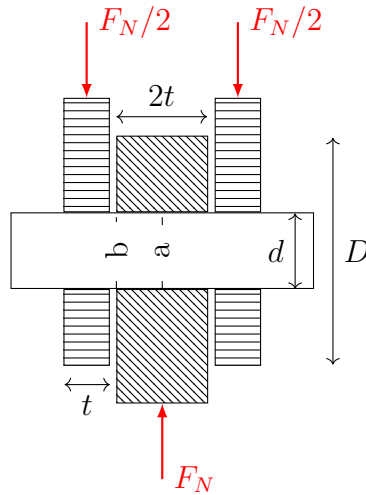


**Figure 4.17:** Principal Sketch of the Force Lever Bolt.

With these, the stresses  $\sigma$  in the cross sections are evaluated as follows:

$$\sigma_{bend,*} = M_{bend,*}/W_b \quad (4.36)$$

with the section modulus  $W_b = \pi d^3/32$  [38]. The shear stress  $\tau$  is found as

$$\tau = \frac{F/2}{A} \quad (4.37)$$

and with the section surface area  $A$ . In position b both the shearing stress and the bending stress act, and the von-mises criterion for equivalent tensile stress is used:

$$\sigma_{v,b} = \sqrt{\sigma_b^2 + 3\tau^2} \quad (4.38)$$

In position “a” only the bending moment is critical and the bending stress is used directly in the calculation of the safety factor,  $\sigma_{v,a} = \sigma_{bend,a}$ . The steel S275 is chosen as a reference for the stability since it is a common steel for general engineering purposes. Its minimum yield strength of 275 N/mm<sup>2</sup> is compared to the stresses  $\sigma_{v,*}$ . Table 4.6 shows the calculation details. As a last step, the pressure in the hole of the fork and the beam is calculated. For that, the projected contact areas  $A_{proj,fork} = td$  and  $A_{proj,beam} = 2td$  are compared to the applied force using

$$p_{beam} = \frac{F}{A_{proj,beam}} \quad (4.39)$$

$$p_{fork} = \frac{F/2}{A_{proj,fork}} \quad (4.40)$$

It becomes clear that the pressure in the fork and beam is the same, being  $38500\text{N}/840\text{mm}^2 = 46\text{N}/\text{mm}^2 < \sigma_{allowed}$ .

**Table 4.6:** Overview over the calculation data for the bolt safety calculation.

Input	Unit	Position "a"	Position "b"
Geometry			
$t$	mm	12	12
$d$	mm	35	35
$D$	mm	87.5	87.5
$W_b$	mm <sup>3</sup>	4209	4209
Forces			
$F$	kN	38.5	38.5
$F_{shear}$	kN	0	19.25
$M_{bend,*}$	Nm	462000	115500
Results			
$\sigma_{bend,*}$	N/mm <sup>2</sup>	110	27
$\tau$	N/mm <sup>2</sup>	0	20
$\sigma_{v,*}$	N/mm <sup>2</sup>	110	44
$\sigma_{allowed}$	N/mm <sup>2</sup>	275	275
$S$	—	2.5	6.2

### Press fits

Both wheels are connected to the shafts by press fits. This allows a good centering and coaxiality of wheel and shaft, minimizing imbalance excitation. The design of the press fits is done according to [33]. Since the comprehensive description of the general way to calculate this is given in the [33, Section 6.10.3], here only the input data and the results will be presented, together with a short overview over the data used. The input and output data can be found in Table 4.7.

The calculation is based on geometrical data like the contact diameter  $d$ , the hole diameter of a bore hole in the shaft  $d_1$ , the outer hub diameter  $d_2$ , and the contact length  $l$ . Further inputs are the material data Young's Modulus  $E$ , Poisson ratio  $\nu$  and the yield strengths of shaft  $\sigma_{Y,1}$  and hub  $\sigma_{Y,2}$ . The forces considered are derived from the contact forces described in Section 4.2.1 "Considerations regarding contact forces". Here, the axial force  $F_a$  is taken from load case 2 and the torque  $T$  is taken from load case 3.

The aim is to calculate the necessary tolerances for shaft and hub, with the basic idea that the contact pressure between shaft and hub in any case needs to be large enough to transmit the acting forces, while at the same time not exceeding the yield strengths of the materials. This is ensured with a safety factor  $K$ . The contact is characterized by the friction coefficient  $f$  and the surface roughness  $Ra_1$  and  $Ra_2$  for shaft and hub respectively. Temperature differences open up the range of possible interferences and need to be taken into account. The linear expansion coefficients  $\alpha_1$  and  $\alpha_2$  for shaft and hub respectively together with the average volumetric temperatures  $t_1$  and  $t_2$  quantify the amount that the connection loosens up when heated.

The results give the minimum and maximum required interference  $N_{min,req}$  and

$N_{max,req}$  as well as the chosen fits. The H7/u7 fit provides an acceptable interference for both shafts. The mounting of this connection can be done in a press or by heating the wheel and cooling the shaft.  $\Delta T$  is the temperature difference necessary to mount the wheel on the shaft without an axial force acting  $F_s$  is the axial force necessary to mount the wheel on the shaft without a temperature difference.

**Table 4.7:** Calculation inputs and results for the press fits of the shaft-wheel connections.

Input	Unit	Upper Shaft	Lower Shaft
Geometry			
$d$	mm	100	145
$d_1$	mm	0	0
$d_2$	mm	135	198
$l$	mm	165	180
Material			
$E$	MPa	2.1e6	2.1e6
$\nu$	–	0.3	0.3
$\sigma_{Y,1}$	MPa	275	275
$\sigma_{Y,2}$	MPa	360	360
Forces			
$F_a$	kN	21.8	21.8
$T$	Nm	6532	6532
Calculation factors			
$K$	–	3	3
$f$	–	0.14	0.14
$Ra_1$	$\mu\text{m}$	0.8	0.8
$Ra_2$	$\mu\text{m}$	1.6	1.6
$\alpha_1$	–	12e-6	12e-6
$\alpha_2$	–	12e-6	12e-6
$t_1$	$^{\circ}\text{C}$	20	40
$t_2$	$^{\circ}\text{C}$	40	40
Results			
$N_{min,req}$	$\mu\text{m}$	82.1	132
$N_{max,req}$	$\mu\text{m}$	185	262
Fit	–	H7/u7	H7/u7
$N_{min}$	$\mu\text{m}$	119	171
$N_{max}$	$\mu\text{m}$	169	227
$\Delta T$	$^{\circ}\text{C}$	173	159
$F_s$	kN	765	1177

## FEM stability calculations

Critical elements difficult to be analyzed analytically but presenting high risk of breaking are studied using the Finite Element solver implemented in the commercial software CATIA.

### Lantern Sides

The Lantern Sides are the parts presented in the drawing Figure B.20 in Appendix B.3 "List of Parts". Together with the Top Disk, they are the first elements transmitting the vertical force to the upper wheel. Due to strong displacement induced in the upper wheel from the squealing, high lateral forces are expected on the inside on the lantern sides, where the bearing housing is mounted.

Shown in Figure 4.18 are the elements fully clamped in space for the lantern sides during the study as those feet are mounted using two M8 screws on each supporting plate.

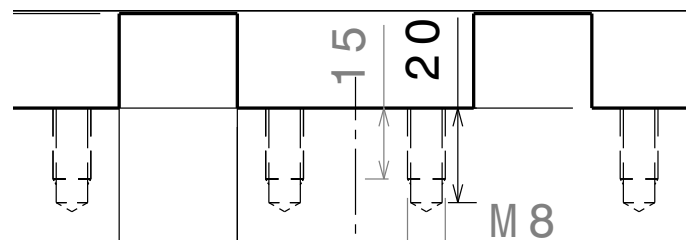


**Figure 4.18:** Lantern Side Clamped Feet

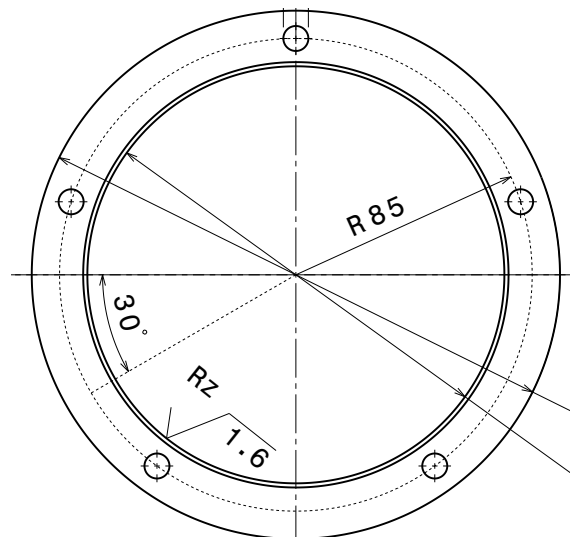


**Figure 4.19:** Lantern Side Contacting Surface with Bearing Housing

The surface area where the bearing housing is in contact with the lantern side is  $0.01 \text{ m}^2$ . According to Table 4.5, the maximum axial load that one side should be able to withstand is 18kN. On the surface shown in 4.19, it is found that applying such a force induces a lateral displacement of at most  $25 \mu\text{m}$  at the bearing housing

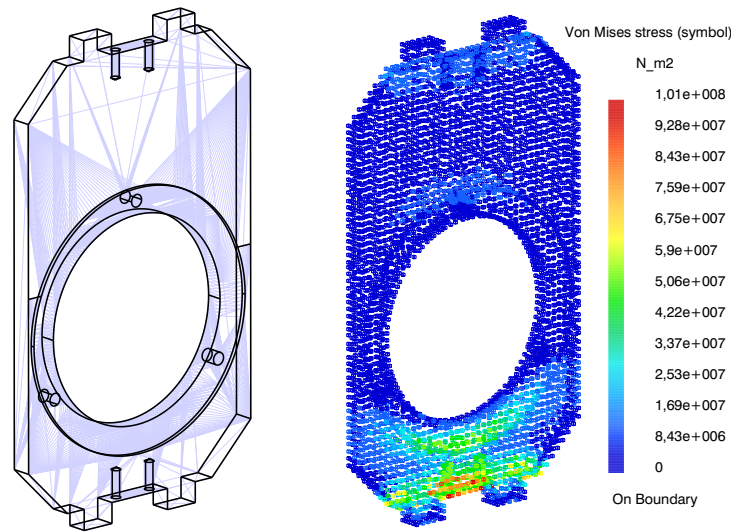


**Figure 4.20:** Lantern Side Von Mises Stress under a Force of 18 kN

position. A maximum stress is found in the area between the two lower feet as shown in Figure 4.20.

**Table 4.8:** Lateral Displacement and Maximum Stress in Local Critical Area of the Lantern Side Plate as Function of Applied Force.

Force Applied in kN	18
Lateral Displacement in mm	0.025
Maximum Stress in MPa	10.1

The maximum stress achieved here is far below the yield strength value of steel, and therefore the design of the plate should hold lateral displacement values. This maximum stress can be as low as 200 MPa for weaker steels, and would represent a vibrational displacement of half a millimeter.

### Lower side plates

Like for the upper axle, the supports of the lower axle bearings are studied using FE analysis. The supports are again shaped like a plate with different holes, and instead of being hold from the bottom and top, are simply mounted from below and the side to a Lower Bottom Plate. As a results, the parts shown is Figure 4.21 taken from Appendix B.23 are clamped in space in the software.

A similar surface of  $0.014\text{m}^2$  to the surface shown in 4.19 is in contact with the bearing housing of the lower axle, and needs to stand a lateral force of 19 kN according to Table 4.5. When applying this force, it is found that a displacement at the bearing housing position of  $6\ \mu\text{m}$ . The maximum Von Mises stress obtained from this displacement is shown is the following figure.

One can see that globally the plate is rather stiff. The maximum stress in around 8.6 MPa and is again way below the yield strength of steels. One can also notice

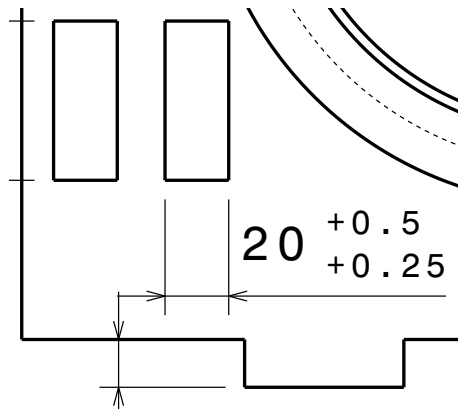


**Figure 4.21:** Half Clamped Elements on the Lower Side Plate

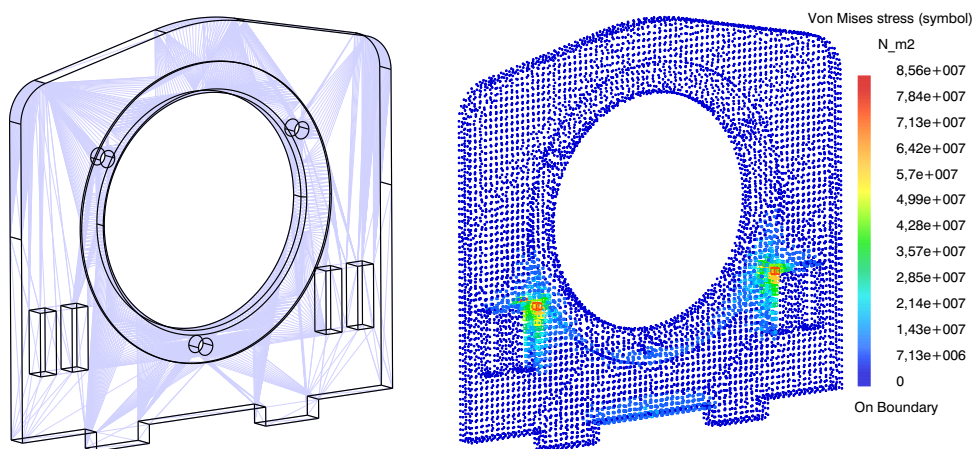


**Figure 4.22:** Lower Side Plate Von Mises Stress under a Force of 19 kN

that the high stresses concentrate around area that are clamped, and that are located at a corner close to the area where the force is applied. The surface where the consolidating element is mounted on is modelled using perfect sharp angle, which means that within this corner, the stress concentration can become infinite and can be potentially responsible for errors. In reality, that stress concentration will still be present, but it will probably be even lower so that in the end, the design of this Lower Side Plate is considered sufficiently robust.

**Table 4.9:** Lateral Displacement and Maximum Stress in Local Critical Area of the Lower Side Plate as Function of Applied Force.

Force Applied in kN	19
Lateral Displacement in mm	0.006
Maximum Stress in MPa	8.6

# 5

## Discussion

A number of findings and solutions demand a critical reflection, both in the design and the construction part of the thesis. Starting with the design section, it was found that changing the geometry has a significant influence on the receptance (see Figure 3.10). Furthermore, a method of introducing wheel damping by adding sheet metal layers is proposed. However, the impact of the added mass for the damping on the receptance is not considered.

The two considered speeds 35 km/h and 50 km/h are quite fast, when considering that the situation that is supposed to be replicated is a tram going around a tight curve. Squealing has been shown to occur for significantly lower speeds, for example 4 km/h [19]. It could be beneficial to research the squealing occurrence for such speeds when searching for an appropriate rail wheel geometry.

Looking at Figure 3.14, a division of the results in two groups is visible. One group is described by all results that have a lateral force level of below  $-120$  dB, and the other group can be characterized by results over more than  $-30$  dB. For an unknown reason, no results are found in between these two force levels. No further investigation was done to find the reason for this divide. However, if this behavior was not specific to this set of simulations, the divide could be used to replace the rather arbitrarily set 0 dB squealing criterion. Even though a squealing criterion of for example  $-40$  dB corresponds to a rather small force, it divides the results into a group where “something happens” and a group where “almost nothing happens”.

As pointed out in the introduction, some authors claim that squealing modes are axial modes [6, 10]. Admittedly, squealing was found at the frequency of 8580 Hz, where an axial mode of the rail wheel at 8576 Hz is coupled to a radial mode of the wheel at 8585 Hz. Even so, the method of using the lateral force as an indicator for squealing lacks an essential feature, namely the sound radiation. An excitation of the wheel by the lateral force only leads to squeal noise if the wheel also has a good radiation efficiency at that frequency. To quantify that, a more elaborate model as for example described in [29] is necessary.

Individual parameters could be analyzed more in depth but were not elaborated on. However, running such a study is time consuming, and some parameters like rolling speed and wheel damping that were assumed minor were only investigate a couple of time so that this detailed analysis cannot rely on a linearity assumption for any of the parameters.

A few points concerning the construction solutions need to be critically discussed. Since at the time of the report writing it is unclear what materials are accessible, rather weak materials have been assumed for the stability calculation. A better integration of the available materials into the calculation could have lead to a more

targeted design, possibly leading to a more lightweight design. On the other hand, a re-investigation of the stability after the rig is built could confirm a higher stability and therefore a larger range in which the rig can be used.

The lateral forces are planned to be measured using strain gages on the shaft. The idea to use slip rings for the transmission of the data from the rotating shaft to the stationary measurement equipment is followed. However, slip rings proved to be rather expensive pieces of hardware. It might be worth considering a wireless connection for the data transmission, as shown in [23]. Furthermore, the possibility of integrating force transducers into the bearing housings exists but was not investigated thoroughly.

The limitation of the maximum transmissible torque on the drive shaft is described to be done by the introduced star disks. And while star disks certainly limit the maximum transmissible torque, they are not specifically designed for this task. They are used in this case primarily to facilitate the lateral displacement of the lower shaft. A slipping of the star disks could potentially affect the surface of the involved shaft and hub or destroy the star disks themselves. It is therefore highly recommended to integrate a torque based control into the motor-control to limit the maximum aligning torque.

The rig is set up such that all settings can be changed from outside the ‘box’ described by the lower bottom plate and the upper top plate, connected by the four vertical I-profiles. This has benefits for safety, since the inner box can be encapsulated with either a fence if radiation measurements are conducted, and otherwise rigid plates. When using rigid plates, it can furthermore be used to test the influence of humidity and temperature.

Generally, this report can only to be understood as a design guideline. If the rig is actually build and operated, the full responsibility for the safety of the equipment and users lies in the person building and/or operating it. This is especially because the safety considerations are in a conceptual state in this report and need completion. Furthermore, not all involved parts are known at the point of report writing, making a detailed safety plan impossible.

# 6

## Conclusion and Outlook

This thesis presents a design proposal for a squealing noise test rig that can be used in a university environment for research and investigation of railway vehicle wheel squeal noise. A preliminary literature study revealed that other rigs built for similar purposes are often roller rigs, with two steel disks rolling on each other. Based on computational models and additional results from the literature study, the different parameters influencing squealing were located. In order to dimension the rig and to find the range of applicability of the parameters a parameter study was run. Sought was the best set of those parameters that would increase the likelihood for squealing to occur in the rig. The results of this study allowed a targeted selection of the upper wheel geometry and running a study was therefore suitable for this purpose. A plan for the construction of the rig was detailed in a CAD model. The non-standard parts included in the CAD model are described in drawings.

However, the geometry is still subject to reviews and modifications and will certainly undergo changes during its actual manufacturing and assembly. Guidelines for mounting and safety feature implementations are required before the rig is built. Furthermore, the monitoring and measuring of the rig as well as the motor control need to be elaborated on.

# Bibliography

- [1] M.J. Rudd. Wheel/rail noise—part ii: Wheel squeal. *Journal of Sound and Vibration*, 46(3):381 – 394, 1976.
- [2] P.J. Remington. Wheel/rail squeal and impact noise: What do we know? what don't we know? where do we go from here? *Journal of Sound and Vibration*, 116(2):339 – 353, 1987.
- [3] David Thompson. Curve squeal noise. In David Thompson, editor, *Railway Noise and Vibration*, chapter 9, pages 315 – 342. Elsevier, Oxford, 2009.
- [4] Maria A. Heckl and X.Y. Huang. Curve squeal of train wheels, part 3: Active control. *Journal of Sound and Vibration*, 229(3):709 – 735, 2000.
- [5] Thomas D. Rossing Prof., editor. *Springer Handbook of Acoustics*. Springer New York, 2 edition, 2007.
- [6] F. G. de Beer, M. H. A. Janssens, P. P. Kooijman, and W. J. van Vliet. Curve squeal of train wheels (part 1): Frequency domain calculation model. In *Proceedings of the INTER-NOISE*, volume 3, pages 1560–1563, 2000.
- [7] A. Pieringer. A numerical investigation of curve squeal in the case of constant wheel/rail friction. *Journal of Sound and Vibration*, 333(18):4295 – 4313, 2014.
- [8] A. Pieringer, W. Kropp, and D.J. Thompson. Investigation of the dynamic contact filter effect in vertical wheel/rail interaction using a 2d and a 3d non-hertzian contact model. *Wear*, 271(1–2):328 – 338, 2011. Proceedings of the 8th International Conference on Contact Mechanics and Wear of Rail / Wheel Systems, Florence, 2009.
- [9] Eric Cataldi-Spinola and Christoph Glocker. Curve squealing of railroad vehicles. In *5th EUROMECH Nonlinear Oscillations Conference*, pages 1970–1976, Eindhoven, Netherlands, August 2005.
- [10] P.A. Meehan, P. Bellette, X. Liu, C. Milne, and D. Anderson. Investigation of wheel squeal characteristics using a rolling contact two disk test rig. *9th Congress on Railway Research*, May 2011.
- [11] Maria A. Heckl. Curve squeal of train wheels, part 2: Which wheel modes are prone to squeal? *Journal of Sound and Vibration*, 229(3):695 – 707, 2000.
- [12] Paul A. Meehan and Xiaogang Liu. Prediction and investigation of wheel squeal amplitude. *12th International Workshop on Railway Noise*, 2016.
- [13] Jamil Abdo, Mohammed Tahat, Ahmed Abouelsoud, and Mohmoud Danish. The effect of frequency of vibration and humidity on the stick–slip amplitude. *International Journal of Mechanics and Materials in Design*, 6(1):45–51, 2010.
- [14] Xiaogang Liu and Paul A. Meehan. Wheel squeal noise: A simplified model to simulate the effect of rolling speed and angle of attack. *Journal of Sound and Vibration*, 338:184 – 198, 2015.

- [15] I. Zenzerovic, W. Kropp, and A. Pieringer. An engineering time-domain model for curve squeal: Tangential point-contact model and greens functions approach. *Journal of Sound and Vibration*, 376:149 – 165, 2016.
- [16] E. J. M. Hiensch and B. Lefranc. Development of a two-material rail allows engineering squeal noise behaviour. In *Euronoise Naples*. 2003.
- [17] D. Curley, D. C. Anderson, J. Jiang, and D. Hanson. *Field Trials of Gauge Face Lubrication and Top-of-Rail Friction Modification for Curve Noise Mitigation*, chapter Noise and Vibration Mitigation for Rail Transportations Systems, pages 449–456. Springer Berlin Heidelberg, Berlin, Heidelberg, 2015.
- [18] A.D. Monk-Steel, D.J. Thompson, F.G. de Beer, and M.H.A. Janssens. An investigation into the influence of longitudinal creepage on railway squeal noise due to lateral creepage. *Journal of Sound and Vibration*, 293(3–5):766 – 776, 2006. Proceedings of the Eighth International Workshop on Railway Noise Proceedings of the Eighth International Workshop on Railway Noise.
- [19] F. G. de Beer, M. H. A. Janssens, P. P. Kooijman, and W. J. van Vliet. Curve squeal of train wheels (part 2): Set-up for measurement of creepage dependent friction coefficient. In *Proceedings of the INTER-NOISE*, volume 3, pages 1564–1567, 2000.
- [20] D.J. Thompson, A.D. Monk-Steel, C.J.C. Jones, P.D. Allen, S.S. Hsu, and S.D. Iwnicki. Railway noise: Curve squeal, roughness growth, friction and wear. Technical report, The Institute of Sound & Vibration Research, The University of Southampton and The Rail Technology Unit, Manchester Metropolitan University, June 2003.
- [21] F. G. de Beer, M. H. A. Janssens, P. P. Kooijman, and W. J. van Vliet. Curve squeal of train wheels (part 3): Measurement method and results. In *Proceedings of the INTER-NOISE*, volume 3, pages 1568–1571, 2000.
- [22] Xiaogang Liu and Paul A. Meehan. Investigation of squeal noise under positive friction characteristics condition provided by friction modifiers. *Journal of Sound and Vibration*, 371:393 – 405, 2016.
- [23] E. Ji, J. Y. Kim, D. H. Hwang, J. H. Lee, K. J. Kim, and J. C. Kim. An experimental study of squeal noise characteristics for railway using a scale model test rig. In Liam Kian Meng, editor, *12th Western Pacific Acoustics Conference*, volume 306 - 311. Research Publishing, Singapore, 2015.
- [24] Moritz Gretschel and Alfred Jaschinski. Design of an active wheelset for a scale roller rig. *Vehicle System Dynamics*, 41(5):365–381, 2004.
- [25] Jean-Claude Samin and Paul Fiset. Railway vehicles: Wheel/rail model. In *Symbolic Modeling of Multibody Systems*, volume 112, pages 249–271. Springer Netherlands, 2003.
- [26] S. Iwnicki. *Handbook of Railway Vehicle Dynamics*. CRC Press, 2006.
- [27] Astrid Pieringer. *Time-Domain modelling of high-frequency Wheel/rail interaction*. PhD thesis, Chalmers University of Technology, 2011.
- [28] David Thompson. *Railway Noise and Vibration: Mechanisms, Modelling and Means of Control*, volume 1. Institute of Sound and Vibration Research, University of Southampton, Southampton, UK, 2009.
- [29] Ivan Zenzerovic. *Engineering model for curve squeal formulated in time domain*. PhD thesis, Chalmers University of Technology, 2014.

- [30] AB SKF. Bogie designs. In *Railway technical handbook*, volume 1, chapter 2, pages 24–41. 2012.
- [31] B. F. Feeny and F. C. Moon. Quenching stick-slip chaos with dither. *Journal of Sound and Vibration*, 1(237):173–180, 2000.
- [32] Ringspann GmbH. Star disks for frequent clamping and loosening short axial width. online, 07 2017. Ringspann.de/.
- [33] Oleg P. Lelikov, Ludger Deters, Frank Dammel, Jens Freudenberger, Hen-Geul Yeh, and Thomas Böllinghaus et al. *Springer Handbook of Mechanical Engineering*, volume 1. Karl-Heinrich Grote and Erik K. Antonsson, 2009.
- [34] AB SKF. Basic rating life. online, 07 2017. www.skf.com.
- [35] AB SKF. Equivalent dynamic bearing load. online, 07 2017. www.skf.com.
- [36] AB SKF. Loads. online, 07 2017. www.skf.com.
- [37] AB SKF. Equivalent static bearing load. online, 07 2017. www.skf.com.
- [38] Dietmar Gross, Werner Hauger, Jörg Schröder, Wolfgang A. Wall, and Nimal Rajapakse. *Engineering Mechanics 1 - Statics*, volume 2. Springer Dordrecht Heidelberg New York London, 2013.
- [39] AB SKF. Deep groove ball bearings - 6017-2rs1. online, 07 2017. www.skf.com.
- [40] AB SKF. Deep groove ball bearings - 6020-2rs1. online, 07 2017. www.skf.com.



# A

## Appendix - Design

### Upper Wheel Geometries Eigenmodes

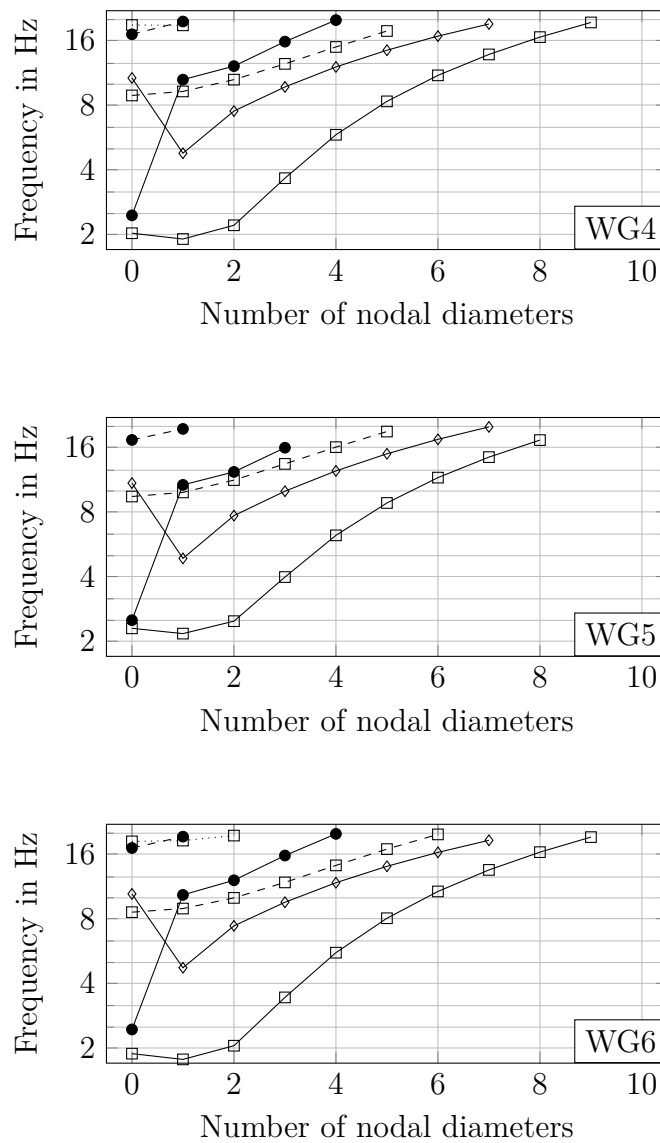


**Figure A.1:** Axial modes are with square marks, radial modes with diamonds and circumferential modes with circles. Solid, dashed and dotted lines are respectively for zero, one and two nodal circles.

# Parameter Study Results

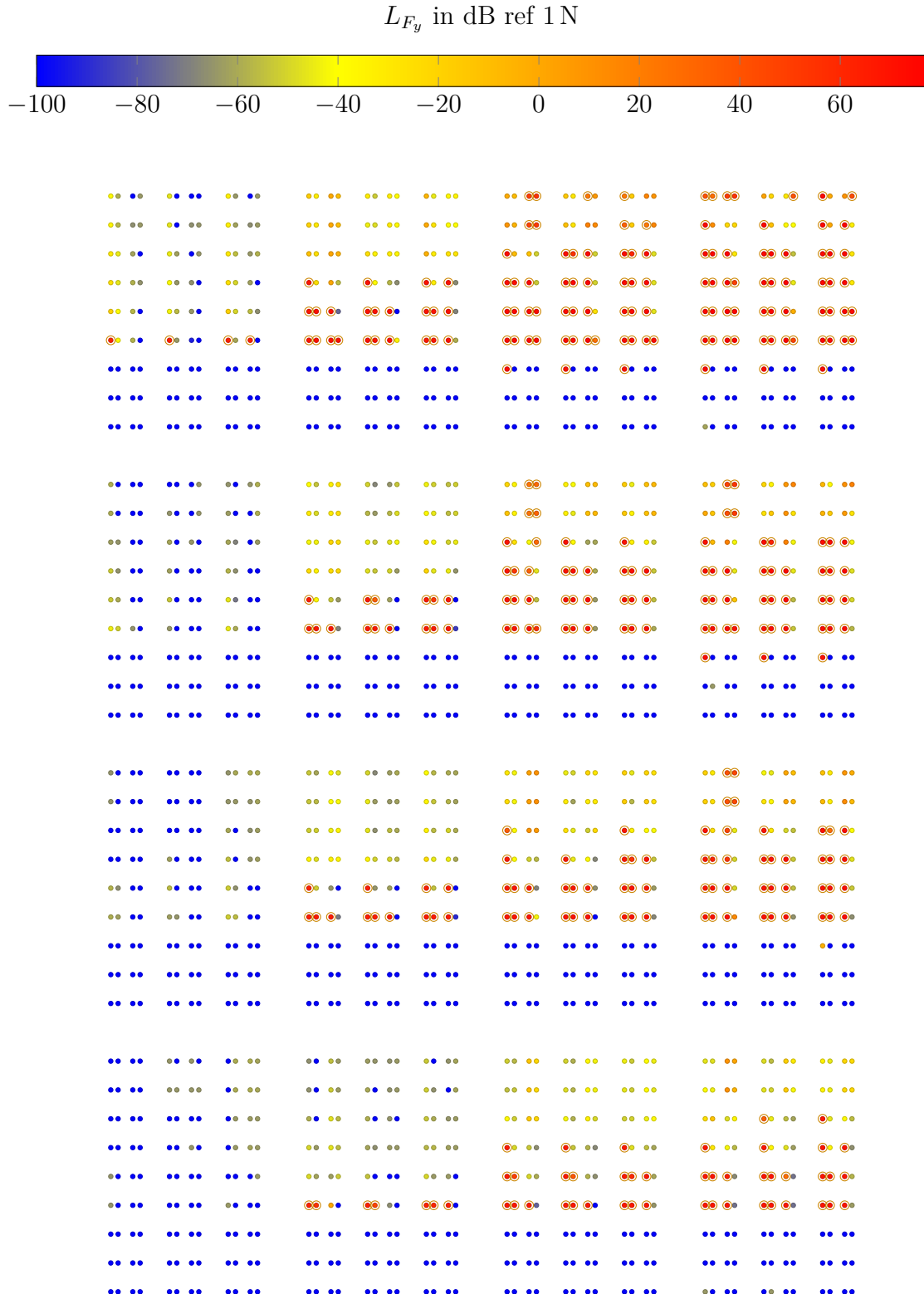


Figure A.2: Result plot for simulations with wheel geometry WG6.

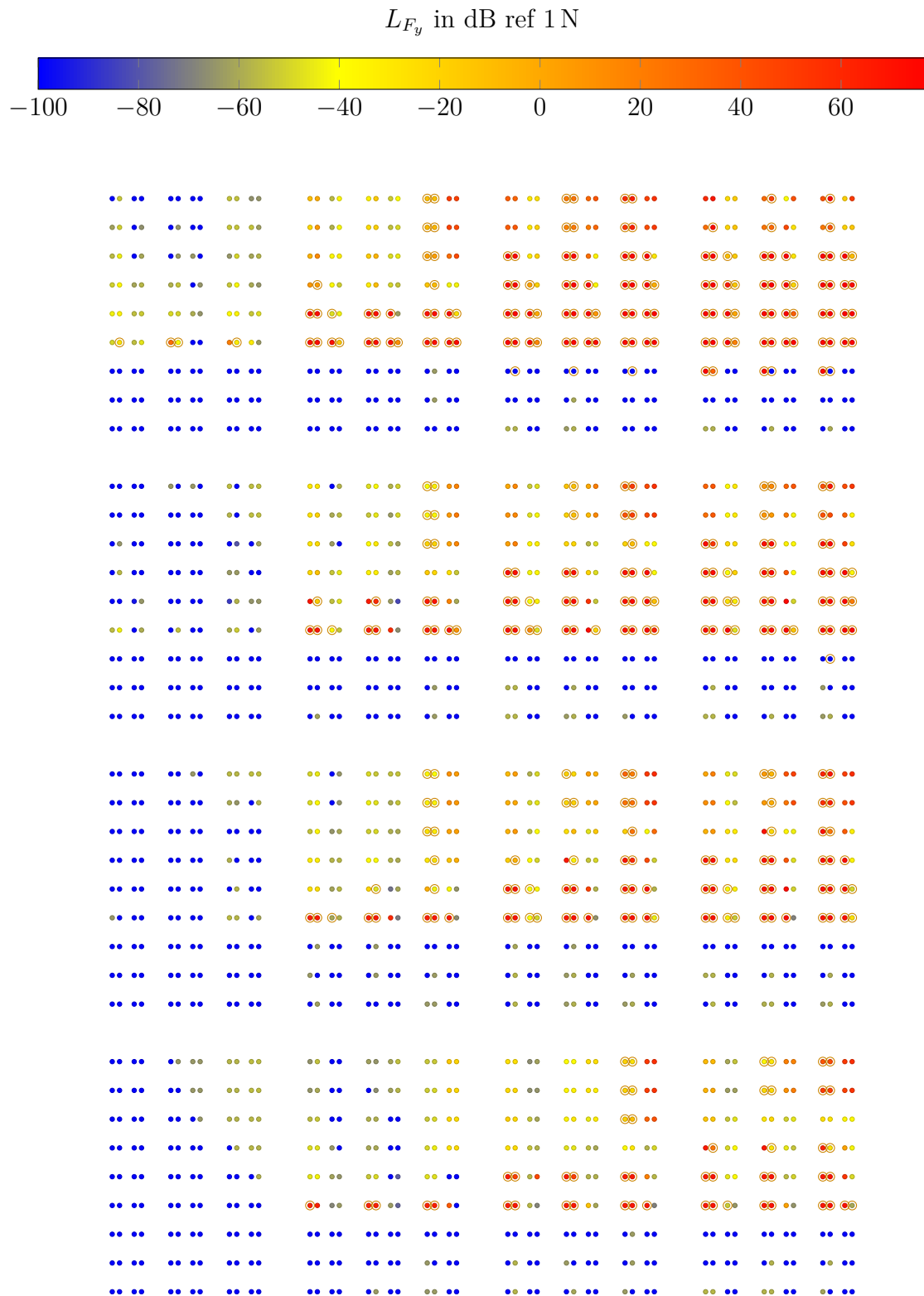
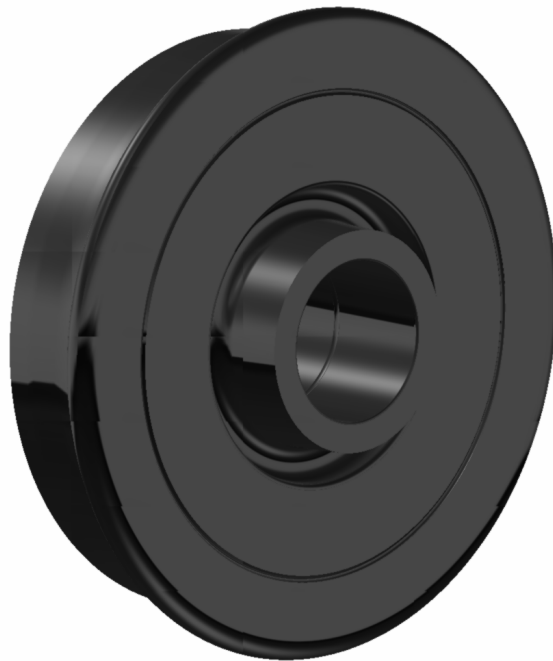


Figure A.3: Result plot for simulations with wheel geometry WG4.

## Lower Wheel Mockup



**Figure A.4:** Back View of the Lower Wheel



**Figure A.5:** Front View of the Lower Wheel

# B

## Appendix - Construction

### **Bearing Data Sheets**

The bearing data sheets are shown in Figure B.1 for the bearing type 6017 and Figure B.2 for the bearings Type 6020.

### **Star Disks Data Sheets**

The two paged data sheet for the star disks is shown in Figures B.3 and B.4.

### **List of Parts**

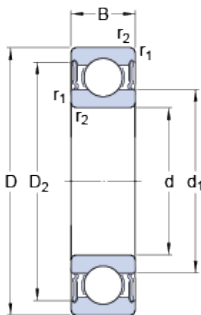
As a last step before the manufacturing and construction of the actual rig, a compact list of all parts included in the test rig, sorted by their assembly group is presented. It needs to be pointed out that the list is not entirely complete, since not all parts are included in the mock-up at the time of report writing. Missing parts include the damping materials, protection fences, any type of sensory equipment, and others. Furthermore, some parts are listed but not fully described, like the grease used (number 05-01-012) or most of the parts belonging to the driving unit assembly. However, since during the continuation of the project outside of this report the rig is inevitably going to undergo now unforeseen changes, it is impossible to present a comprehensive list of parts at this point.



## 6017-2RS1

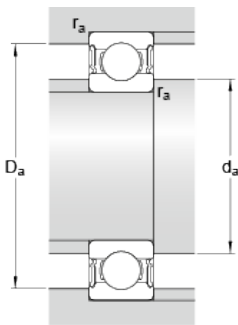
SKF Explorer

### Dimensions



d	85
D	130
B	22
$d_1$	≈ 99.4
$D_2$	≈ 119.1
$r_{1,2}$	min. 1.1

### Abutment dimensions



$d_a$	min. 92
$d_a$	max. 99.3
$D_a$	max. 123
$r_a$	max. 1

### Calculation data

Basic dynamic load rating	C	52
Basic static load rating	$C_0$	43
Fatigue load limit	$P_u$	1.76
Limiting speed		3000
Calculation factor	$k_r$	0.025
Calculation factor	$f_0$	15.8

### Mass

Mass bearing	0.929
--------------	-------

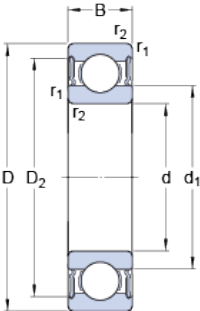
Figure B.1: Data Sheet for Bearing Type 6017-2RS1 from [39].



**6020-2RS1**

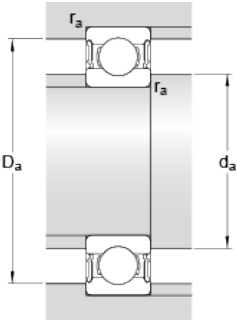
SKF Explorer

**Dimensions**



d		100
D		150
B		24
d <sub>1</sub>	≈	115.95
D <sub>2</sub>	≈	138.3
r <sub>1,2</sub>	min.	1.5

**Abutment dimensions**



d <sub>a</sub>	min.	107
d <sub>a</sub>	max.	115.9
D <sub>a</sub>	max.	143
r <sub>a</sub>	max.	1.5

**Calculation data**

Basic dynamic load rating	C	63.7
Basic static load rating	C <sub>0</sub>	54
Fatigue load limit	P <sub>u</sub>	2.04
Limiting speed		2600
Calculation factor	k <sub>r</sub>	0.025
Calculation factor	f <sub>0</sub>	15.9

**Mass**

Mass bearing		1.296
--------------	--	-------

Figure B.2: Data Sheet for Bearing Type 6020-2RS1 from [40].

**Star Discs**

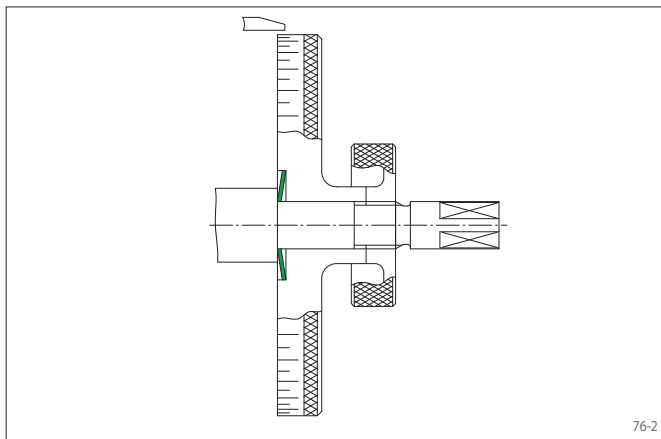
**for frequent clamping and loosening  
short axial width**



76-1

**Features**

- For frequent clamping and release
- Short axial width
- Adjustable to the required torque by multiple arrangements in the form of disc packs
- Low actuating force required, thus ideal for manual actuation



76-2

**Application example**

Backlash free attachment of a graduated dial in a feed unit with a Star Disc. After release of the right knurled nut, the dial can be adjusted in circumferential direction.

**Transmissible torques**

The transmissible torques or axial forces listed on the following page are subject to the following information about disc pack, tolerances, surface characteristics and material requirements. Please contact us in the case of deviations.

Disc Pack

The torque M stated in the table applies for one star disc. In case of multiple arrangements of star discs in disc packs of up to 16 star discs, the following applies:

Torque	$M_n = n \cdot M$
Preload force	$E_n = n \cdot E$
Load-bearing axial width	$L_1 \approx n \cdot s$

Tolerances

- h9 for shaft diameter d
- H9 for hub bore D

Surfaces

Average surface roughness at the contact surfaces between the shaft and the hub bore:  
 $R_z = 10 \dots 25 \mu\text{m}$ .

Materials

The following apply to the shaft and the hub:

- Yield strength  $R_e \geq 300 \text{ N/mm}^2$
- E-module  $\geq 170 \text{ kN/mm}^2$

**Example for ordering**

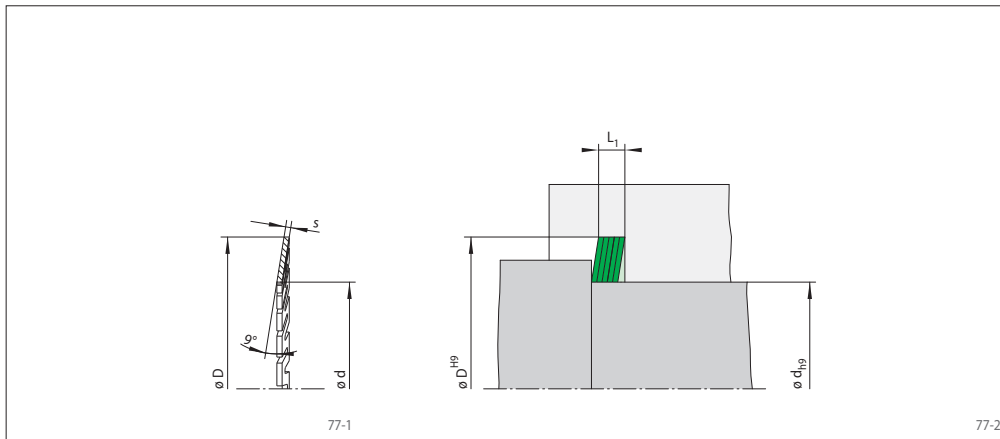
- 100 Star Discs for shaft diameter  $d = 20 \text{ mm}$ :
- 100 pcs. A 20 SS 37  
Article number 1032-037004-000000

**Figure B.3:** Data Sheet for Star Disks, page 1/2, from [32].

**Star Discs**



for frequent clamping and loosening  
short axial width



Dimensions			Technical Data					Type	Article number	
d	Size	D	s	Transmissible torque M	Contact pressure at Shaft $P_W$	Hub $P_N$	Preload force E	Weight		
mm		mm	mm	Nm	$N/mm^2$	$N/mm^2$	N	kg/100 pieces		
4	14	14	0,50	0,16	100	29	140	0,3	A 4 SS 14	1032-014002-000000
5	14	14	0,50	0,29	116	41	210	0,3	A 5 SS 14	1032-014003-000000
6	18	18	0,50	0,34	94	31	180	0,5	A 6 SS 18	1032-018001-000000
8	18	18	0,50	0,72	113	50	310	0,5	A 8 SS 18	1032-018003-000000
10	22	22	0,60	1,26	105	48	430	0,9	A 10 SS 22	1032-022002-000000
11	22	22	0,60	1,53	105	53	500	0,8	A 11 SS 22	1032-022003-000000
12	27	27	0,65	1,95	104	46	520	1,4	A 12 SS 27	1032-027001-000000
14	27	27	0,65	2,80	110	57	680	1,3	A 14 SS 27	1032-027003-000000
15	27	27	0,65	3,30	113	63	770	1,2	A 15 SS 27	1032-027004-000000
16	37	37	0,90	5,10	111	48	1030	3,7	A 16 SS 37	1032-037001-000000
17	37	37	0,90	5,90	113	52	1150	3,6	A 17 SS 37	1032-037002-000000
18	37	37	0,90	6,80	117	57	1270	3,5	A 18 SS 37	1032-037003-000000
20	37	37	0,90	8,70	121	65	1540	3,2	A 20 SS 37	1032-037004-000000
22	42	42	0,90	9,90	114	60	1490	4,3	A 22 SS 42	1032-042001-000000
24	42	42	0,90	12,2	118	67	1760	4,0	A 24 SS 42	1032-042002-000000
25	42	42	0,90	13,5	120	71	1900	3,8	A 25 SS 42	1032-042003-000000
28	52	52	1,15	21,0	116	63	2550	8,2	A 28 SS 52	1032-052001-000000
30	52	52	1,15	25,0	121	70	2900	7,7	A 30 SS 52	1032-052002-000000
35	52	52	1,15	33,5	119	80	3750	6,3	A 35 SS 52	1032-052004-000000
38	62	62	1,15	40,5	122	75	3600	10,2	A 38 SS 62	1032-062001-000000
40	62	62	1,15	45,5	124	80	4000	9,5	A 40 SS 62	1032-062002-000000
42	62	62	1,15	51,0	126	85	4450	8,8	A 42 SS 62	1032-062003-000000
45	62	62	1,15	60,0	129	94	5200	7,7	A 45 SS 62	1032-062004-000000
48	70	70	1,15	68,0	128	88	5000	11,0	A 48 SS 70	1032-070001-000000
50	70	70	1,15	75,0	130	93	5500	10,2	A 50 SS 70	1032-070002-000000
55	70	70	1,15	93,0	134	105	7000	8,0	A 55 SS 70	1032-070003-000000
60	80	80	1,15	112	135	101	6800	11,9	A 080 060 IV	1032-080001-000000
65	90	90	1,15	131	135	97	6700	16,5	A 090 065 IV	1032-090001-000000
70	90	90	1,15	154	137	106	8000	13,6	A 090 070 IV	1032-090002-000000
75	100	100	1,15	176	136	102	7800	18,6	A 100 075 IV	1032-100001-000000
80	100	100	1,15	205	139	111	9300	15,3	A 100 080 IV	1032-100002-000000
85	110	110	1,15	230	138	107	9000	20,7	A 110 085 IV	1032-110001-000000
100	120	120	1,15	325	141	118	11900	18,7	A 120 100 IV	1032-120001-000000

Figure B.4: Data Sheet for Star Discs, page 2/2, from [32].

X

**Table B.1:** List of Parts includes all parts that are described and included in the Mock-up at the time of report completion. Parts that are manufactured (marked with “make” in the Make/Buy-column) are further described by the drawings attached below.

Assembly	Sub Assembly	Part Name	Part Number	Amount	Serial Number/ISO	Drawing Number	Assembled to	Make / Buy	Manufacturing	Drawing revision
01 - cage	XX	bottomPlate	001	1		01-XX-001	cage	make	Laser	2
		upperGuiders	002	6		01-XX-002	cage	make	Laser	1
		largeSidePlate	003	4		01-XX-003	cage	make	Laser	2
		smallSidePlate	004	4		01-XX-004	cage	make	Laser	2
		topPlate	005	1		01-XX-005	cage	make	Laser	3
		M8x40	006	6	ISO 4014	01-XX-006	cage	buy		
		M8x30	007	24	ISO 4017	01-XX-007	cage	buy		
		M8 Nut	008	14	ISO 4032	01-XX-008	cage	buy		
		M8 Shims	009	30		01-XX-009	cage	buy		
		M12x40	010	12	ISO 4017	01-XX-010	frame	buy		
		spacerPin	011	1		01-XX-011	cage	make	Turning	2
		M12 Shims	012	24		01-XX-012	frame	buy		
		M12 Nut	013	12	ISO 4032	01-XX-013	frame	buy		
		lowerGuiders	014	4		01-XX-014	cage	make	Laser	1
02 - tonearm	XX	M8 rod 400mm	001	1		02-XX-001	tonearm	buy		
		Flange	002	2		02-XX-002	tonearm	make	Laser	2
		M8 Angle Joints	003	2		02-XX-003	tonearm	buy		
		Spacer1200	004	4		02-XX-004	tonearm	make	Laser	1
		Spacer0200	005	10		02-XX-005	tonearm	make	Laser	1
		Spacer0050	006	10		02-XX-006	tonearm	make	Laser	1
		Spacer0025	007	10		02-XX-007	tonearm	make	Laser	1
		M8 Nut	008	4	ISO 4032	02-XX-008	tonearm	buy		
03 - rotating /lifting	01 - shaft	upperBearingHousing1	001	1		03-01-001	housing	make	Turning	1
		upperBearingupperHousing2	002	1		03-01-002	upperHousing	make	Turning	1
		upperBearingSpacer5mm	003	6		03-01-003	upperHousing	make	Laser	2
		upperBearingSpacer1mm	004	16		03-01-004	upperHousing	make	Laser	2
		BellevilleSpring 125mm	005	1	DIN 2093 Row B	03-01-005	upperHousing	buy		
		M8x50	006	3	ISO 4014	03-01-006	lantern	buy		
		M8 Nut	007	6	ISO 4032	03-01-007	lantern	buy		
		M8 Shims	008	6		03-01-008	lantern	buy		
		upperShaft	009	1		03-01-009	shaft	make	Turning	
		upperWheel	010	1		03-01-010	shaft	make	Turning	1
		upperBearing	011	2	SKF 6017- 2RS1	03-01-011	shaft	buy		
		upperBearingSpacer025mm	012	3		03-01-012	shaft	make	Laser	2

Assembly	Sub Assembly	Part Name	Part Number	Amount	Serial Number/ISO	Drawing Number	Assembled to	Make / Buy	Manufacturing	Drawing revision	
02 - lantern		M8x40 Grease Nipple 1/8"	013	3	ISO 4014	03-01-013	lantern	buy			
			014	2		03-01-014	shaft	buy			
		bottomDisc	001	1		03-02-001	lantern	make	Laser / Milling	2	
		sidePlate	002	2		03-02-002	lantern	make	Laser	3	
		topDisk	003	1		03-02-003	lantern	make	Laser / Milling	2	
		M8x30 M8 Shims	004	8	ISO 4017	03-02-004	lantern	buy			
			005	8		03-02-005	lantern	buy			
	04 - support	XX	lowerBottomPlate	001	1		04-XX-001	LowerSupport	make	Laser	2
			lowerSidePlate	002	2		04-XX-002	LowerSupport	make	Laser / Milling	2
			supportWall	003	8		04-XX-003	LowerSupport	make	Laser	2
			M12x40	004	8	ISO 4017	04-XX-004	frame	buy		
M12 Shims			005	16		04-XX-005	frame	buy			
M12 Nut			006	8	ISO 4032	04-XX-006	frame	buy			
M8x30			007	12		04-XX-007	LowerSupport	buy			
M12x100			008	6	ISO 4762	04-XX-008	LowerSubAssembly	buy			
M12 Shims			009	6		04-XX-009	LowerSubAssembly	buy			
M12 Nut			010	6	ISO 4032	04-XX-010	LowerSubAssembly	buy			
M8 Shims			011	12		04-XX-011	LowerSupport	buy			
05 - LowerSubAssembly	XX	lowerShaft	001	1		05-XX-001	LowerSubAssembly	make	Turning		
		lowerWheel	002	1		05-XX-002	LowerSubAssembly	buy		x	
		lowerBearing	003	2	SKF 6020-2RS1	05-XX-003	LowerSubAssembly	buy			
		sleeve	004	2		05-XX-004	LowerSubAssembly	make	Turning / Milling	1	
		lockRing for shaft 100mm	005	2	DIN 471	05-XX-005	lowerShaft	buy			
		lockRing for sleeve hole 150mm	006	2	DIN 472	05-XX-006	sleeve	buy			
		key	007	2		05-XX-007	sleeve	buy			
		spacerLockRing 3x150mm	008	2		05-XX-008	LowerSubAssembly	make	Laser	1	
		spacerLockRing 3x100mm	009	2		05-XX-009	LowerSubAssembly	make	Laser	1	
01 - lowerHousing		BearingHousing	001	2		05-01-001	lowerHousing	make	Turning	2	
		Lid	002	2		05-01-002	lowerHousing	make	Turning	1	
		BellevilleSpring 160mm	003	1		05-01-003	lowerHousing	buy			
		lowerSpacer1mm	004	20		05-01-004	lowerHousing	make	Laser	1	
		lowerSpacer5mm	005	20		05-01-005	lowerHousing	make	Laser	1	

Assembly	Sub Assembly	Part Name	Part Number	Amount	Serial Number/ISO	Drawing Number	Assembled to	Make / Buy	Manufacturing	Drawing revision	
06 - ForceArm	XX	M10x20	006	6		05-01-006	lowerHousing	buy			
		M10 Shims	007	6		05-01-007	lowerHousing	buy			
		lowerSpacer025mm	008	4		05-01-008	lowerHousing	make	Laser	1	
		lowerSpacer12mm	009	3		05-01-009	lowerHousing	make	Laser	1	
		M10x30	010	3		05-01-010	lowerHousing	buy			
		Grease Nipple 1/8"	011	2		05-01-011	lowerHousing	buy			
		Grease	012			05-01-012	lowerHousing	buy			
		hingeMoving	001	2			06-XX-001	ForceArm	make	Laser / Drilling	1
		stampBeam	002	2			06-XX-002	ForceArm	make	Laser / Drilling	2
		stampFoot	003	2			06-XX-003	ForceArm	make	Laser / Drilling	1
		stampBasePlate	004	1			06-XX-004	ForceArm	make	Laser	2
		frontEnd	005	1			06-XX-005	ForceArm	make	Laser	2
forceArmFix rear	006	1			06-XX-006	Frame	make	Laser	2		
forceArmFix front	007	1			06-XX-007	Frame	make	Laser	1		
forceArmFix_frontScrew	008	1			06-XX-008	ForceArm	make	Turning	1		
BellevilleSpring 40mm	009	12			06-XX-009	ForceArm	buy				
bolt	010	3			06-XX-010	ForceArm	make	Turning	1		
pin	011	6			06-XX-011	bolt	buy				
M8x40	012	8		ISO 4014	06-XX-012	Frame	buy				
M16x100	013	1		ISO 4017	06-XX-013	ForceArm	buy				
rearFoot	014	2			06-XX-014	ForceArm	make	Laser / Drilling	1		
07 - Frame	XX	I-Beam End Plate	001	28		07-XX-001	Frame	make	Laser	1	
		I-Beam vertical	002	4		07-XX-002	Frame	buy			
		I-Beam horizontal long	003	4		07-XX-003	Frame	buy			
		I-Beam horizontal short	004	4		07-XX-004	Frame	buy			
		M12x30	005	72		07-XX-005	Frame	buy			
		M12 Nut	006	80		07-XX-006	Frame	buy			
		M12 Shims	007	128		07-XX-007	Frame	buy			
		I-Beam motor long	008	2		07-XX-008	Frame	buy			
		I-Beam motor short	009	2		07-XX-009	Frame	buy			
		M12x35	010	8		07-XX-010	Frame	buy			
08 - DrivingUnit	XX	Motor	001	1		08-XX-001	DrivingUnit	buy			
		motorBasePlate	002	1		08-XX-002	DrivingUnit	make	Laser		
		Elastic Coupling	003	1		08-XX-003	DrivingUnit	buy			
		starDisk	004	5		08-XX-004	DrivingUnit	buy			

Assembly	Sub Assembly	Part Name	Part Number	Amount	Serial Number/ISO	Drawing Number	Assembled to	Make / Buy	Manufacturing	Drawing revision
		outerConnection	005	1		08-XX-006	DrivingUnit	make	Turning	
		outerPress	006	1		08-XX-006	DrivingUnit	make	Turning	
		M8x20	007	1	ISO 4017	08-XX-007	DrivingUnit	buy		
		Key motorside	008	1		08-XX-008	DrivingUnit	buy		
		Key rigside	009	1		08-XX-009	DrivingUnit	buy		

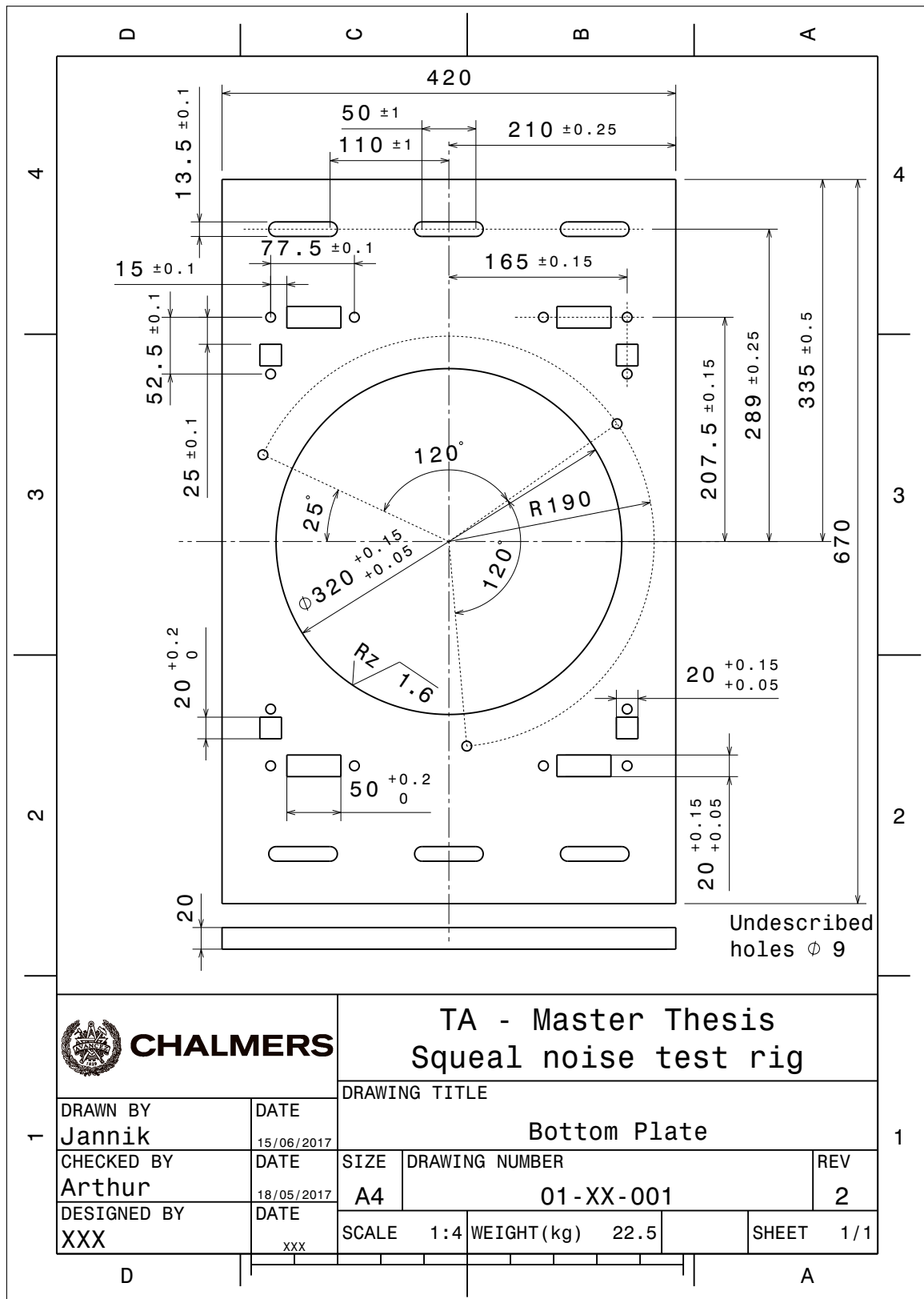


Figure B.5: Upper Bottom Plate

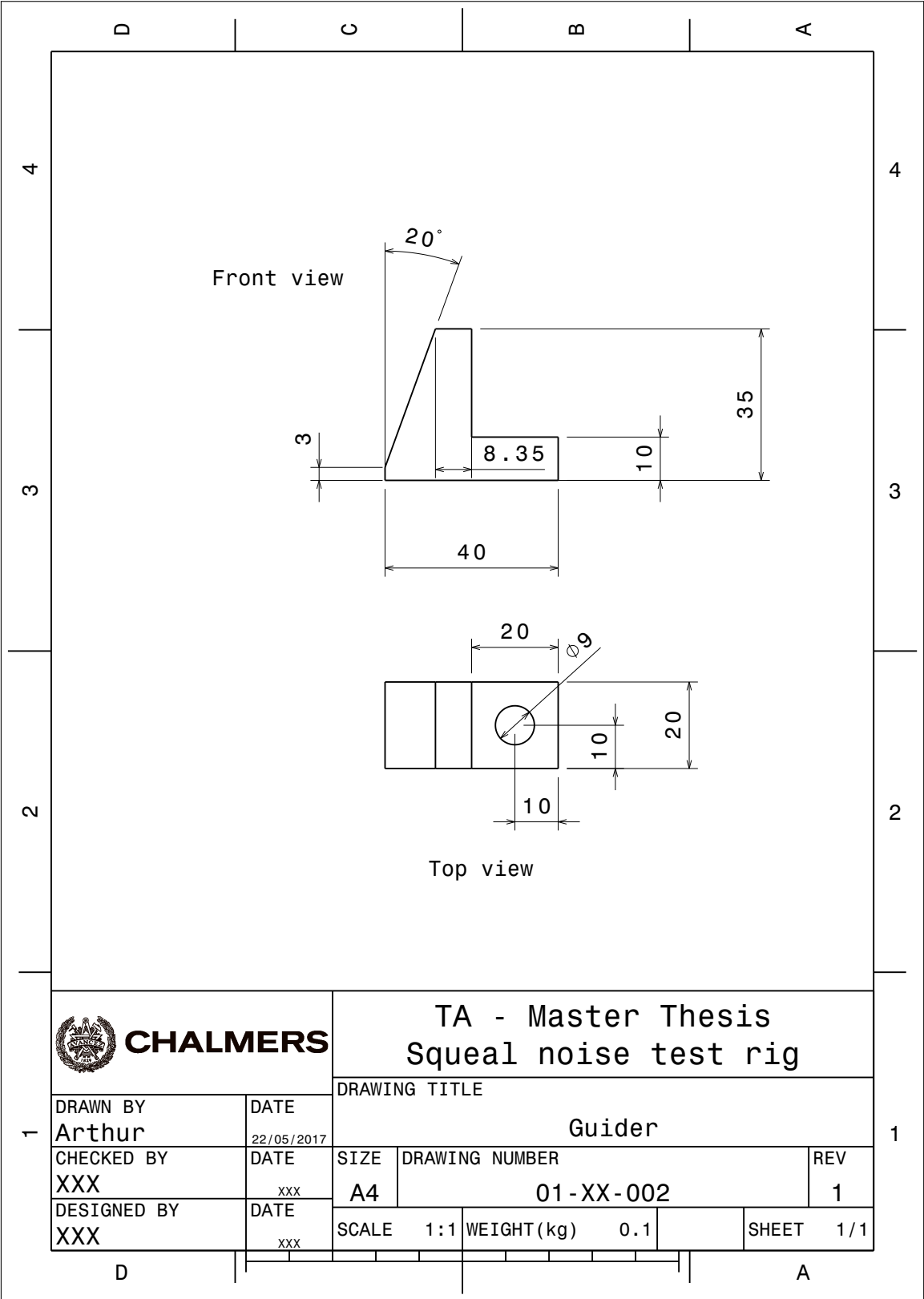


Figure B.6: Glider

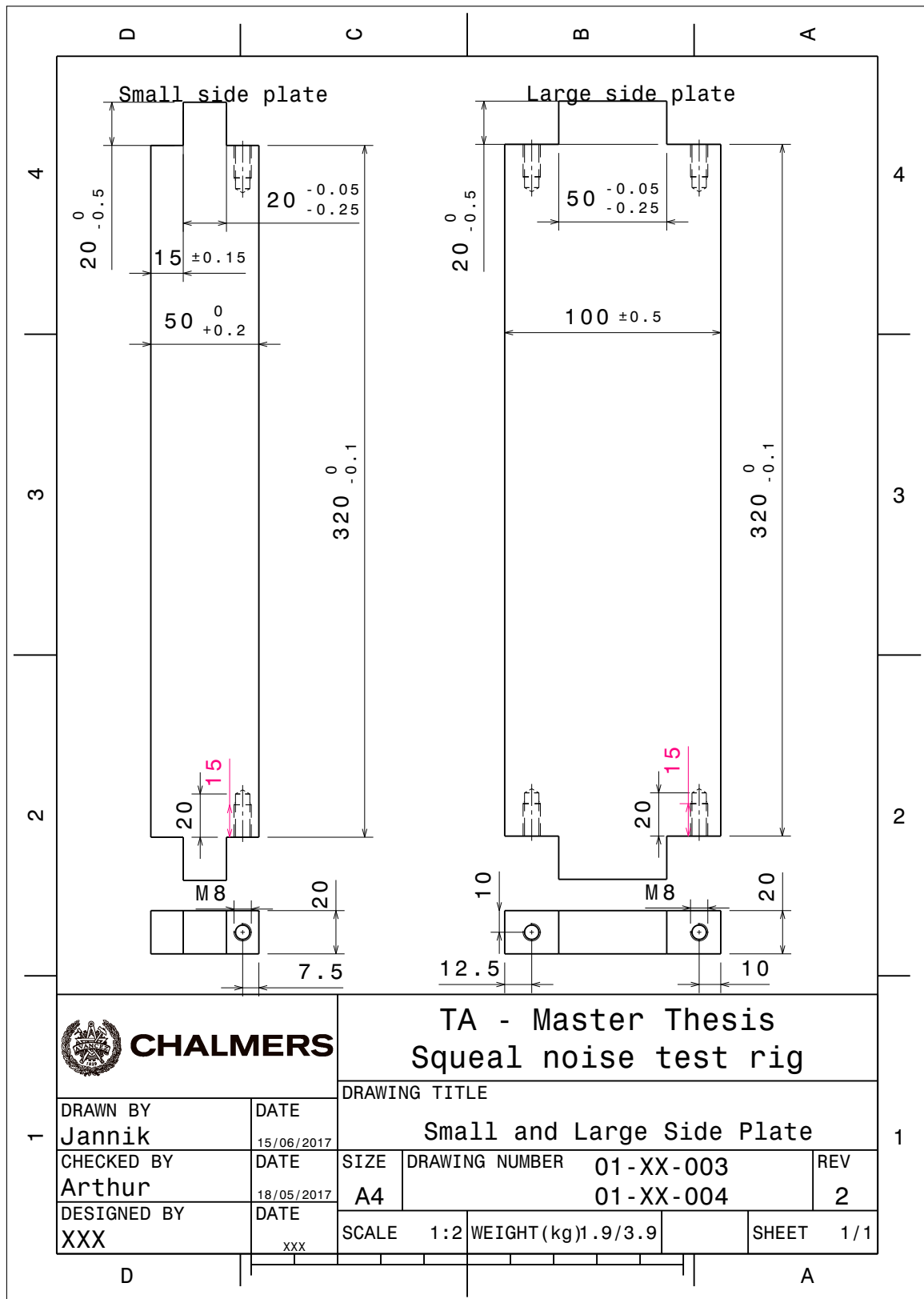


Figure B.7: Small and Large Side Plate

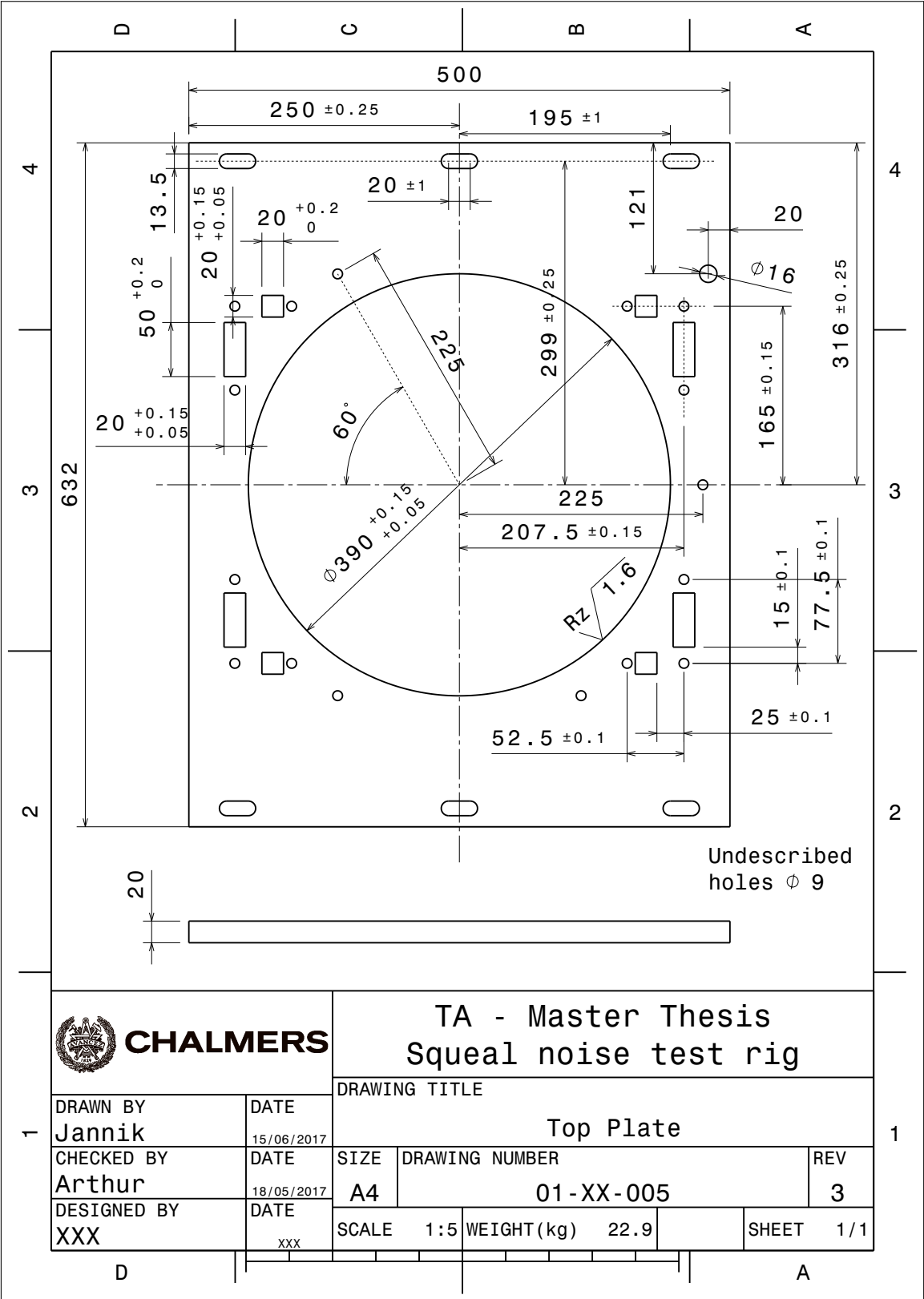


Figure B.8: Upper Top Plate

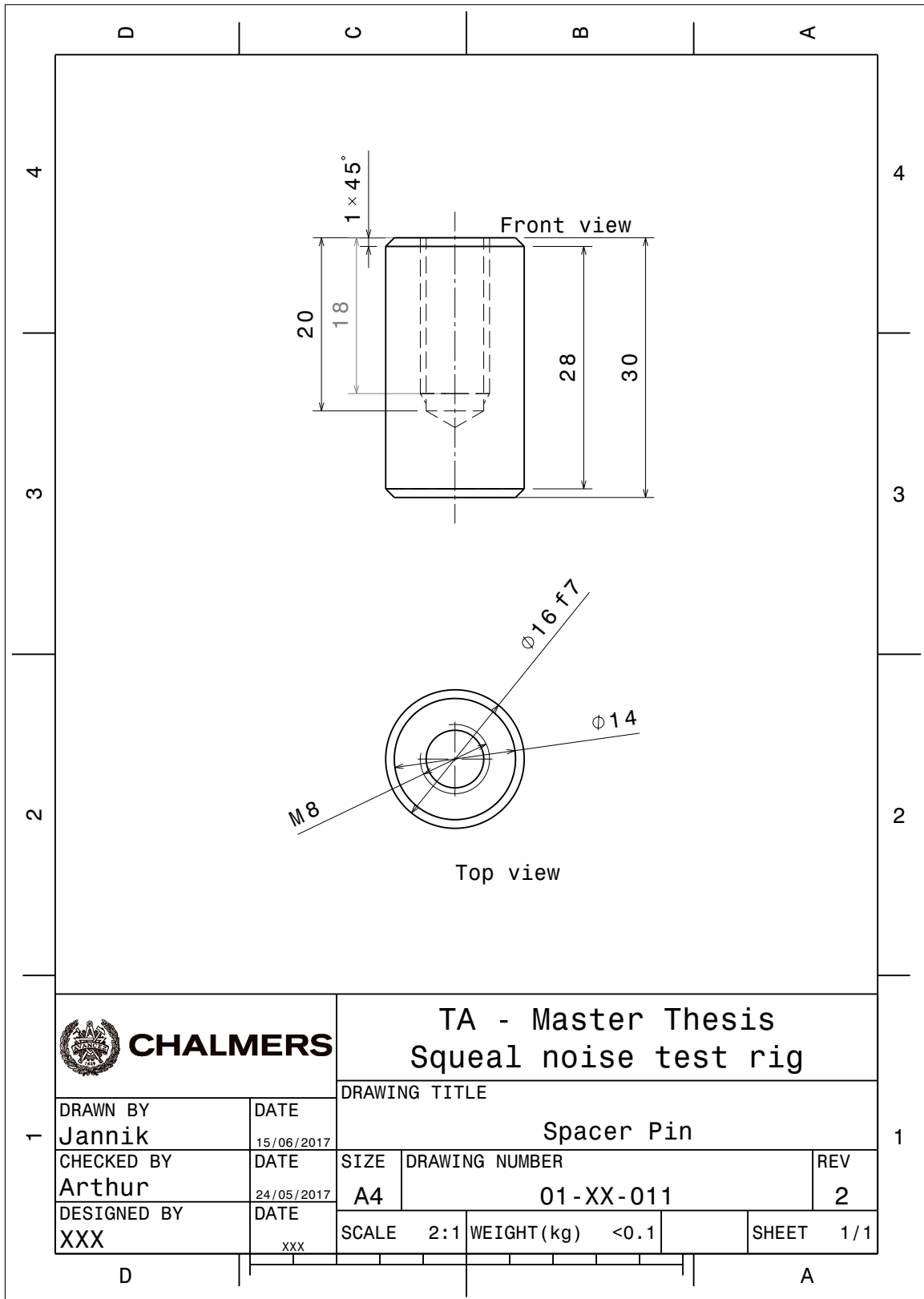


Figure B.9: Spacer Pin

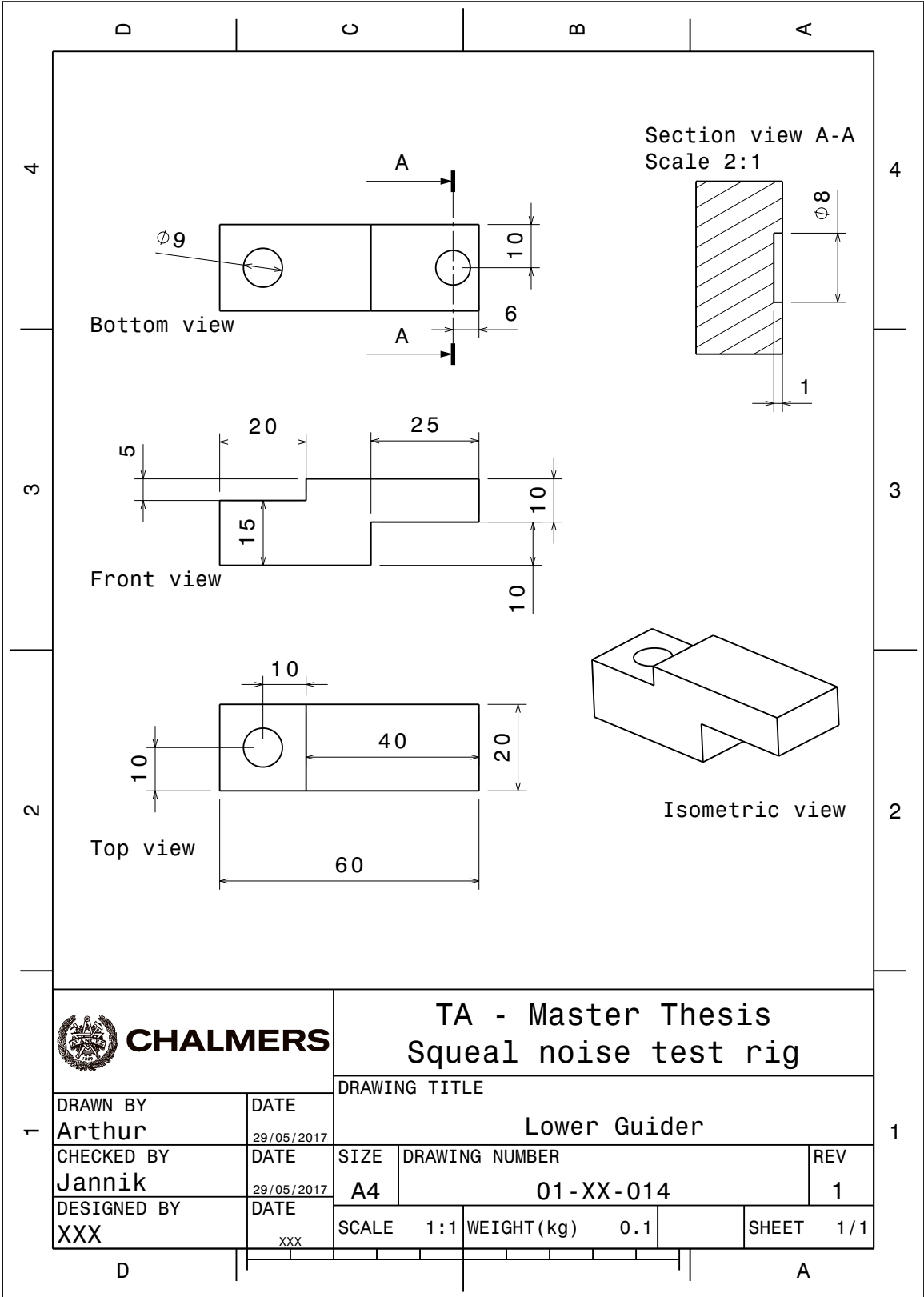


Figure B.10: Lower Guider

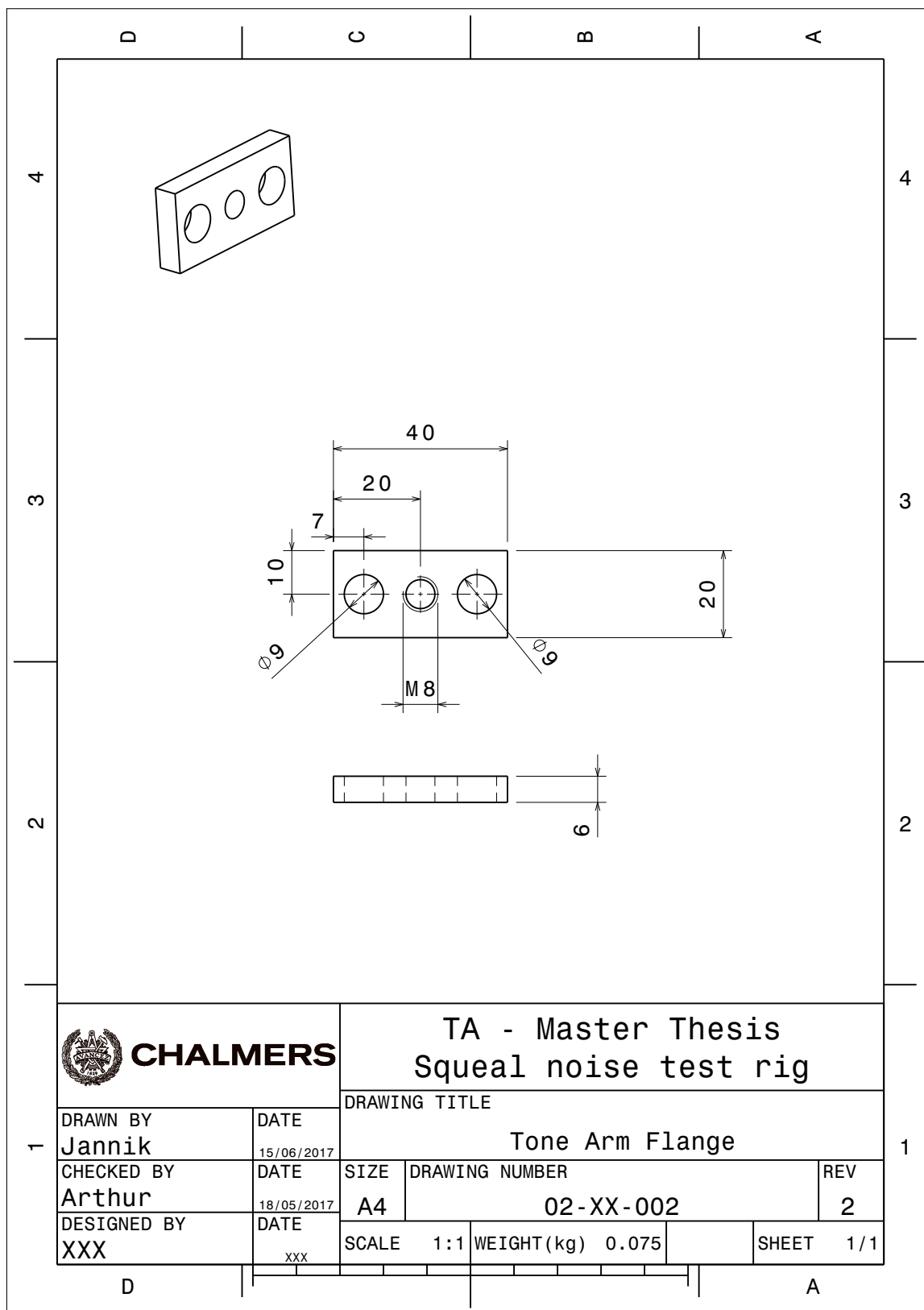


Figure B.11: Toone Arm Flange

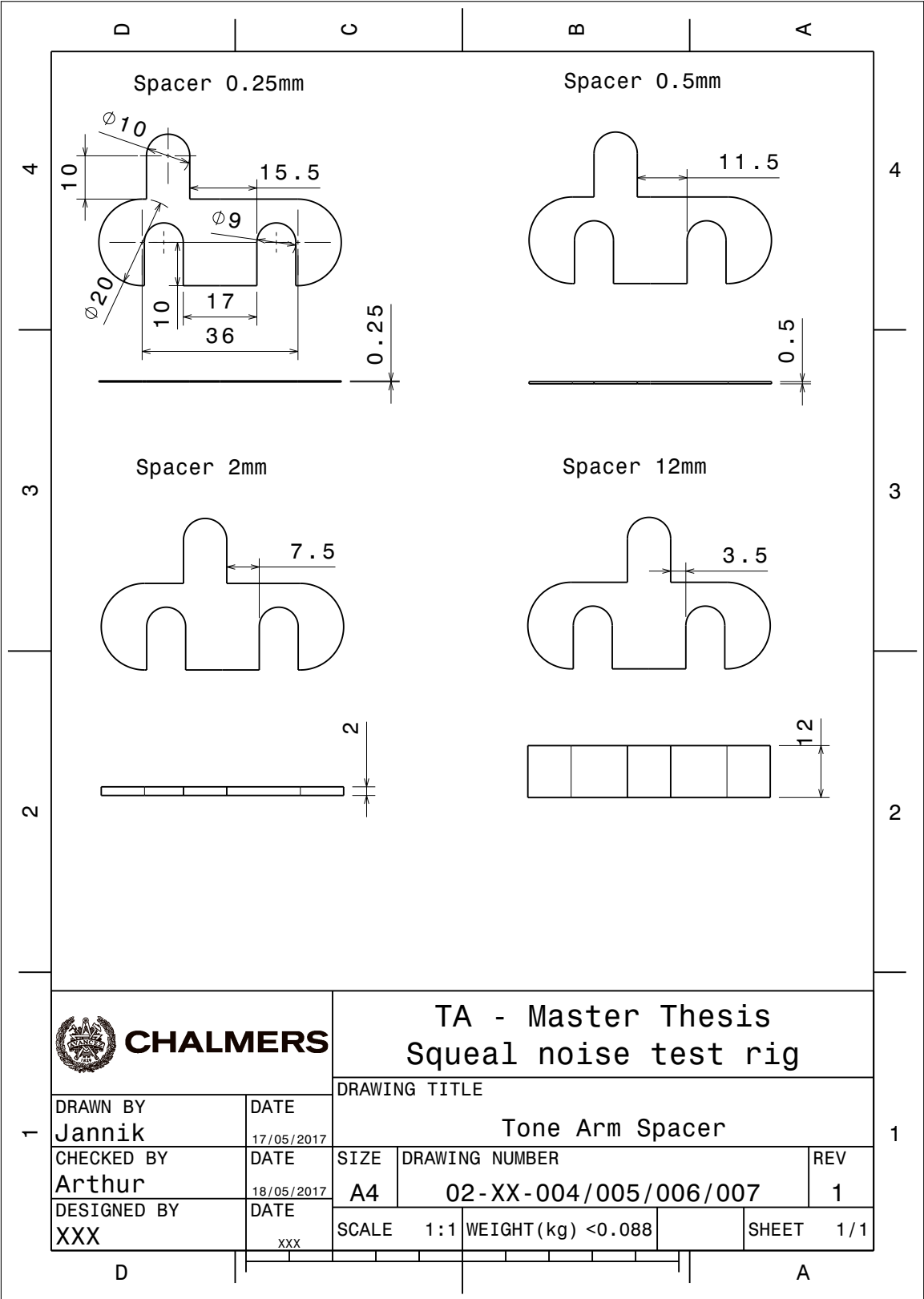


Figure B.12: Tone Arm Spacers

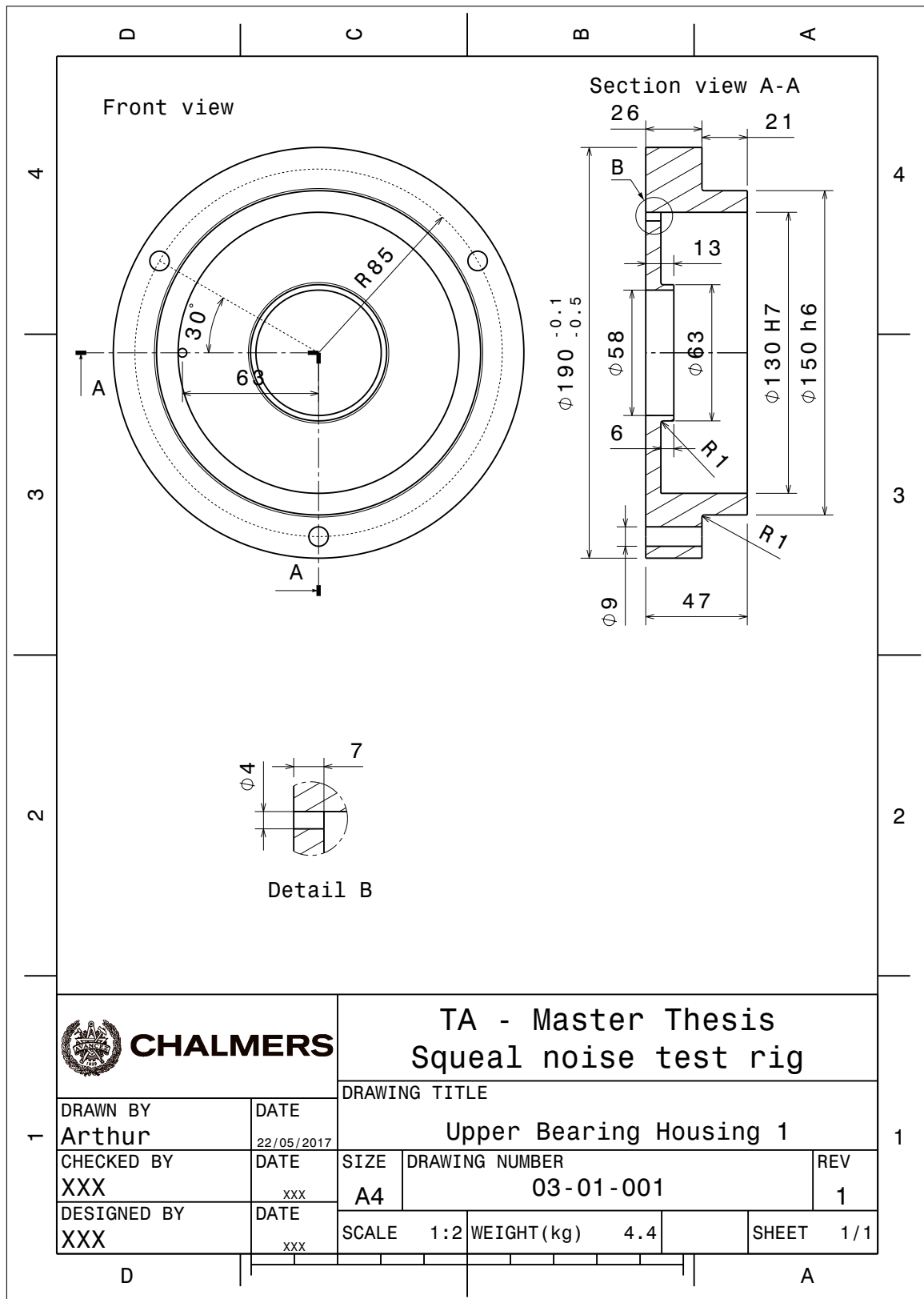


Figure B.13: Upper Bearing Housing 1

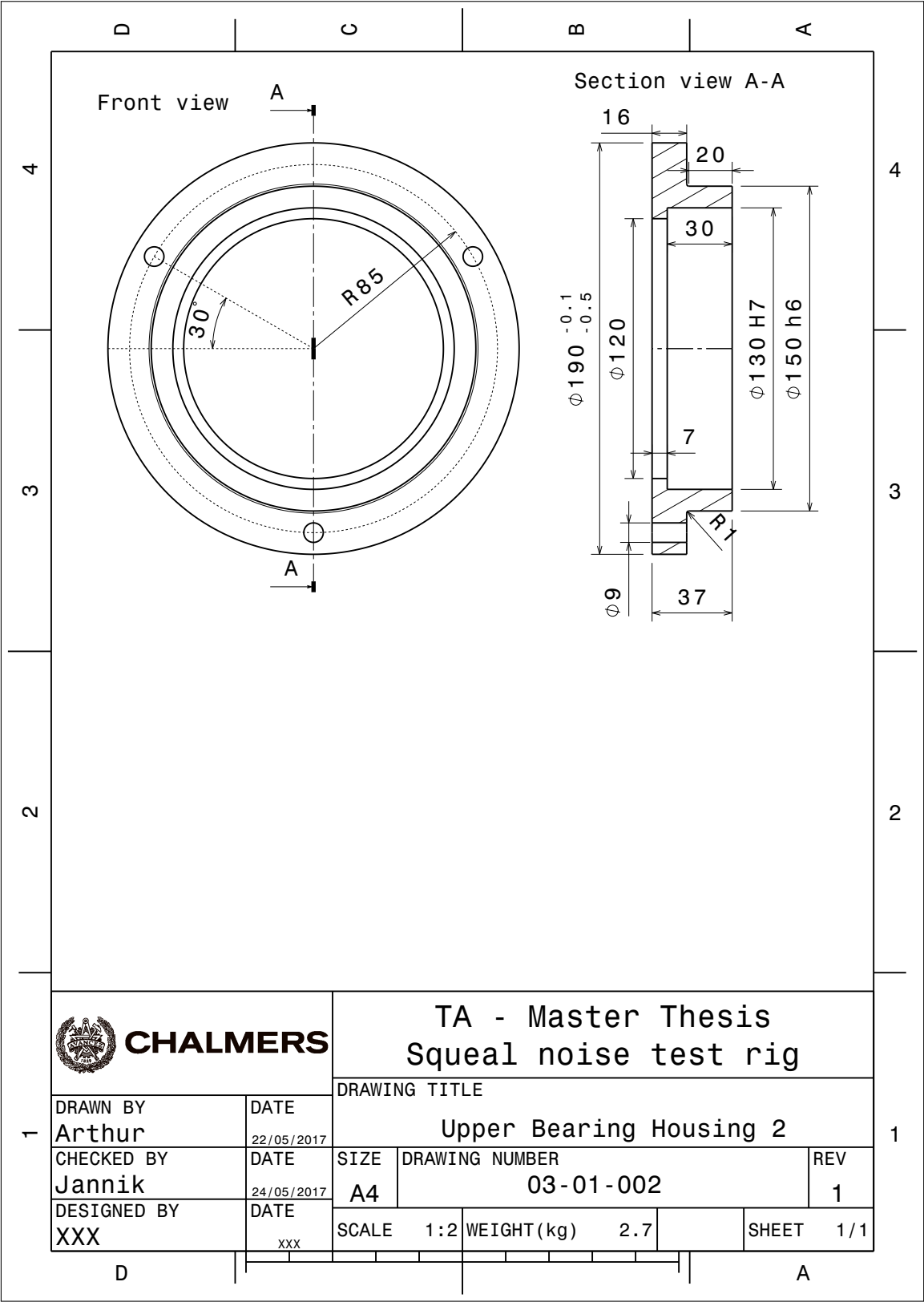


Figure B.14: Upper Bearing Housing 2

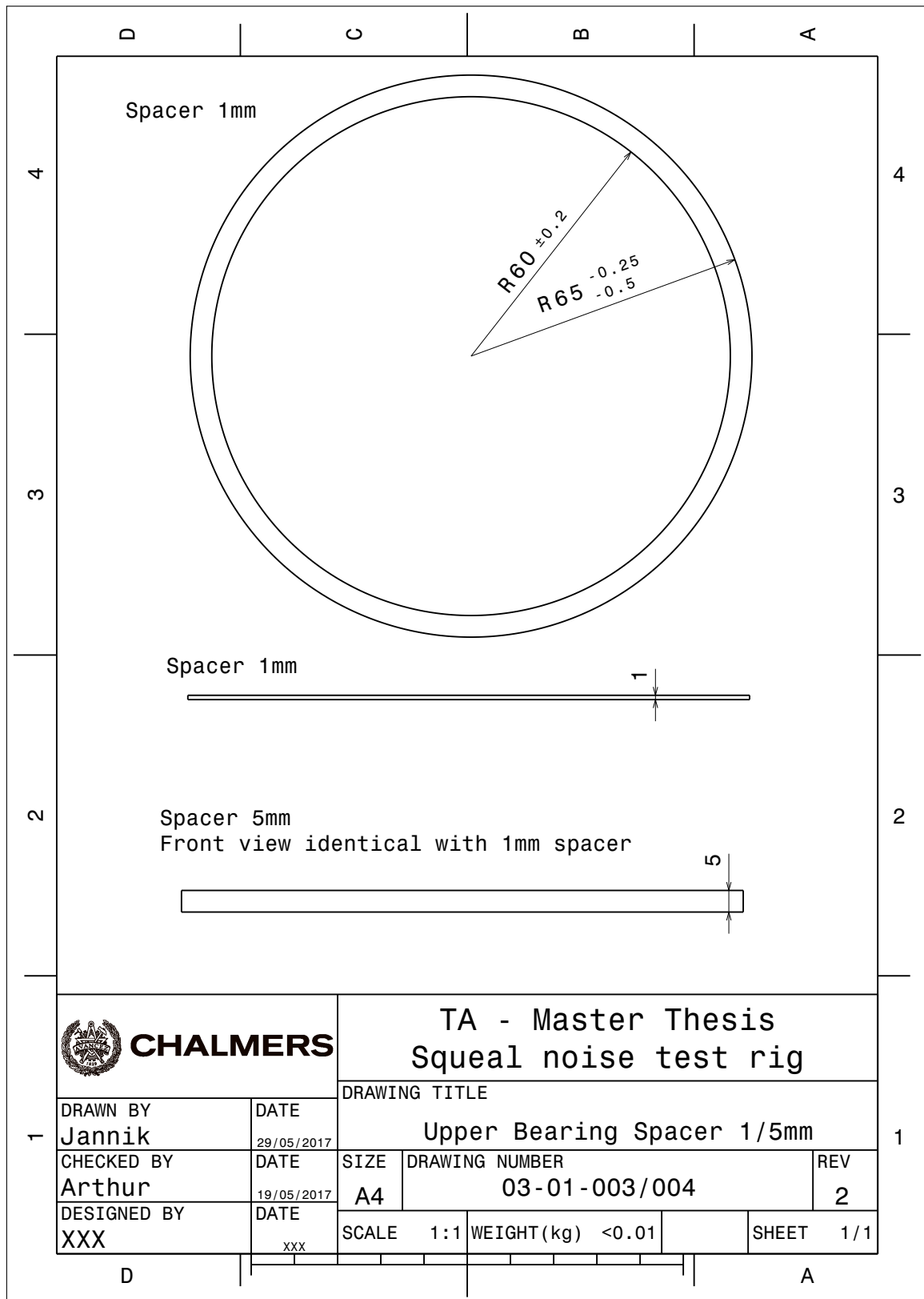


Figure B.15: Upper Bearing Spacers

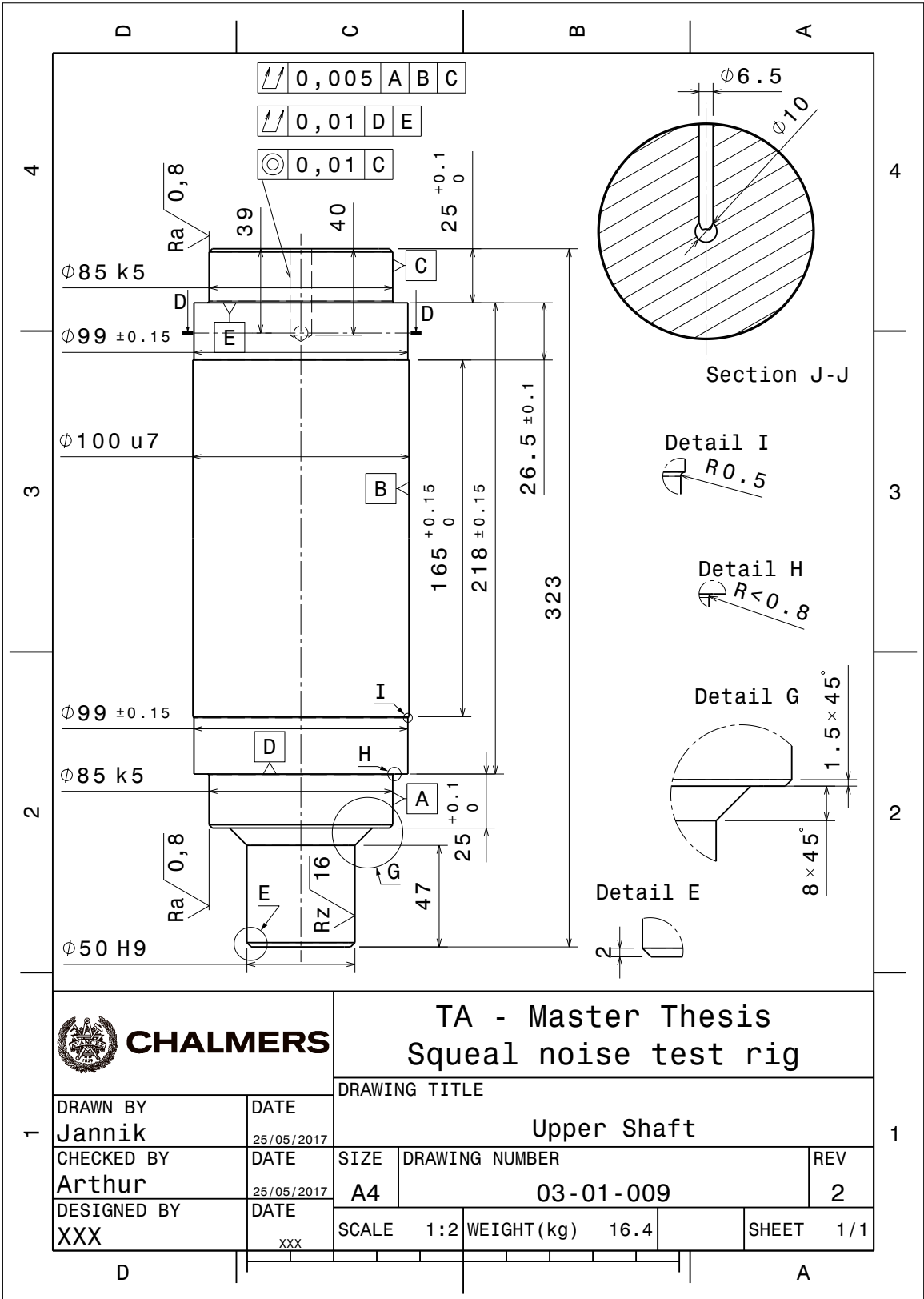


Figure B.16: Upper Shaft

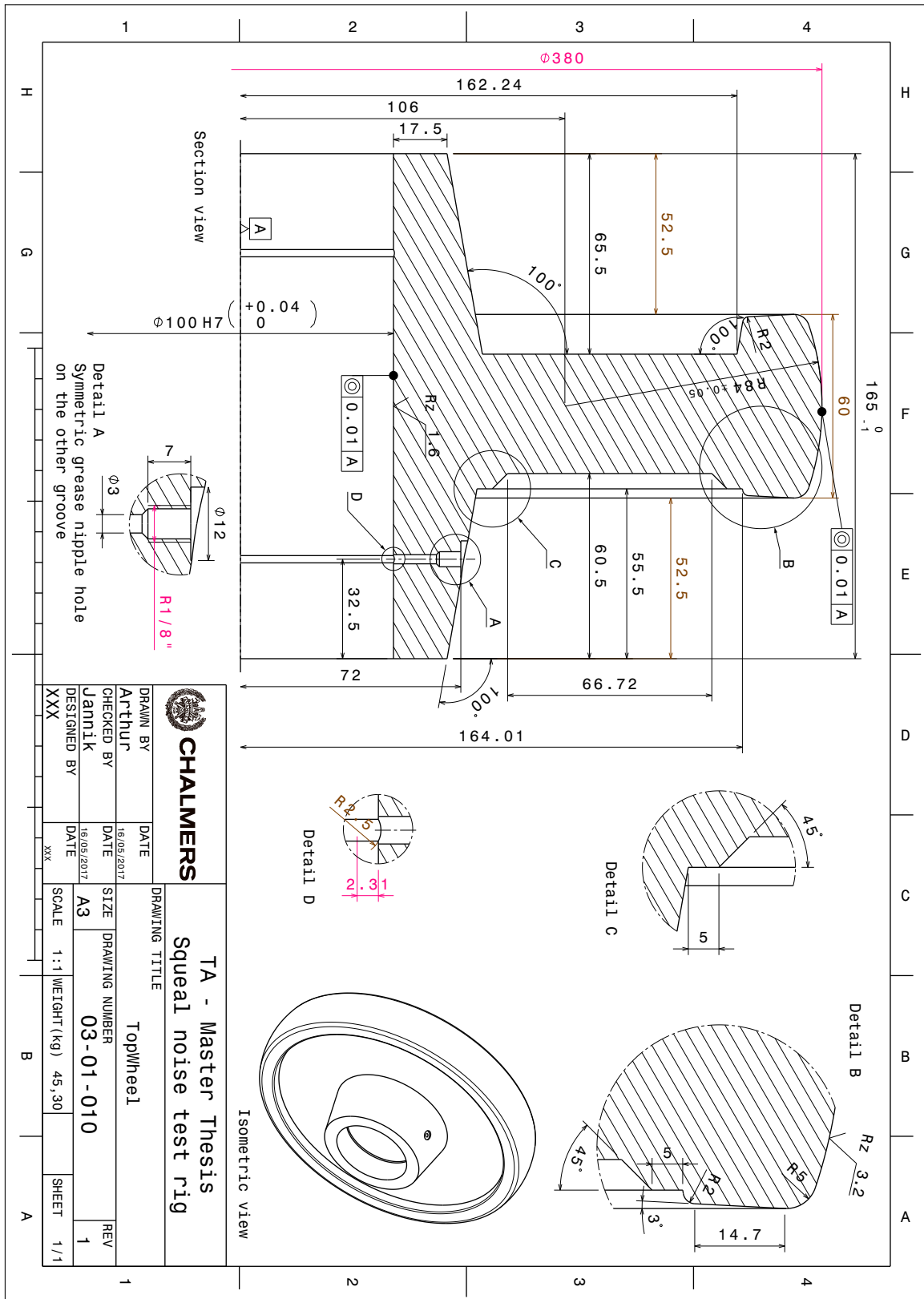


Figure B.17: Upper Wheel

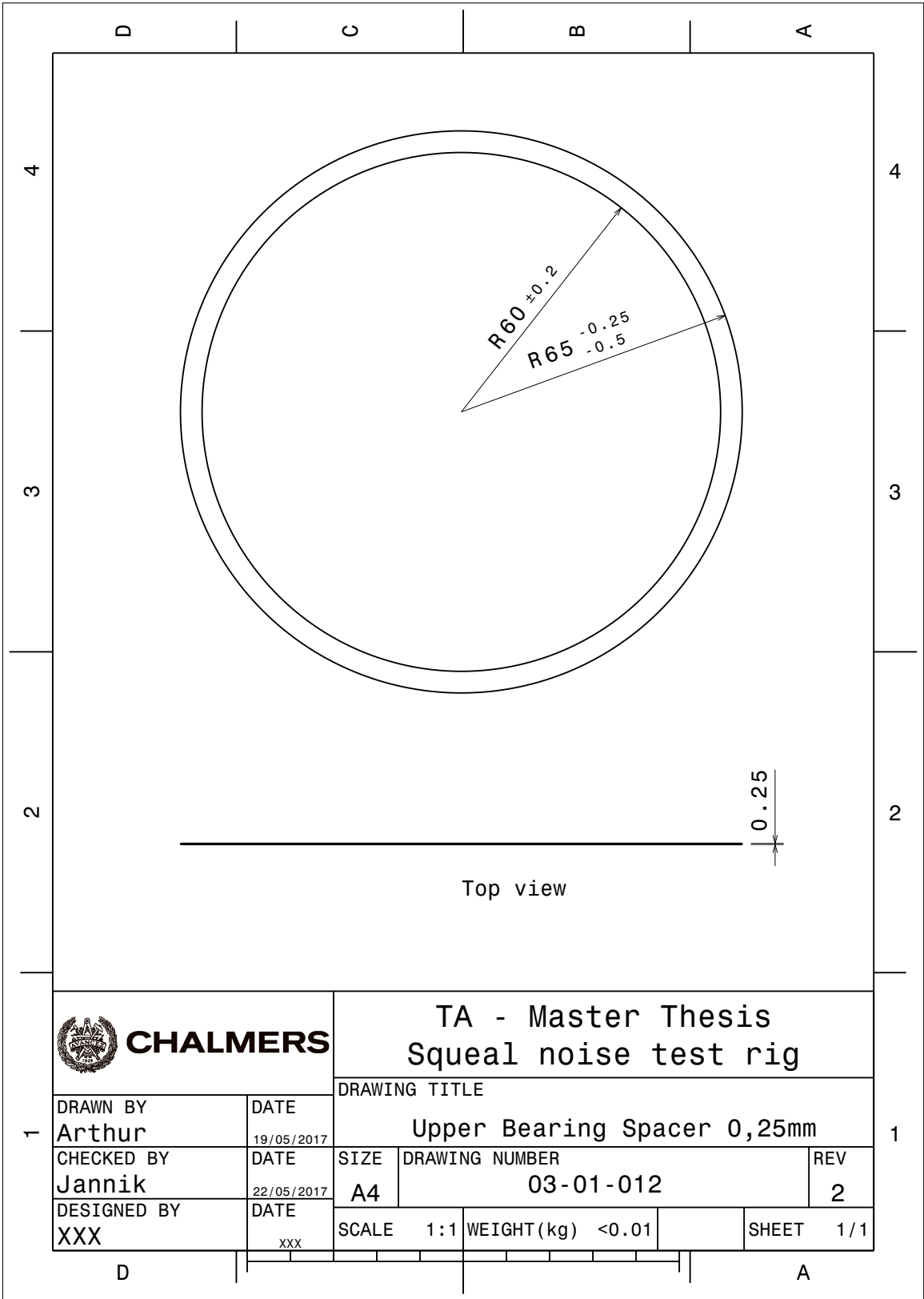


Figure B.18: Upper Bearing Spacer

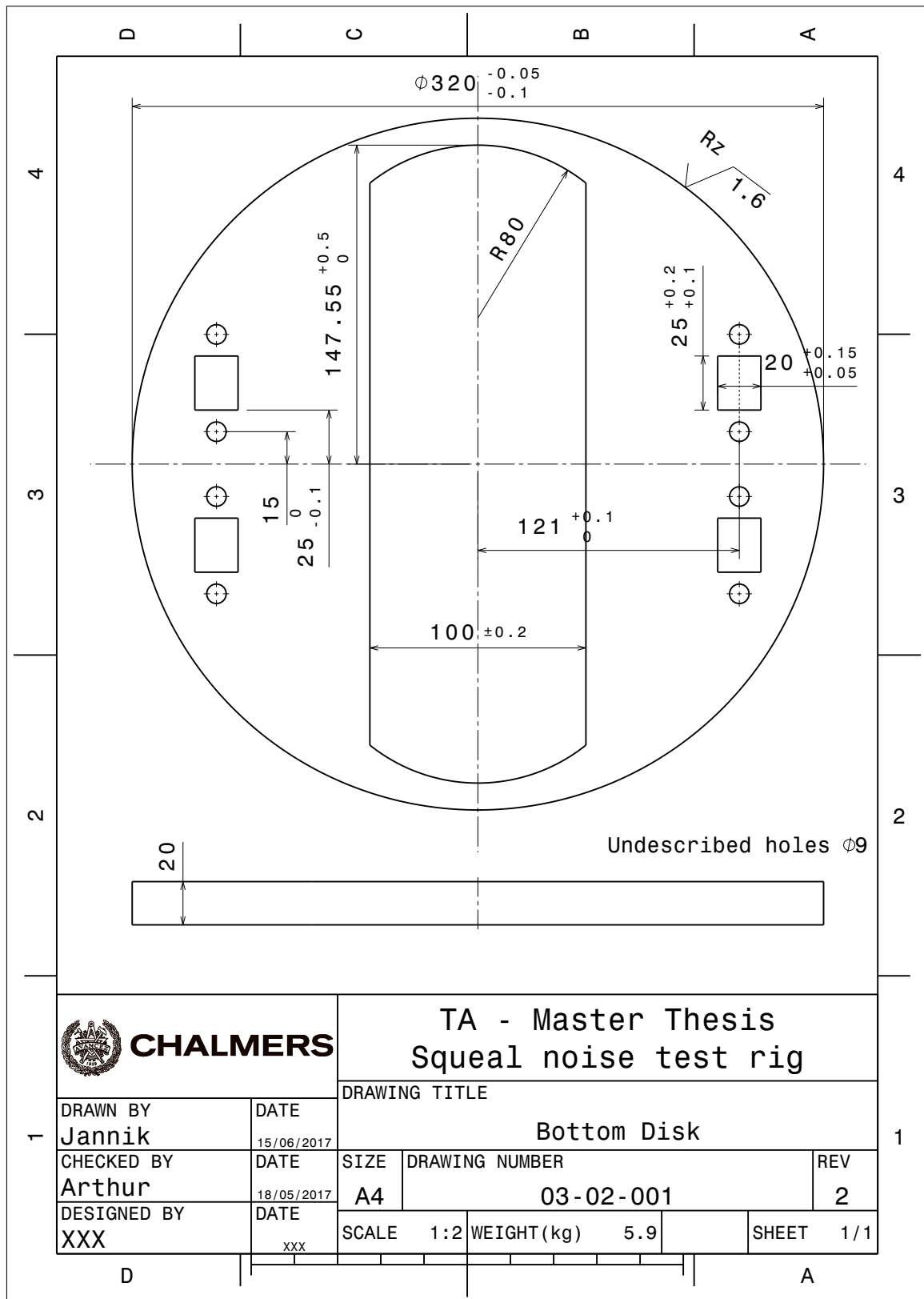


Figure B.19: Bottom Disk

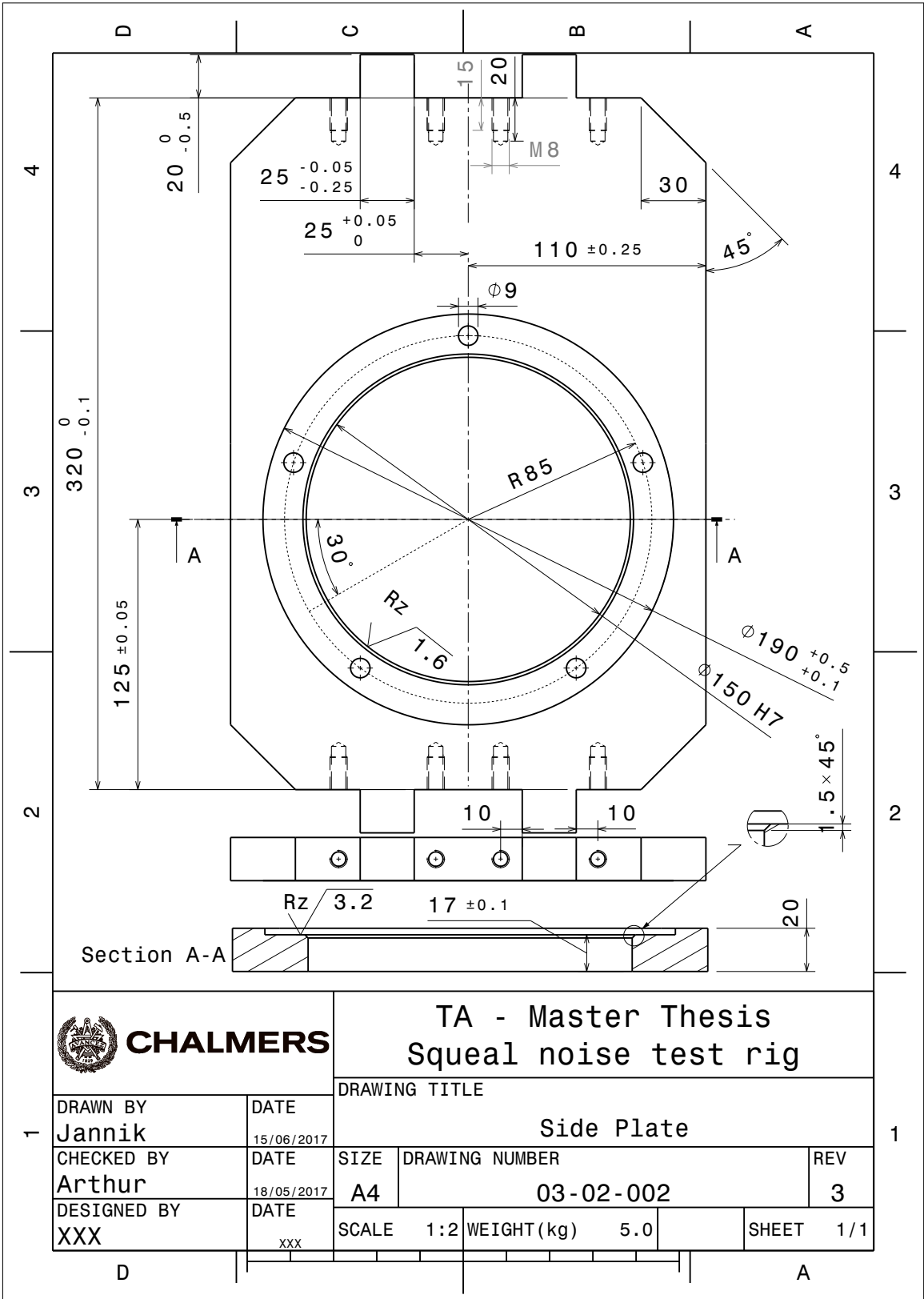


Figure B.20: Lantern Side Plate

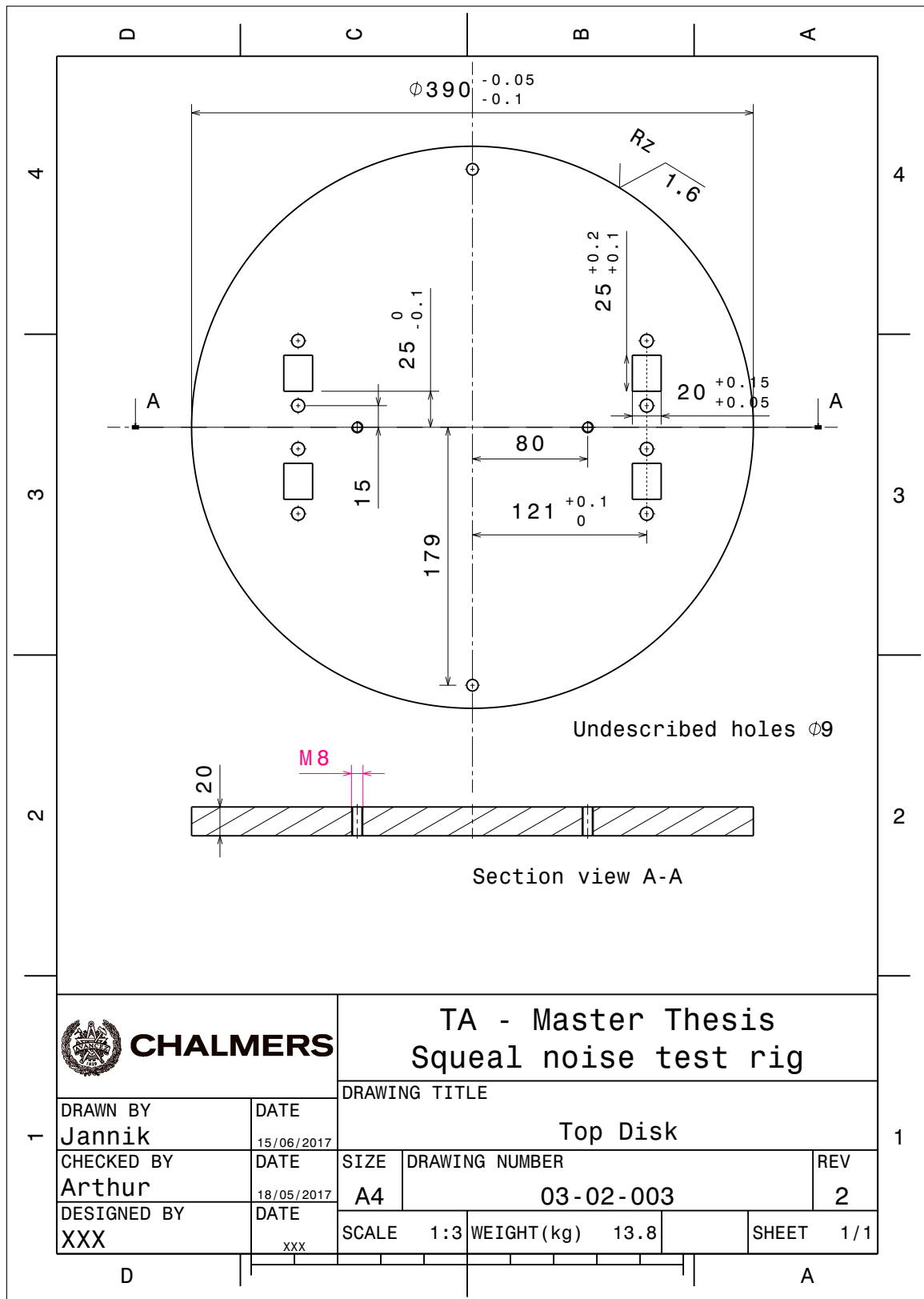


Figure B.21: Top Disk

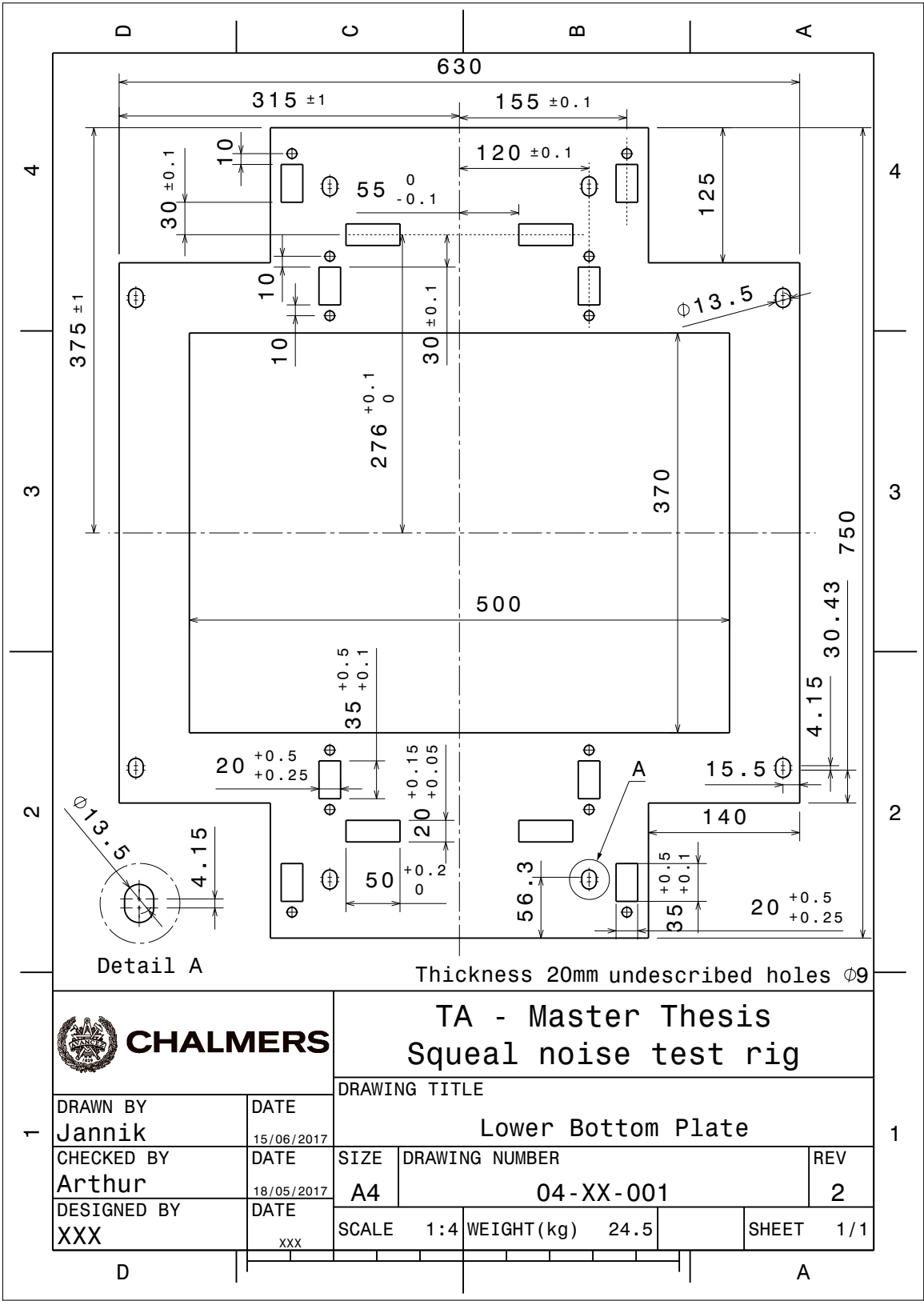


Figure B.22: Lower Bottom Plate

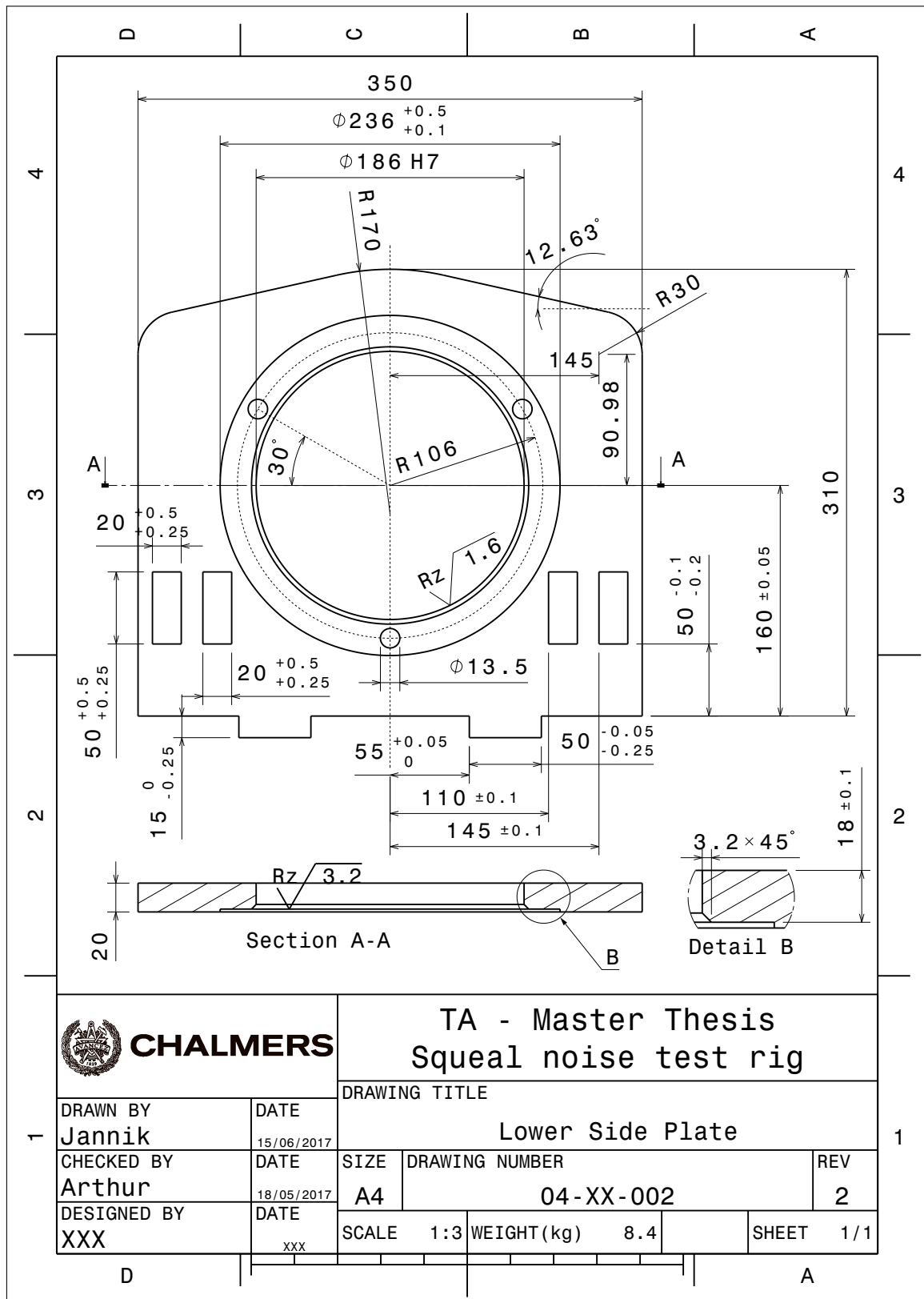


Figure B.23: Lower Side Plate

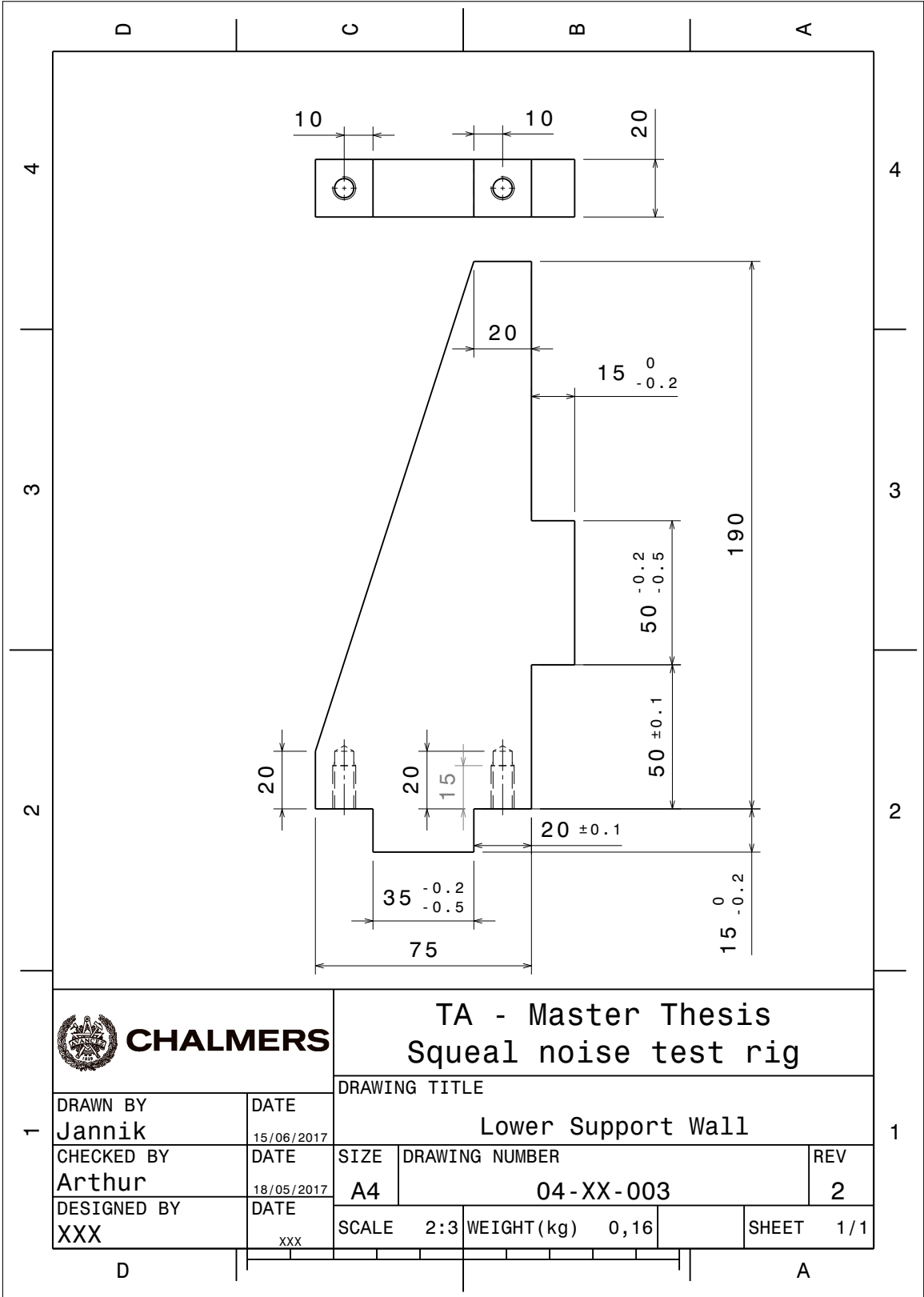


Figure B.24: Lower Support Wall

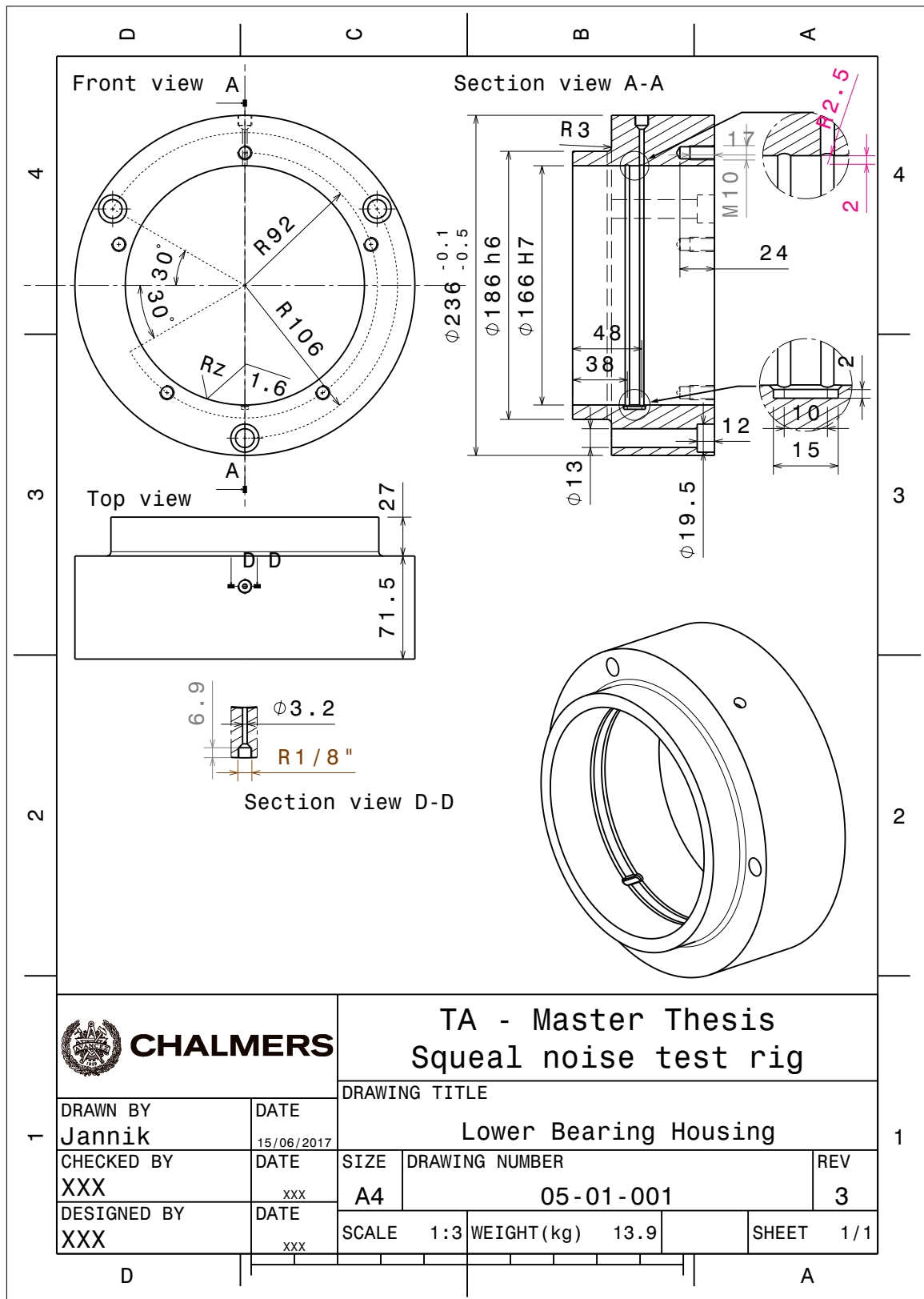


Figure B.25: Lower Bearing Housing

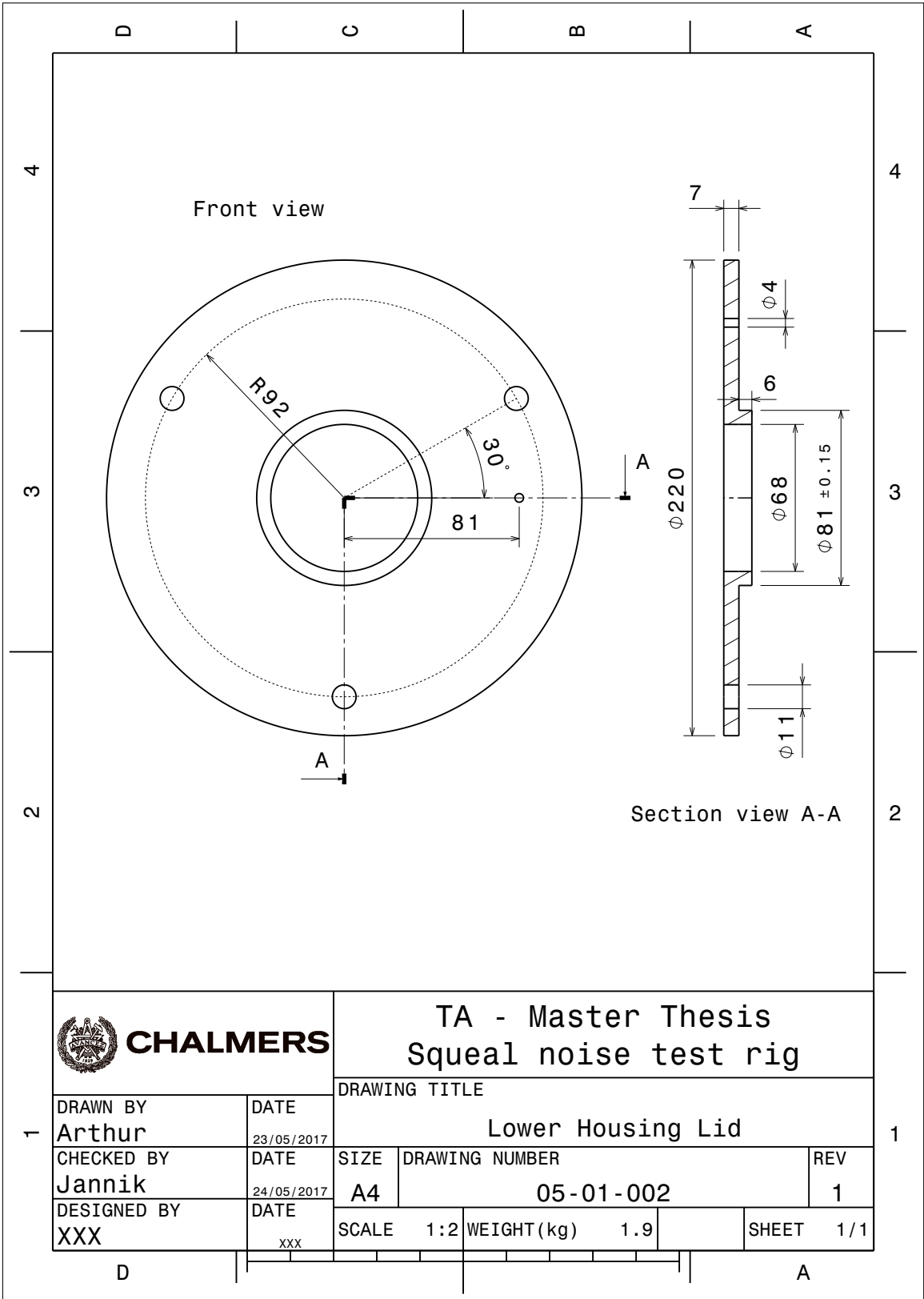


Figure B.26: Lower Housing Lid

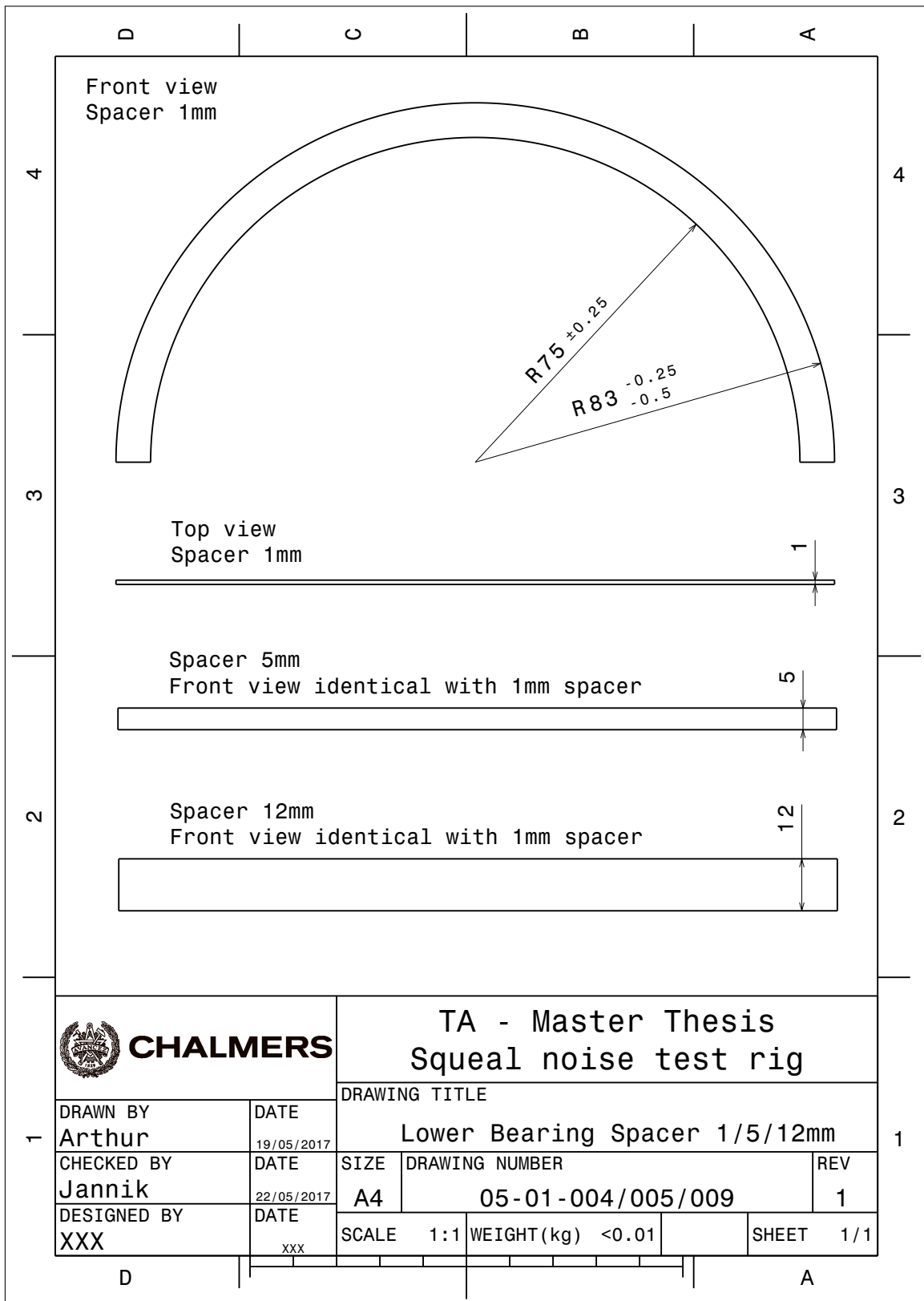


Figure B.27: Lower Bearing Spacers

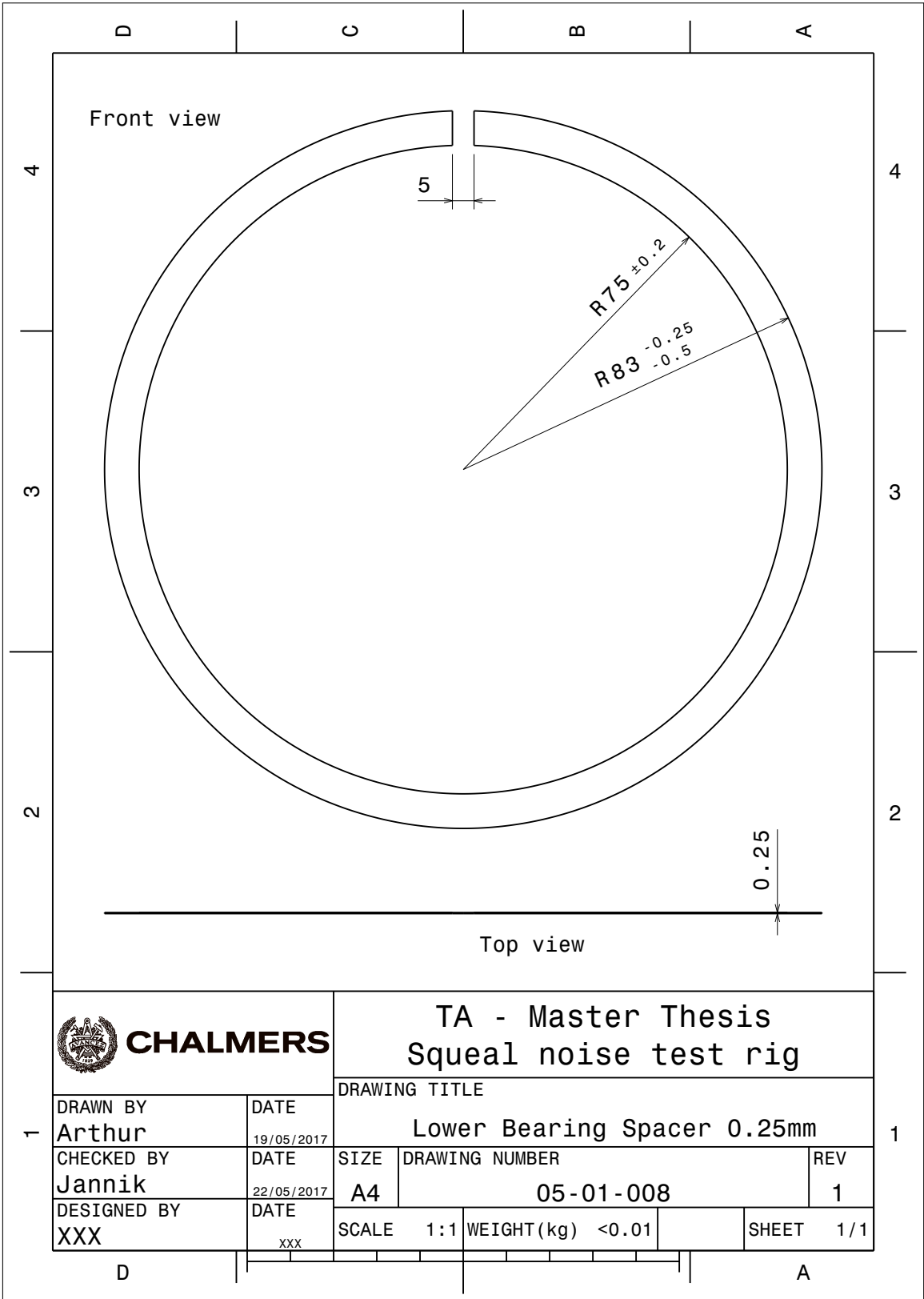


Figure B.28: Lower Bearing Spacer 0.25 mm

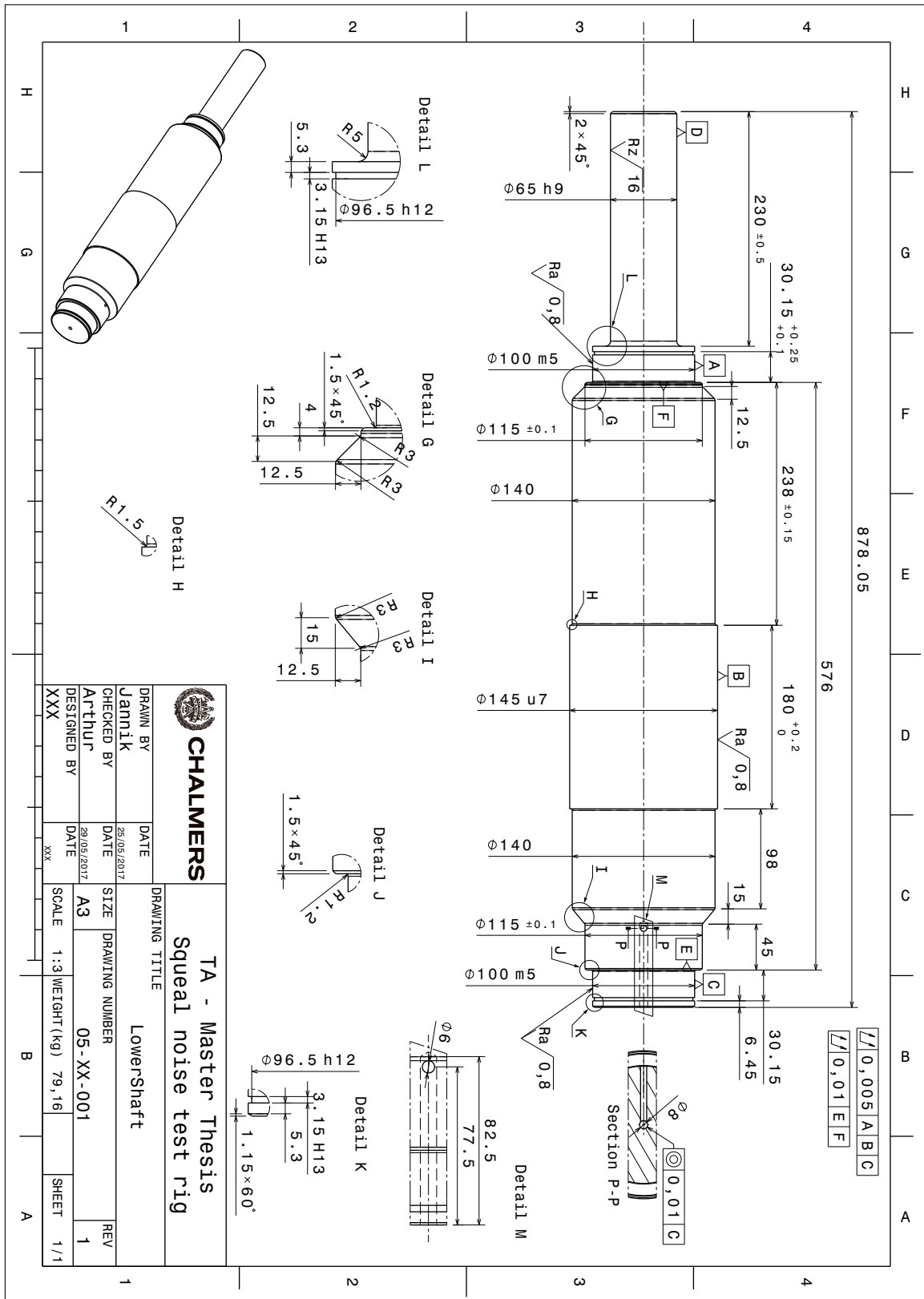


Figure B.29: Lower Shaft

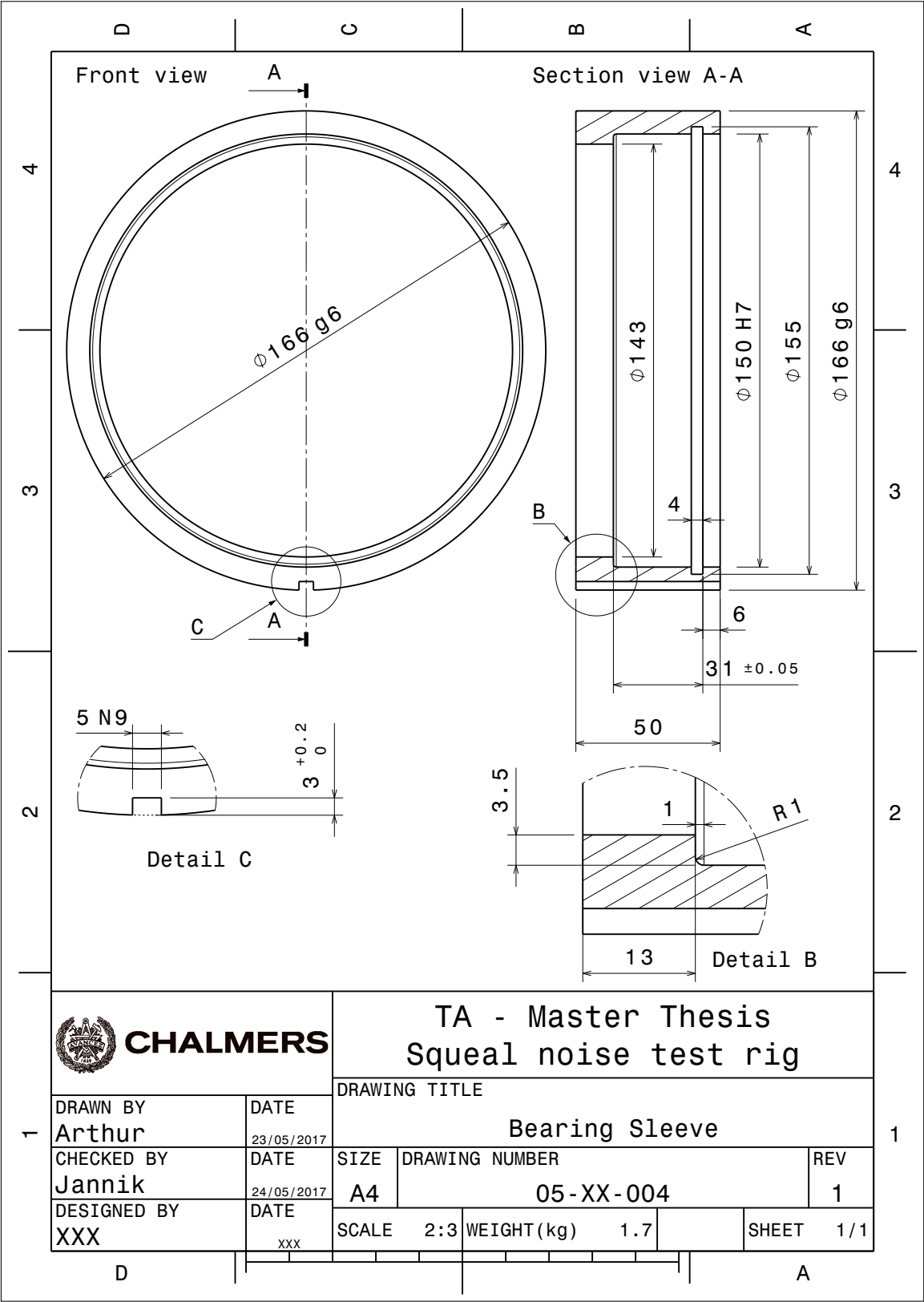


Figure B.30: Bearing Sleeve

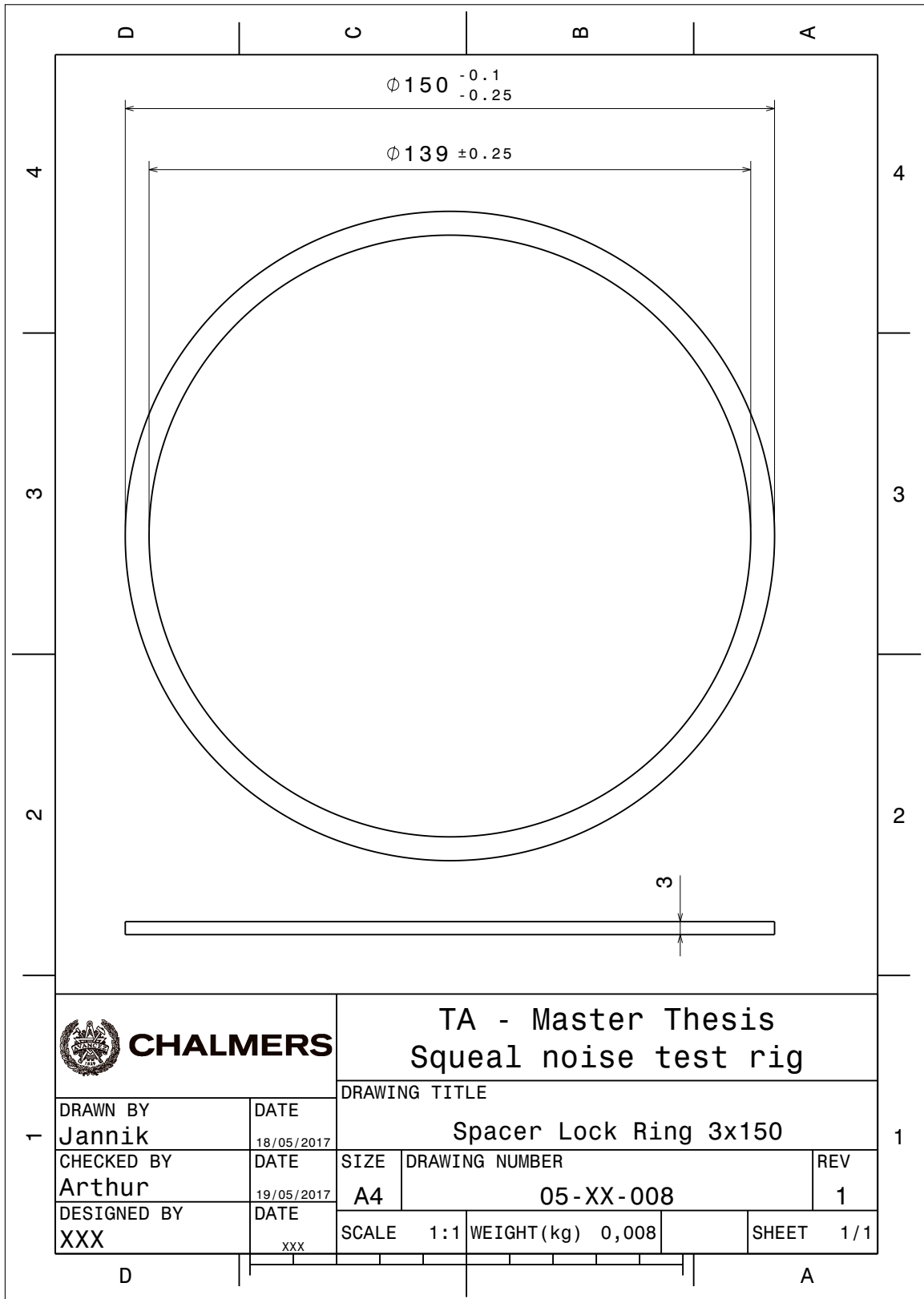


Figure B.31: Spacer Lock Ring 3x150

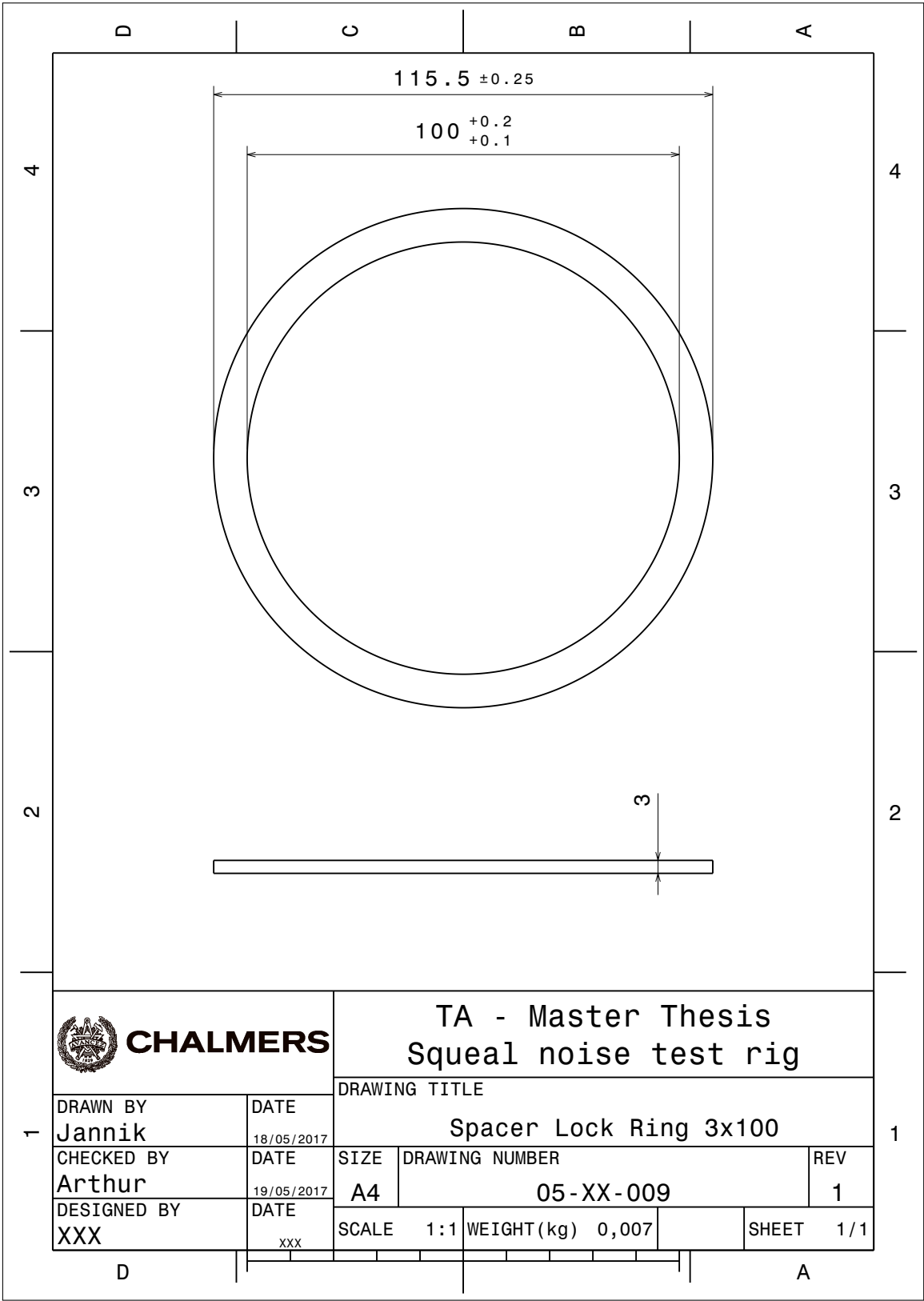


Figure B.32: Spacer Lock Ring 3x100

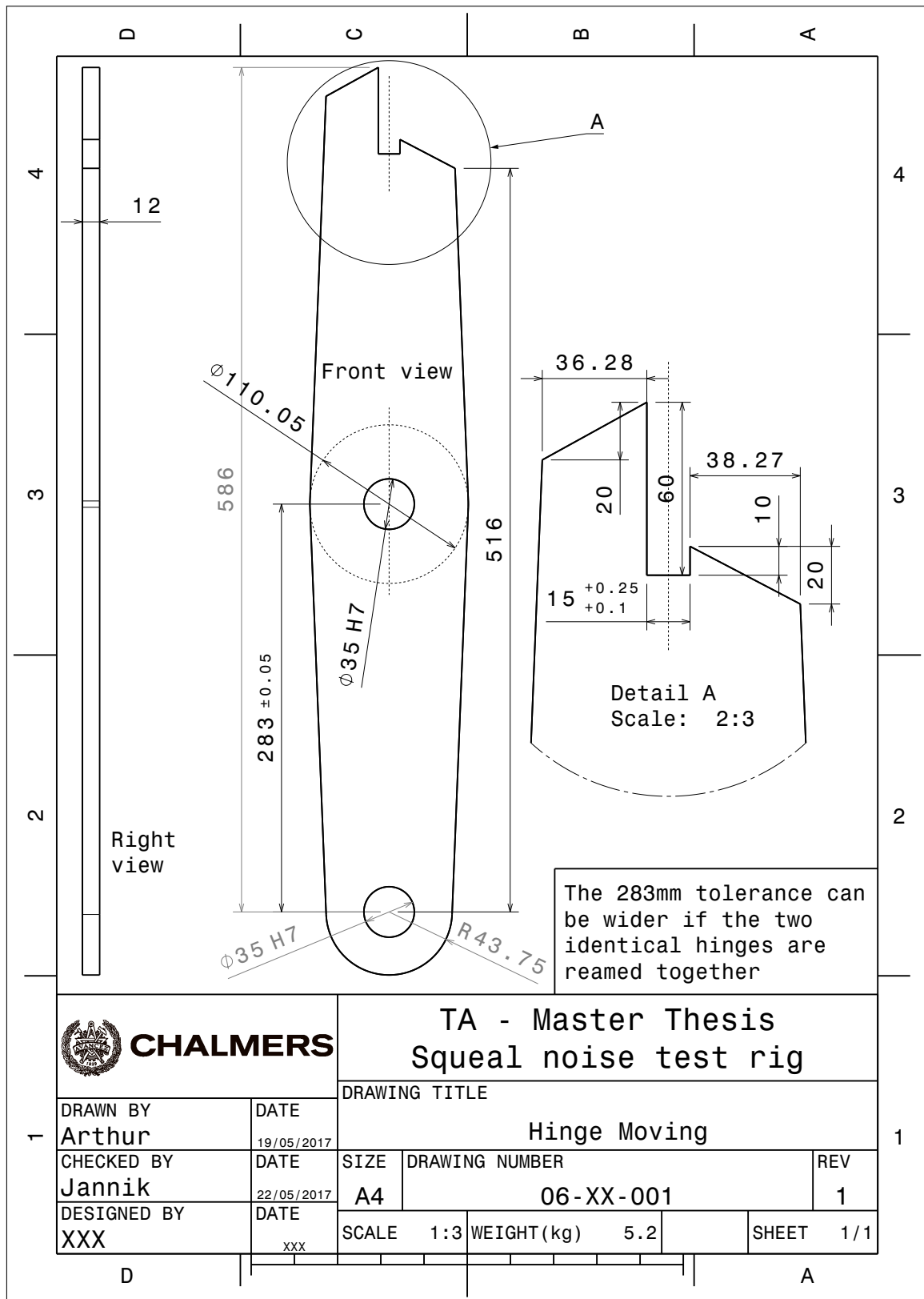


Figure B.33: Force Lever

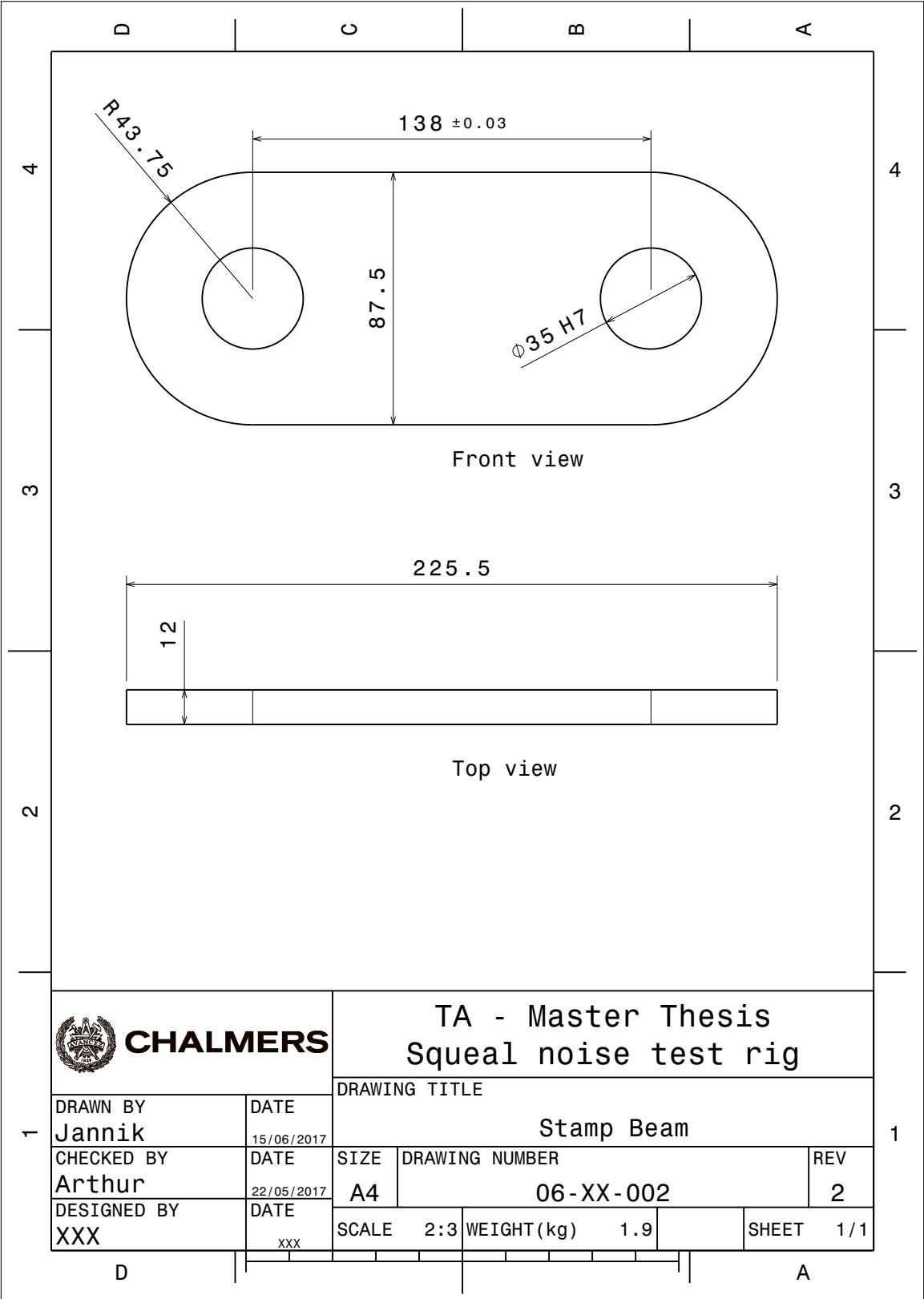


Figure B.34: Stamp Beam

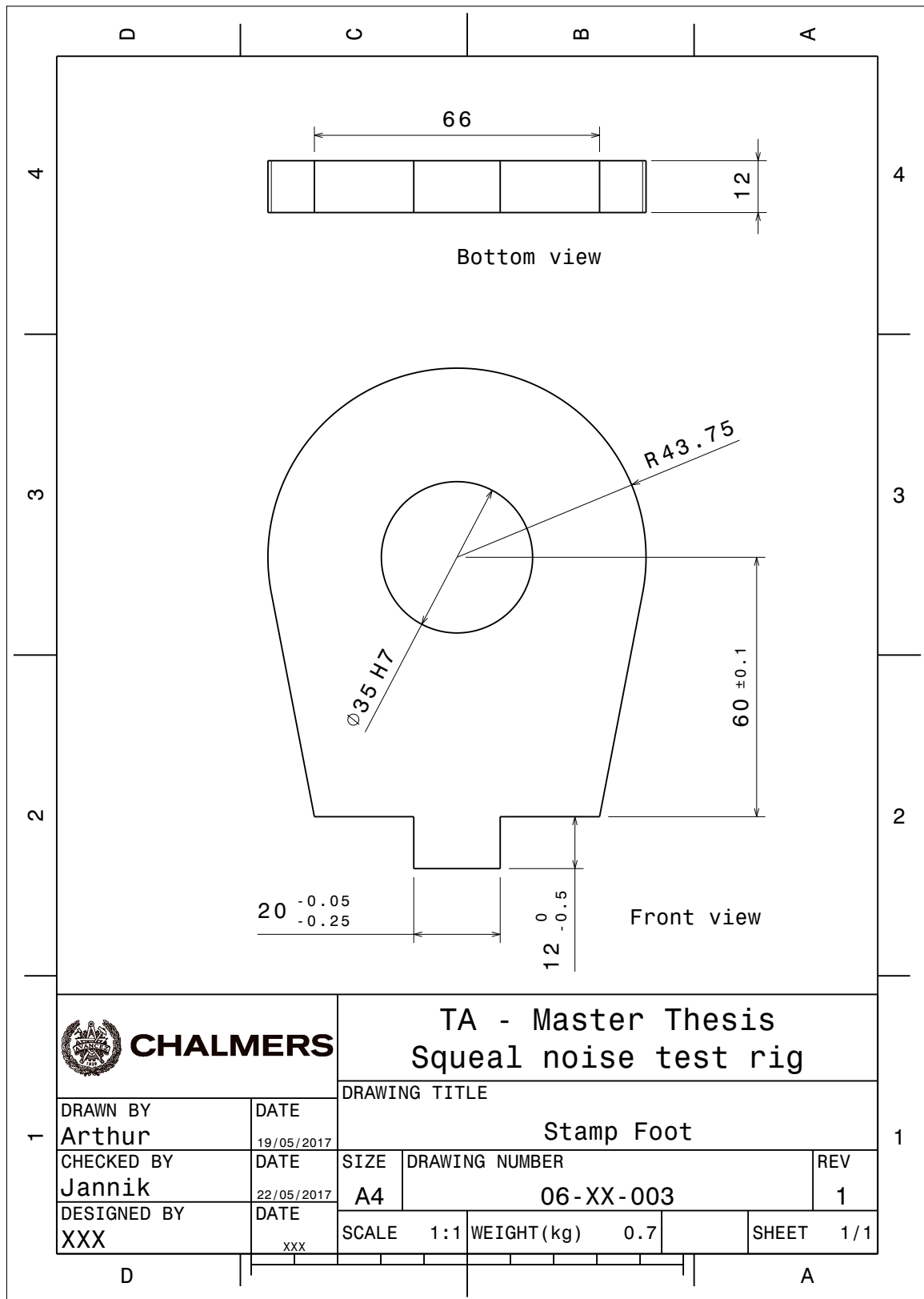


Figure B.35: Stamp Foot

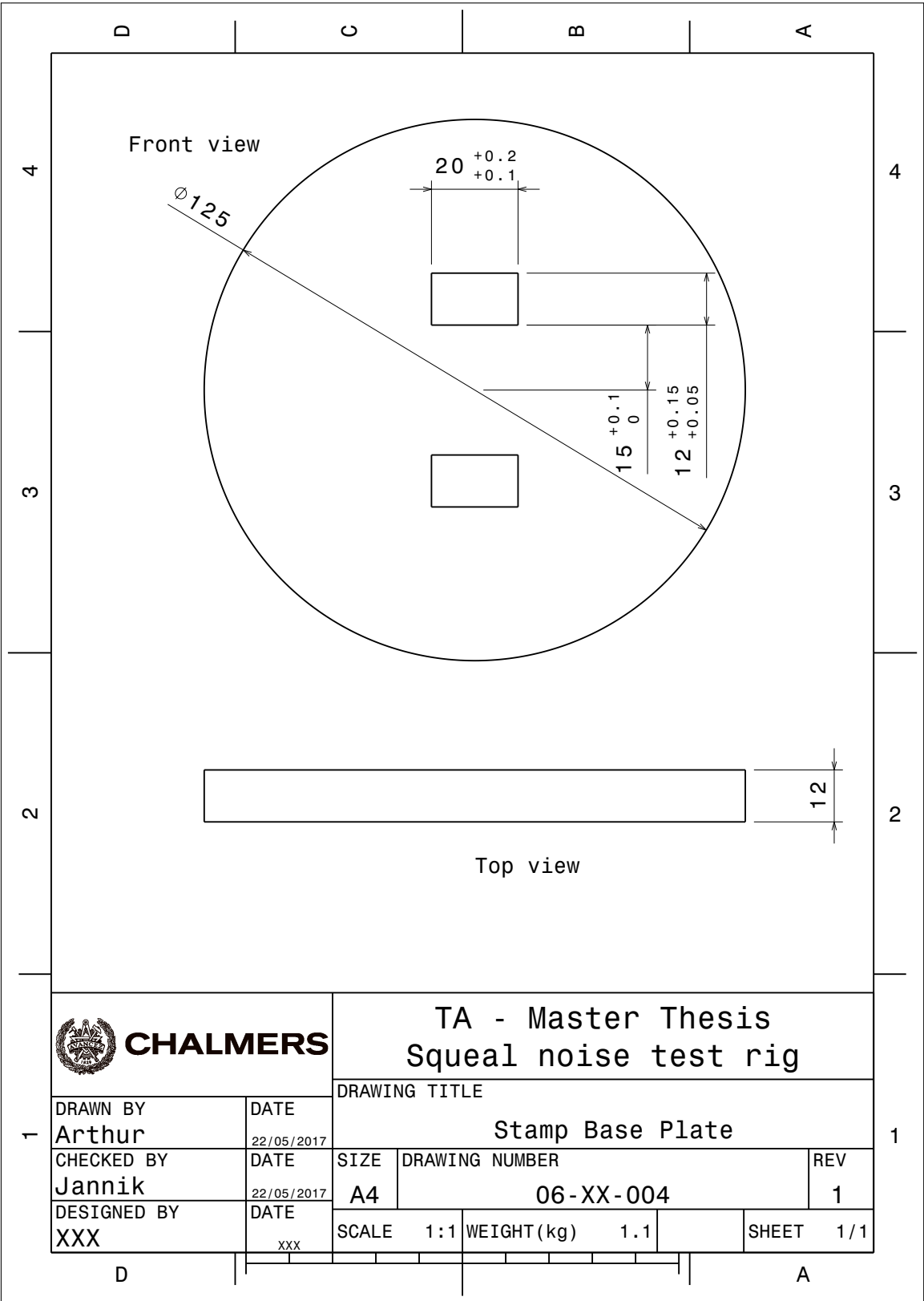


Figure B.36: Stamp Base Plate

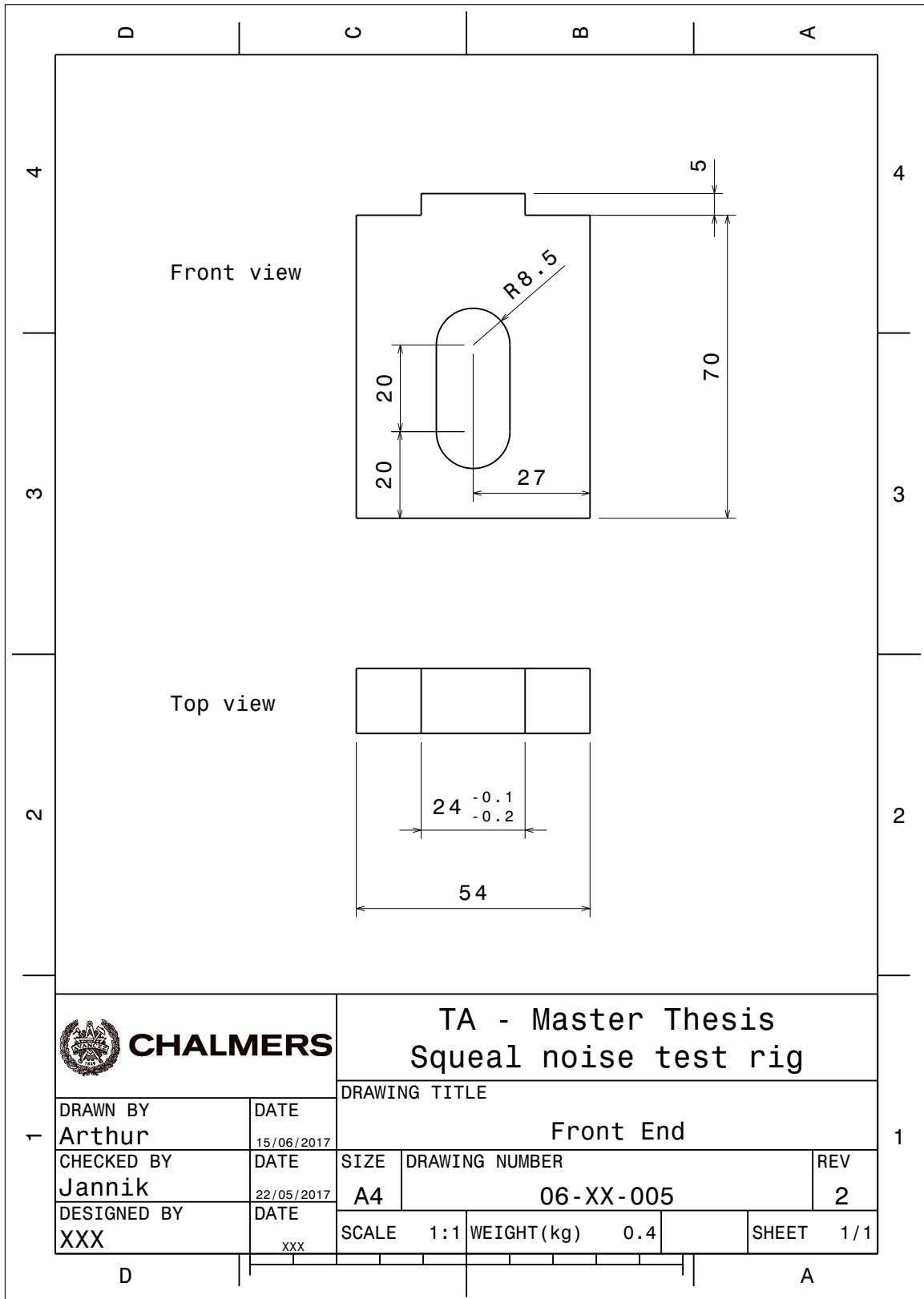


Figure B.37: Front End of the Lever.

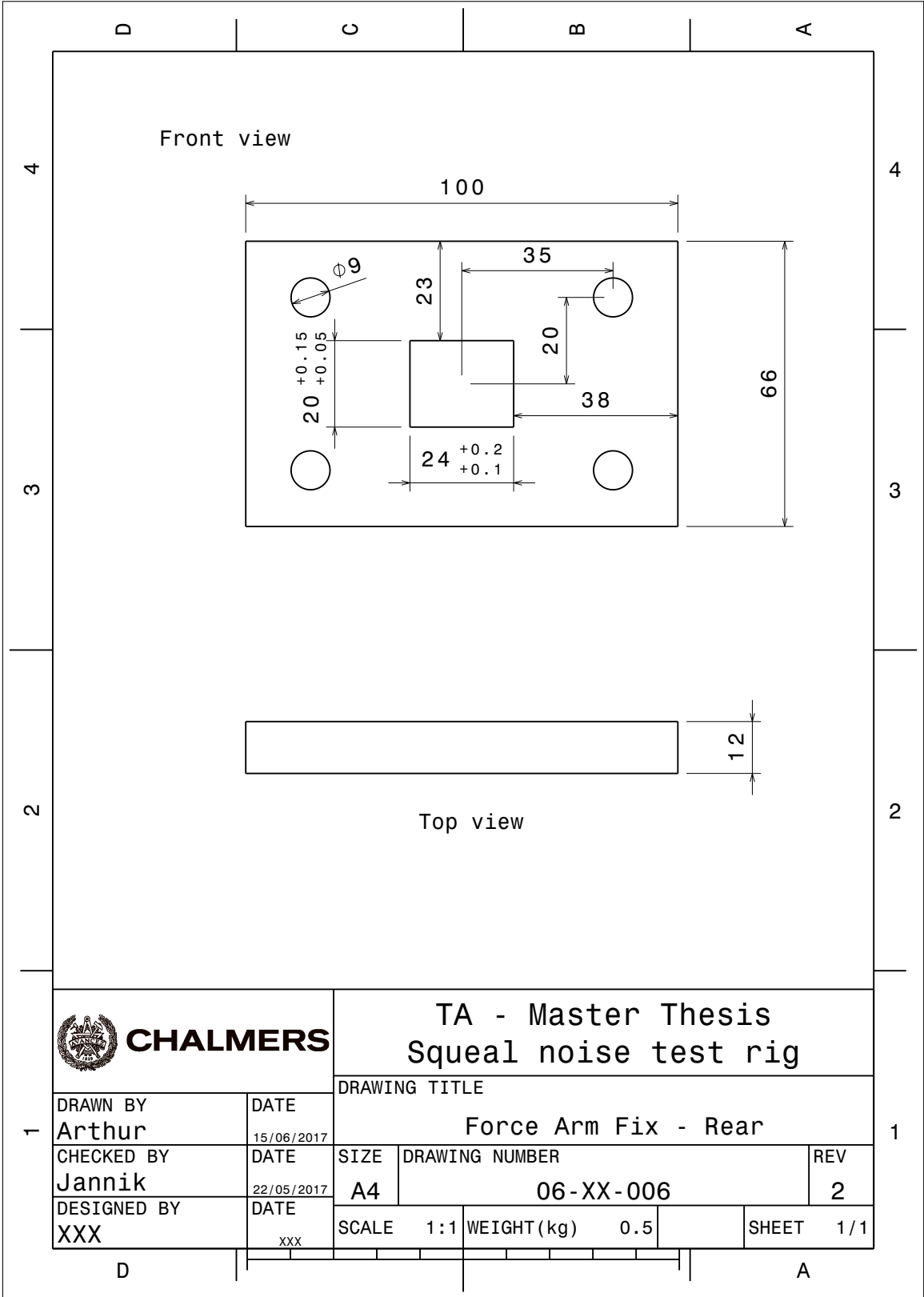


Figure B.38: Force Arm Fix - Rear

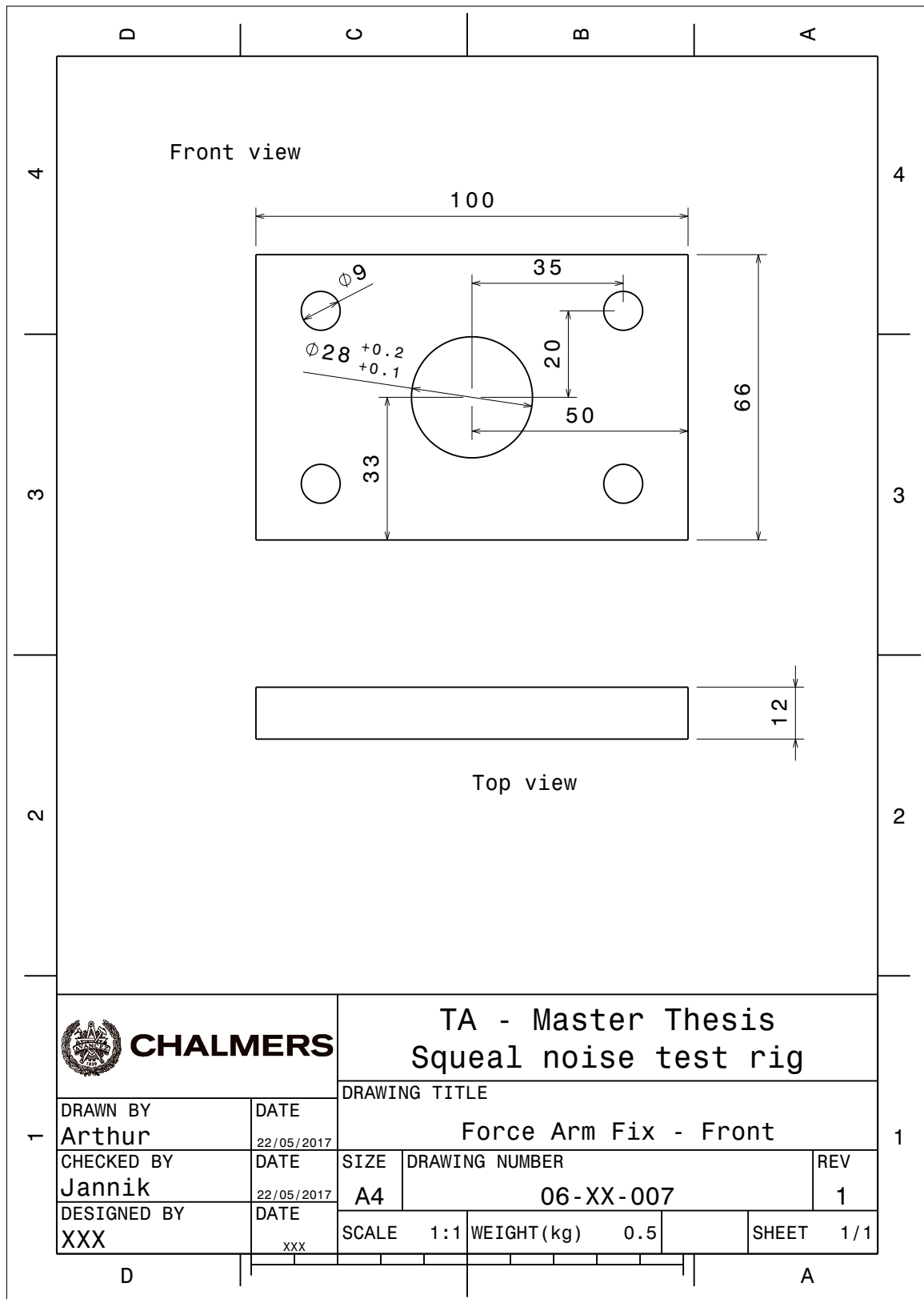


Figure B.39: Force Arm Fix - Front

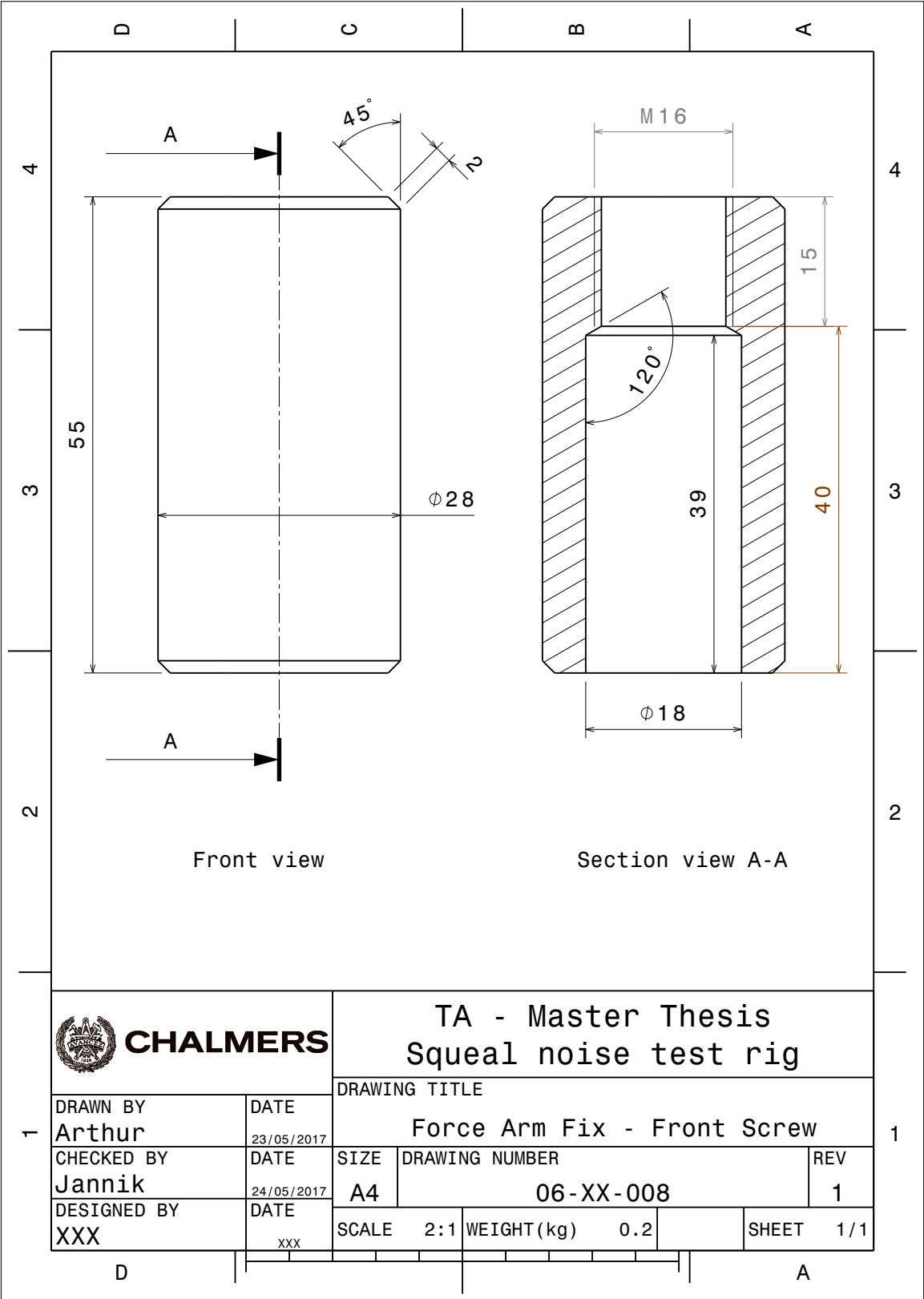


Figure B.40: Force Arm Fix - Front; Screw socket for force generation screw.

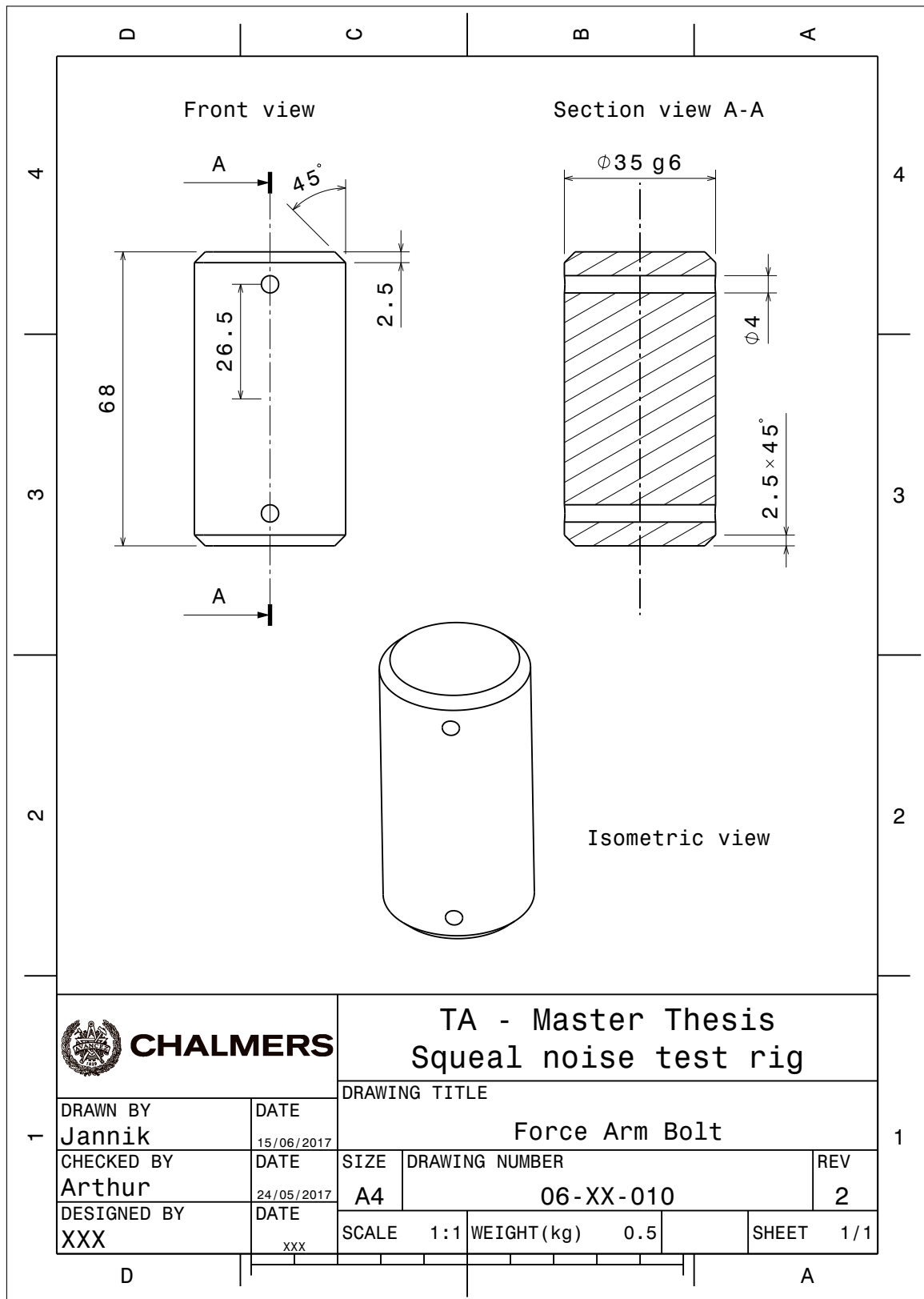


Figure B.41: Force Arm Bolt

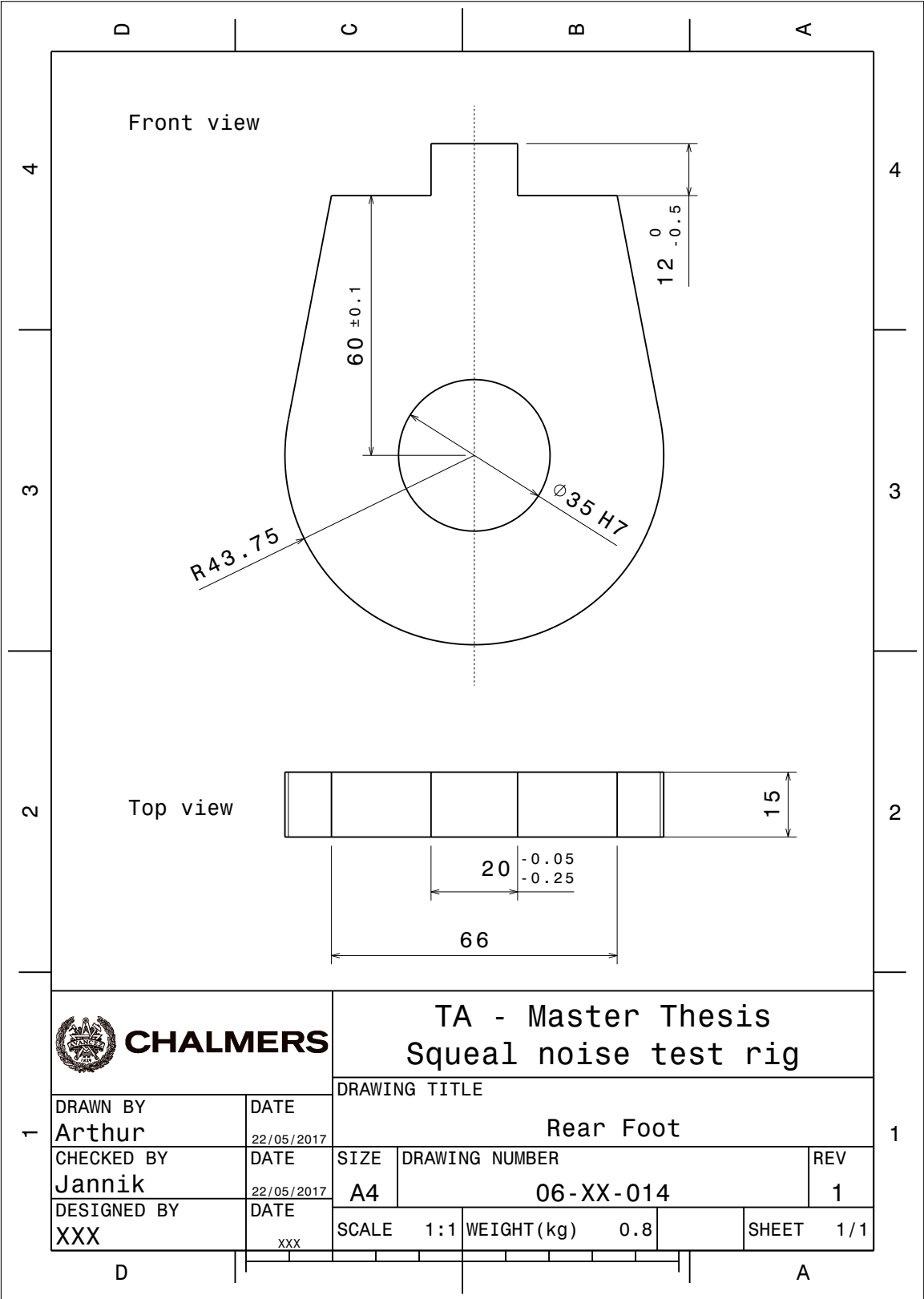


Figure B.42: Rear Foot

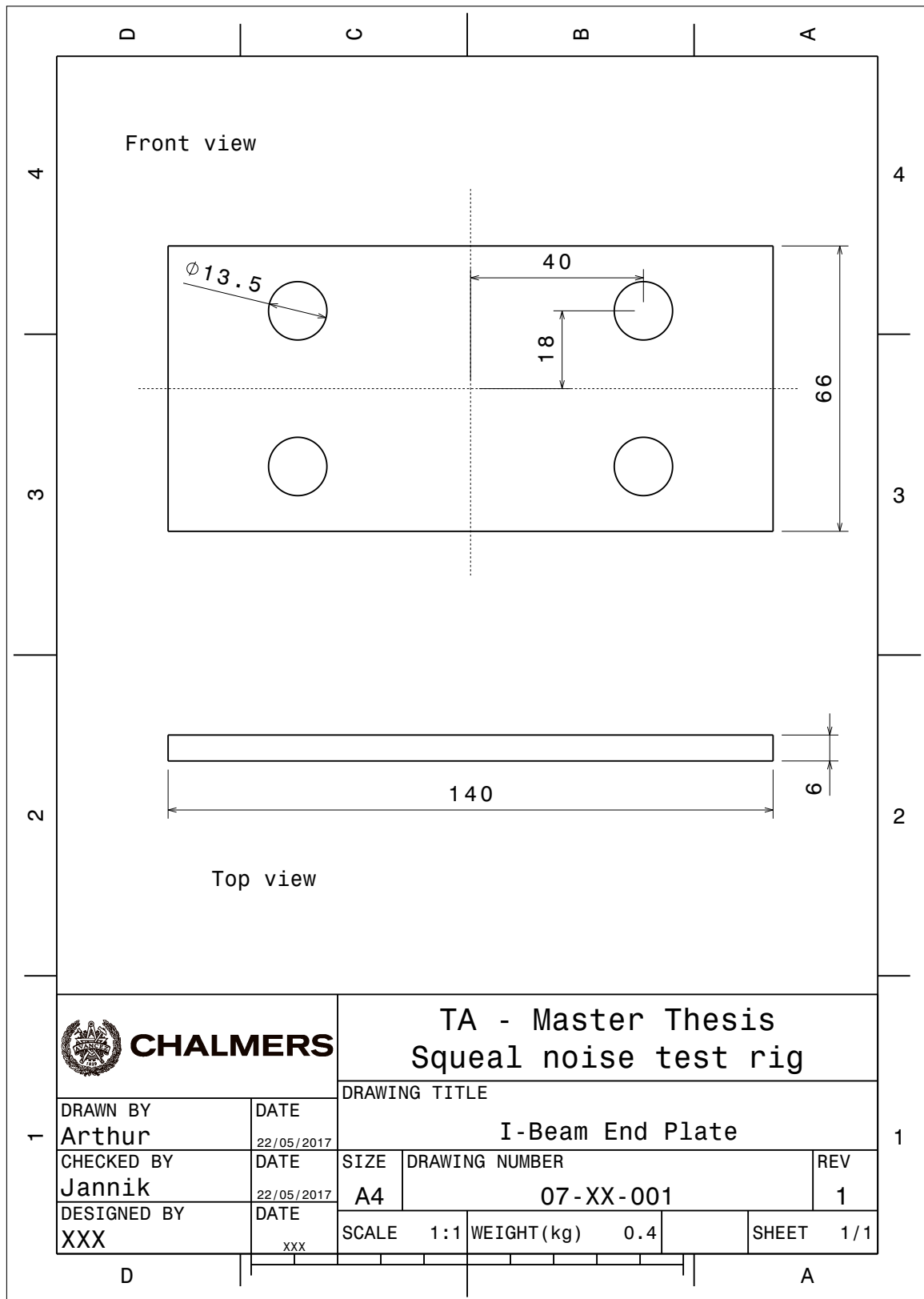


Figure B.43: I-Beam End Plate